# Study on Fe-Cr-based Brazing Filler Metals as Substitutes for Ni-based Brazing Filler Metals

September, 2016

Kangdao Shi

Contents

Chapter 1 Introduction

Chapter 2 Microstructures and electrochemical characteristics of Fe-Cr-based brazing filler metals

Chapter 4 Corrosion resistance of SUS304 stainless steel joints brazed with Fe-Cr-based brazing filler metals

Chapter 5 Conclusions

# Chapter 1 Introduction

## 1.1 Background of this study

Due to environmental pollution, global warming has attracted much attention in recent years, and one of the main factors is exhaust gas from automobiles [1]. Exhaust gas from automobiles usually consists of a variety of components including fine carbonaceous particulate matter (PM), oxides of nitrogen (NOx) and volatile unburnt hydrocarbons. All are considered to be deleterious to human health as well as environment [2, 3]. Exhaust gas from automobiles and the resulting health hazards are the growing concerns today.

In general, the control of pollutants can be divided into two strategies. One is focused on end-of-pipe controls after combustion, while the other directly works on combustion process acting on the root of pollutant emissions [4]. The former includes selective catalytic reduction (SCR), DeNOx and the diesel oxidation catalyst (DOC) installed in exhaust pipes. The latter includes low-excess-air (LEA) burn, staged-fuel, ignition delay and exhaust gas recirculation (EGR) [4, 5].

During the past decades, significant progress has been achieved in decreasing emissions of NOx and PM, but the legislated maximum levels of emissions are more and more tightened [6-10]. The European Union has approved the Euro VI (2014) regulations. In the regulations, the $NO_X$ and PM emission standards are 0.08 and 0.005 g/km, respectively. Compared with the Euro V ($NO_X$ 0.18 g/km and PM 0.005 g/km), more strict $NO_X$ emission regulations imply that engine manufacturers and researchers must develop more effective solutions to reduce $NO_X$ emission [11-13]. Although significant improvements have been achieved, continuous development and innovation are required to meet future EU, JP and US emission targets [14].

In order to restrain the formation of $NO_X$, exhaust gas temperature must be decreased significantly [15, 16]. A cooled EGR system is one of the most effective solutions in established techniques [17-28]. In the EGR system, a portion of exhaust gas is returned to the cylinder through an EGR cooler for combustion. The presence of cooled inert gas reduces the amount of oxygen available for combustion, thereby lowers the flame temperature and as a result, reducing the amount of NOx produced [1]. As recognized, EGR is possibly the only available technology to meet more stringent legal regulations for engine emission in the future [29].

To improve the performance and efficiency of EGR coolers, the designs are becoming increasingly compact and complex. These configurations result in a large number of internal joints [30]. As shown in Fig. 1.1.1, the fabrication of an EGR cooler involves bonding fins to plates, and brazing is the preferred option for the complex systems. Several commercial brazing filler metals exist, including silver-based and nickel-based [31]. Regarding conditions of the use, corrosion resistance of materials is important. Stainless steel joints brazed with Ni-based filler metals are popular in practical application because of the excellent corrosion and heat resistance [32, 33].

Owing to soaring commodity prices of bare metals, there has been a growing anxiety for resources in a variety of industry sectors since 2003. The price of Ni has fluctuated widely. In 1989 the price of Ni was around $8.00 per pound in London Metal Exchange (LME). In 1999 the LME price of Ni was as low as $2.00 per pound. As shown in Fig. 1.1.2, the peak of over $22.00 per pound was June 2007 and the price dropped down by the end of 2008. In the first quarter of 2016, the LME average price was $3.82 per pound. However, it is presumed that the higher price is followed with a recovery in demand [34]. Therefore, the Ni-based filler metals, mainly composed of Ni, are subject to the high cost. On the other hand, cars are equipped with different brazed devices in addition to EGR, continuous pressure for cost reduction makes the automobile industry take interest in new brazing filler metals with further cost reduction potentials [35]. The development of inexpensive fillers to replace the conventional Ni-based filler metals has been demanded in the industry and market. In contrast to the wide fluctuation in the price, the price of iron, which is currently less than $1.00 per pound, remains relatively modest [36]. It has been advancing to develop new brazing filler materials by adding Fe to reduce raw material cost [37, 38].

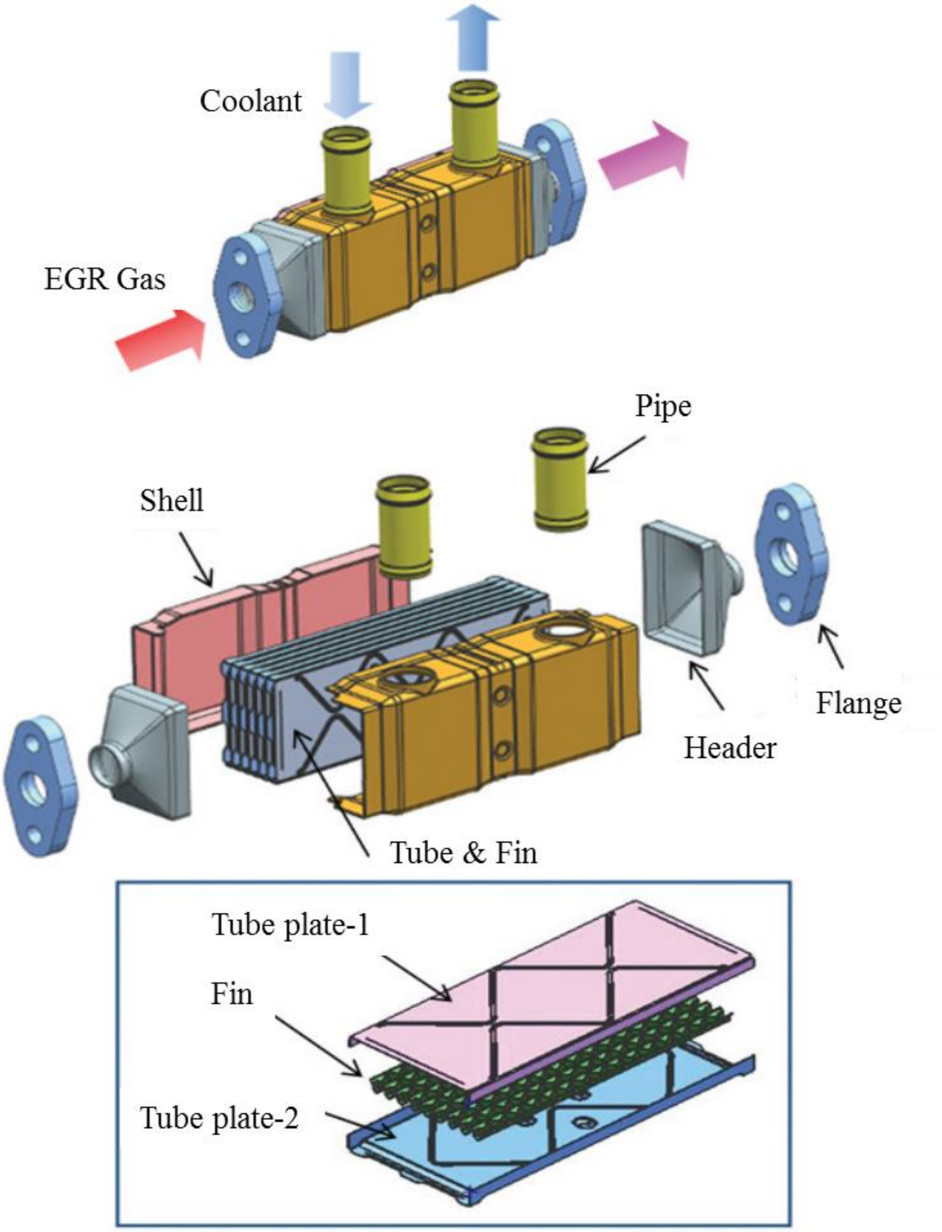

Fig. 1.1.1 Structure of EGR cooler [30].

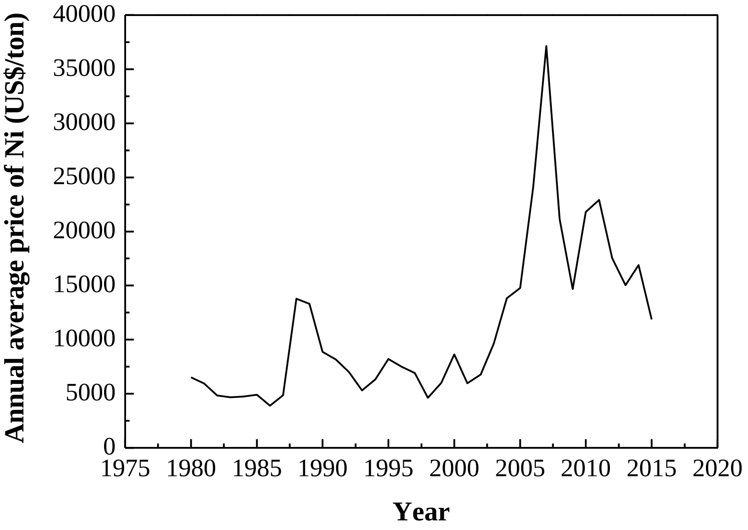

Fig. 1.1.2 Fluctuation in LME annual average price of Ni from 1980 to 2015.

## 1.2 EGR cooler

Most EGR systems consist of EGR coolers, valves, piping, flanges and gaskets. As shown in Fig. 1.2.1, a portion of exhaust gas from the engine comes to the EGR cooler through an EGR valve. From the EGR cooler, the exhaust gas is conducted to an intake throttle assembly and then it is mixed with fresh combustion air cooled by an intercooler to recover some of its density. The mixed air is then returned to the engine.

The EGR cooler is one of the most important elements in the EGR system. The EGR cooler is an air-to-liquid heat exchanger device. In the EGR system, 20-30% hot combustion gas from the engine is recirculated into the EGR cooler, and significantly cooled down by the coolant in the EGR cooler. The inlet coolant and inlet exhaust gas temperatures in the EGR cooler are around 353-363 K and 523-573 K, respectively [11]. As a result of heat exchange between the coolant and the exhaust gas, the outlet exhaust gas temperature is reduced to around 373-393 K, decreasing $NO_X$ emission.

There are commonly three types of the EGR cooler: shell and tube type, wave fin type and off-set fin type, every of which has its own advantages and disadvantages. Fig. 1.2.2 shows their schematic diagrams and photographs.

The shell and tube type EGR cooler is easy to manufacture and the production cost is low. In

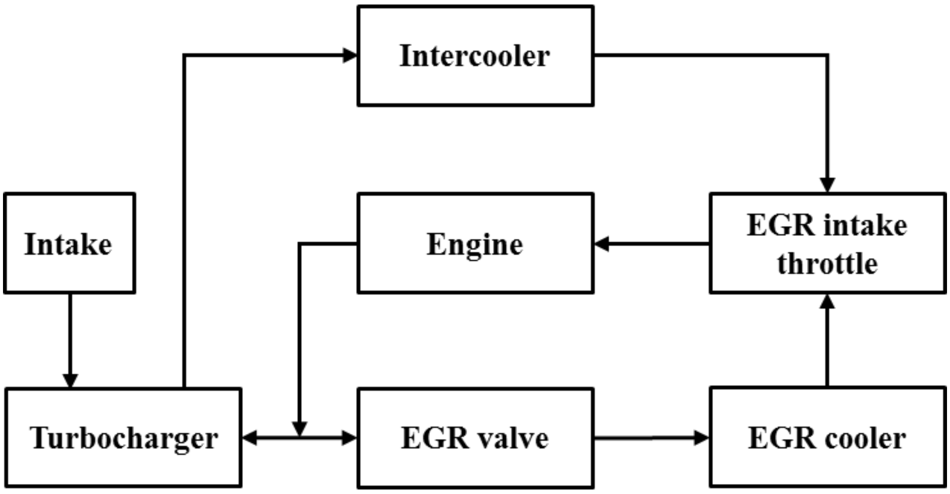

Fig. 1.2.1 Schematic diagram of cooled EGR system.

contrast, the thermal efficiency of the shell and tube type heat exchanger is inferior to that of the wave fin type [39]. Due to outstanding performance, the helical baffle shown in Fig. 1.2.3 has been introduced into the EGR cooler recently [40]. The helical baffles can improve heat transfer and pressure drop characteristics with eliminating the pressure losses [41]. The shell-and-tube heat exchanger with helical baffles also shows significant improvement in the fouling behavior during operation.

The wave fin type EGR cooler features a high thermal efficiency, and the system can be designed in proportion to the size compactly [42] and is of more effective than that of the shell and tube type because of the increased surface area and better mixing of the coolant flow [18]. However, the wave fin type heat exchanger is difficult to manufacture so that the production cost is higher than that of the shell and tube type, and it is vulnerable to fouling due to soot [39].

The off-set fin type EGR cooler has a stacked tube unit that is inserted into the gas discharge channel. Therefore, the EGR cooler reduces the size by as much as 30 % compared with the conventional system [39]. Thermal efficiency is similar to that of the wave fin type [11, 39].

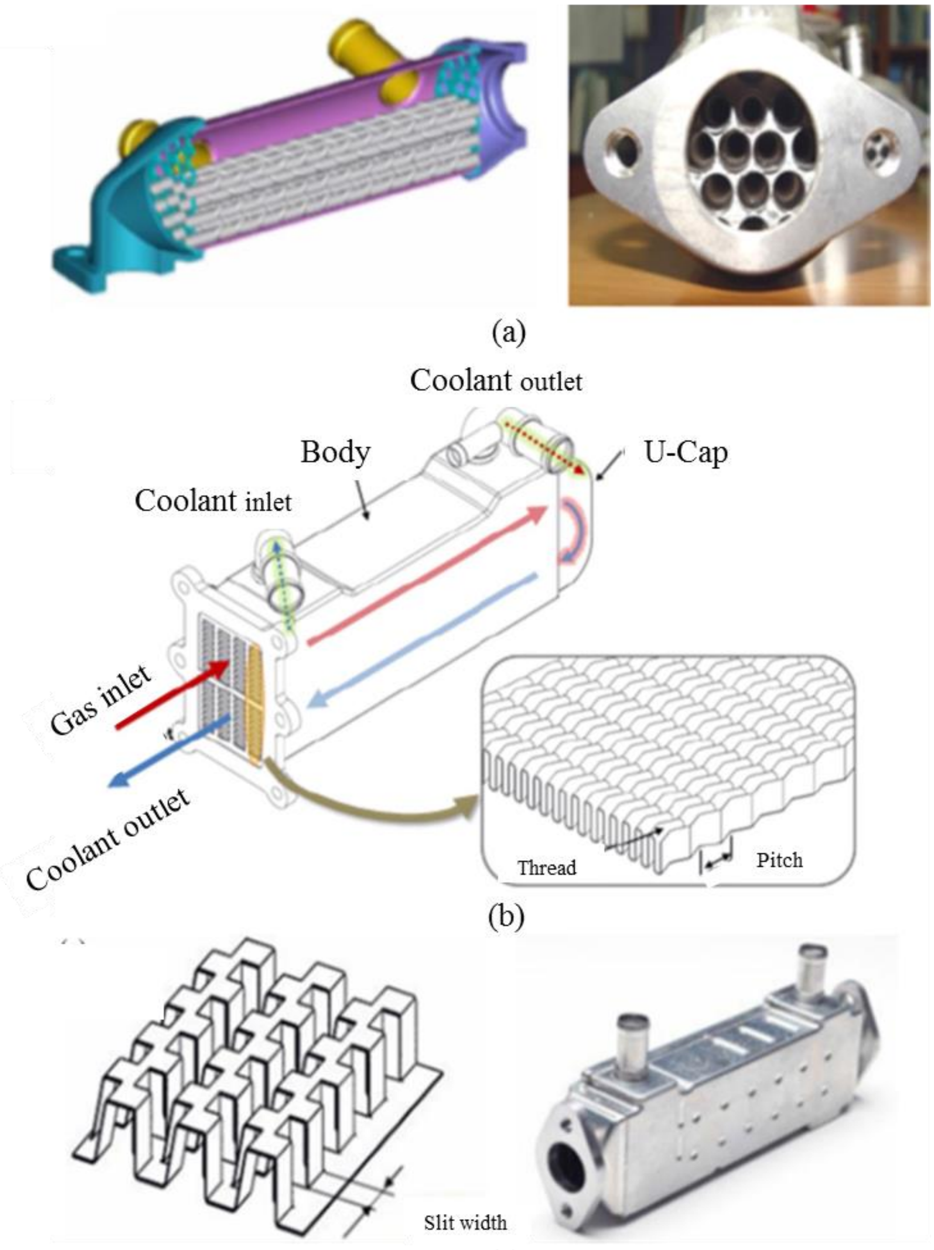

(a)

(b)

(c)

Fig. 1.2.2 Schematic diagrams and photographs of typical EGR coolers.

(a) shell and tube type EGR cooler,

(b) wave fin type EGR cooler,

(c) off-set fin type EGR cooler [1].

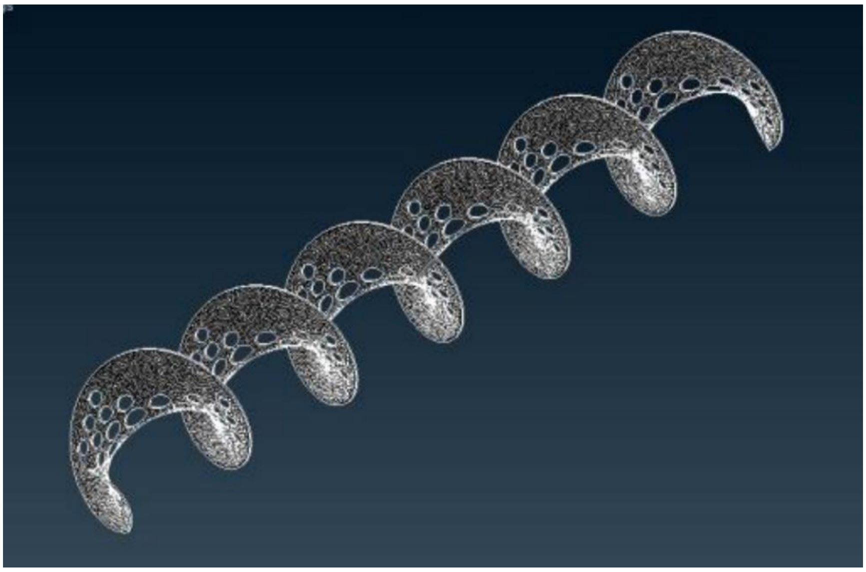

Fig. 1.2.3 Surface mesh with helical baffle [40].

## 1.3 Brazing

Brazing has been used extensively to create attachments between metallic structures and especially successfully for bonding such materials as Ni alloys, steels, and structural ceramics [43]. Compared with conventional welding, brazing can be used to joint dissimilar materials which cannot be joined by fusion processes due to metallurgical incompatibility [44]. In general, brazing produces less thermally distortion than welding due to the uniform heating. In addition, it is possible for brazing to maintain closer assembly tolerances without the costly secondary operations because it produces a clean joint while welded joints must sometimes be ground flush [45]. Another advantage is that brazing can be coated or clad for protective purposes. Moreover, brazing can be easily adopted for mass production [46].

Brazing is not a modern invention. Archaeological evidence shows it has been practiced continuously since ancient times. The method has reemerged as a research topic largely because of its role in the fabrication of large-scale, lattice-based, multifunctional structures shown in Fig. 1.3.1 [43]. Welding is often not feasible for topologically complex systems, and brazing is left as the preferred option [43].

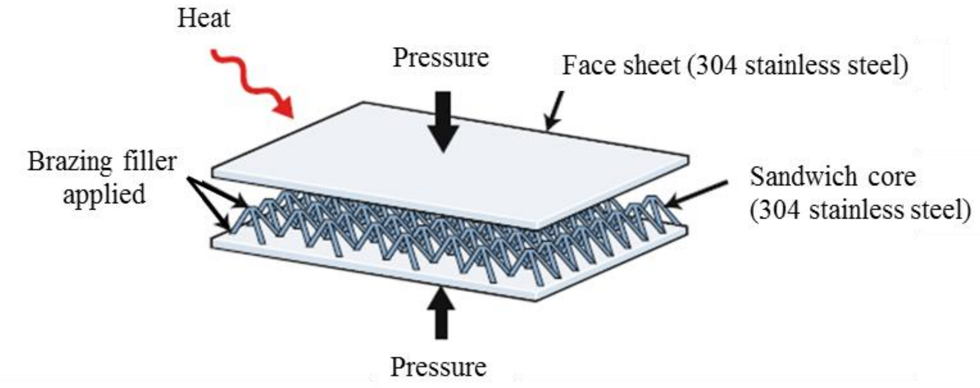

Fig. 1.3.1 Topologically configured sandwich structure with many nodes and thin face sheets.

### 1.4 Stainless steel and Nickel-based filler metals

Stainless steel was at first used as material for decoration trims in automobile. In the past two decades, many automotive components previously fabricated from carbon steels are now fabricated from stainless steels by virtue of its excellent corrosion resistance, heat resistance and good appearance for clean exhaust gas and reduced weight for better fuel economy [47]. Austenitic stainless steels, such as SUS 304 and SUS 316, have being used for automotive components because they are featured with excellent formability, excellent high-temperature strength and good corrosion resistance [48].

Owing to the design complexity, the automotive components such as EGR coolers, catalytic converters and heat exchangers have been fabricated by brazing. Traditional fillers used in brazing stainless steel are classified as Ag-based, Cu-based and Ni-based brazing filler metals [49]. Ag-based brazing filler metals have the advantage of low brazing temperatures. However, high cost and low corrosion resistance are major drawbacks of most Ag-based fillers. Cu-based brazing filler metals have the advantage of low material cost, but poor corrosion resistance prohibits them from certain industrial applications. Nickel-based filler metals can braze any type of high-melting point base metals, including most commonly the AISI 300 and 400 series stainless steels and nickel-based and cobalt-based alloys [50]. AWS A5. 8M/A5. 8-2011 is the most recent and most complete specification system for Ni-based brazing filler metals [50]. It includes 15 Ni-based brazing filler metals and representative chemical compositions specified in JIS are shown in Table 1.4.1 [51]. The traditional brazing filler metals used for automotive stainless steel components are BNi-2 and BNi-5.

BNi-2 allows good flow properties at lower brazing temperatures and finds use for high-strength, heat-resistant joints in assemblies such as turbine blades and jet engine parts [50]. BNi-2 contains a relatively high amount of boron as a melting-point depression element. The boron has a deleterious effect on the stainless steel brazed joint. During the brazing process, the boron diffuses into the thin stainless steel sheet metal and forms $Cr_3B$ precipitates at the base metal [52-54], resulting in erosion of base metal and the lowering of the strength and corrosion resistance of the brazed assembly.

BNi-5 has a high braze temperature range of 1423 to 1473 K that is above the feasible temperature range for many components. BNi-5 is made a choice for high-strength and corrosion resistant joints and finds use in nuclear and other applications where it is necessary to restrain the degradation of brazing layers caused by B containing brazing filler metals.

Table 1.4.1 Chemical compositions and melting properties of AWS Ni-based brazing filler metals.

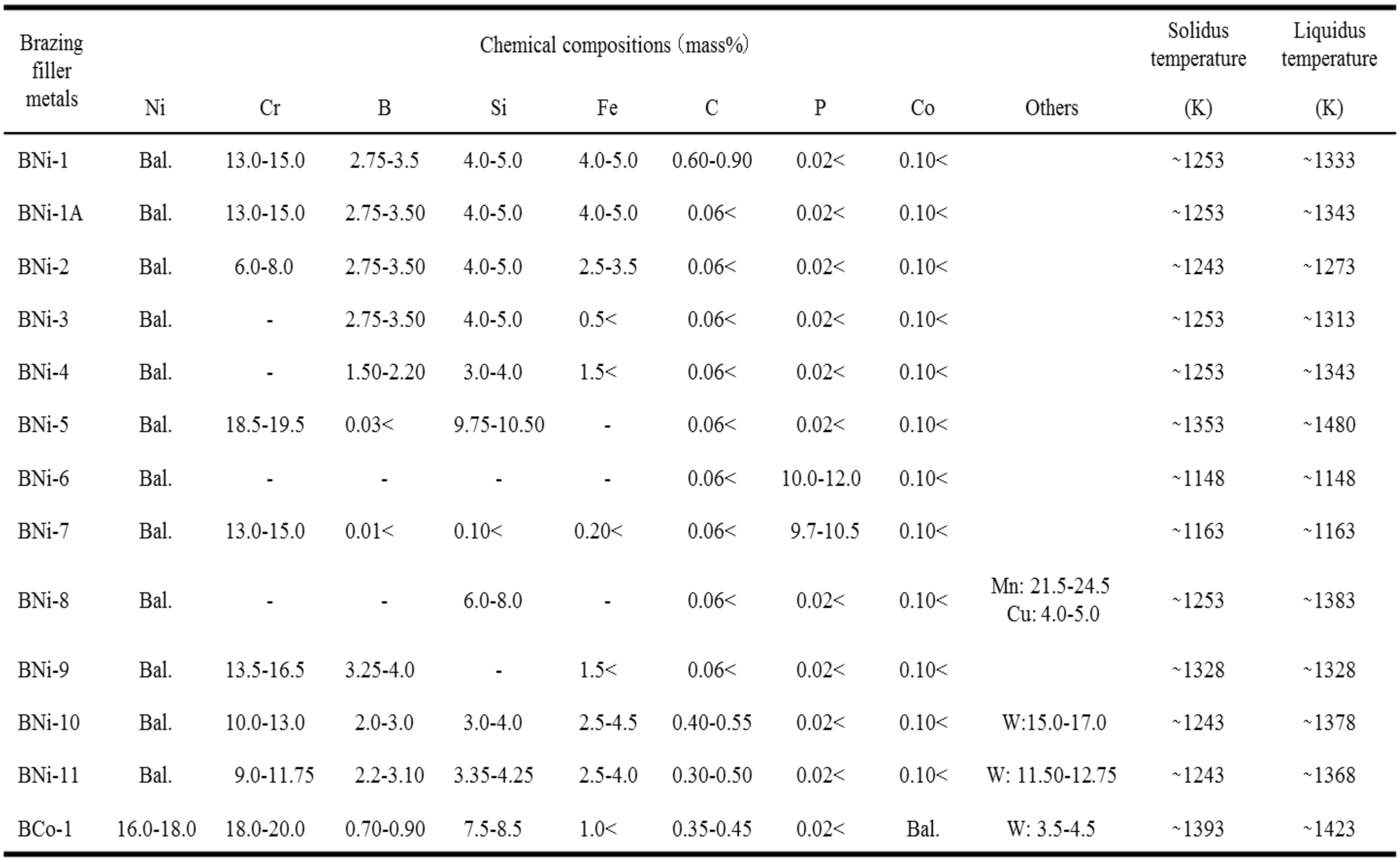

| Brazing filler metals | Chemical compositions（mass%) | | | | | | | | | Solidus temperature | Liquidus temperature |
|---|---|---|---|---|---|---|---|---|---|---|---|
| | Ni | Cr | B | Si | Fe | C | P | Co | Others | (K) | (K) |
| BNi-1 | Bal. | 13.0-15.0 | 2.75-3.5 | 4.0-5.0 | 4.0-5.0 | 0.60-0.90 | 0.02< | 0.10< | | ~1253 | ~1333 |
| BNi-1A | Bal. | 13.0-15.0 | 2.75-3.50 | 4.0-5.0 | 4.0-5.0 | 0.06< | 0.02< | 0.10< | | ~1253 | ~1343 |
| BNi-2 | Bal. | 6.0-8.0 | 2.75-3.50 | 4.0-5.0 | 2.5-3.5 | 0.06< | 0.02< | 0.10< | | ~1243 | ~1273 |
| BNi-3 | Bal. | - | 2.75-3.50 | 4.0-5.0 | 0.5< | 0.06< | 0.02< | 0.10< | | ~1253 | ~1313 |
| BNi-4 | Bal. | - | 1.50-2.20 | 3.0-4.0 | 1.5< | 0.06< | 0.02< | 0.10< | | ~1253 | ~1343 |
| BNi-5 | Bal. | 18.5-19.5 | 0.03< | 9.75-10.50 | - | 0.06< | 0.02< | 0.10< | | ~1353 | ~1480 |
| BNi-6 | Bal. | - | - | - | - | 0.06< | 10.0-12.0 | 0.10< | | ~1148 | ~1148 |
| BNi-7 | Bal. | 13.0-15.0 | 0.01< | 0.10< | 0.20< | 0.06< | 9.7-10.5 | 0.10< | | ~1163 | ~1163 |
| BNi-8 | Bal. | - | - | 6.0-8.0 | - | 0.06< | 0.02< | 0.10< | Mn: 21.5-24.5<br>Cu: 4.0-5.0 | ~1253 | ~1383 |
| BNi-9 | Bal. | 13.5-16.5 | 3.25-4.0 | - | 1.5< | 0.06< | 0.02< | 0.10< | | ~1328 | ~1328 |
| BNi-10 | Bal. | 10.0-13.0 | 2.0-3.0 | 3.0-4.0 | 2.5-4.5 | 0.40-0.55 | 0.02< | 0.10< | W:15.0-17.0 | ~1243 | ~1378 |
| BNi-11 | Bal. | 9.0-11.75 | 2.2-3.10 | 3.35-4.25 | 2.5-4.0 | 0.30-0.50 | 0.02< | 0.10< | W: 11.50-12.75 | ~1243 | ~1368 |
| BCo-1 | 16.0-18.0 | 18.0-20.0 | 0.70-0.90 | 7.5-8.5 | 1.0< | 0.35-0.45 | 0.02< | Bal. | W: 3.5-4.5 | ~1393 | ~1423 |

However, relatively high melting point of BNi-5 induces grain growth in the stainless base metals during the brazing cycle, which may degrade the strength of the sheet metal.

As substitutions for BNi-2 and BNi-5, boron-free/low boron containing brazing filler metals have been developed in the manufacture of brazed stainless steel components. Ni-Cr-Si-P brazing filler metals, such as BrazeLet® Ni 613 (Ni-29Cr-4Si-6P, mass%), Nicrobraz®33 (Ni-29Cr-6.5Si-6P, mass%), VITROBRAZE® VZ2170 (Ni-21Cr-0.5Si-8P-0.5B, mass%) and Amdry 105 (Ni-23Cr-6.5Si-4.5P, mass%), are widely used and have particular importance in the manufacture of EGR units, heat exchangers and catalytic converters. The filler metals contain Si and P for amorphization of structure [55], melting-point depression and wettability improvement [56, 57]. The addition of Si and P may result

in low strength of joints because of the formation of the brittle intermetallic phase of $Ni_3Si$ and phosphides [58-70], respectively. Brazed joints are brittle, therefore burst strength required for components such as heat exchangers cannot always be achieved. At the same time, extreme volatility in the price of nickel has significantly affected the cost and affordability of Ni-based brazing filler metals. This effort is directed towards developing new Fe containing brazing filler metals to overcome the technical and commercial limitations of Ni-based filler metals.

## 1.5 Fe containing brazing filler metals as substitutions for Ni-based brazing filler metals

At present, several Fe containing brazing filler metals have been developed and utilized practically, such as IronBraze™ TB-2720 and TB-4520 from Tokyo Braze Co. Ltd (Japan), VITROBRAZE® VZ2106 and VZ2099 from Vacuumschmelze (Germany), Niferobraz™ 9080 from Wall Colmonoy (USA), BrazeLet® F300 and F302 from Höganäs (Sweden), Amdry 108 and 805 from Sulzer (Switzerland). Chemical compositions and melting properties of them are shown in Table 1.5.1.

IronBraze™ TB-2720 and TB-4520 are B-free, Fe-Cr-based brazing filler metals. They are ideal especially in austenitic stainless steel brazing. Furthermore, B-free can reduce the level of erosion experienced in the case of brazing components of thin sections. However, it was found that joint strength and corrosion resistance characteristics fluctuated when brazing conditions, corrosion solutions and stainless steels were changed [71].

Both VITROBRAZE® VZ2106 and VZ2099 are amorphous brazing foils. These brazing foils alloys are primarily optimized for mass production of heat exchangers made of stainless steel, such as EGR coolers [72]. Compared with amorphous Ni-based filler metals, the prices of these brazing foils are lower because of their lower the Ni content. Joint performance and corrosion resistance are comparable to the well-known high-chromium Ni-based brazing alloys [72].

Niferobraz™ 9080 is a new Fe-based brazing filler metal. The alloy confers excellent resistance to corrosion and high temperature and shows capabilities to perform as well as some nickel base filler metals [36]. The filler metal is well suited for use in brazing applications including heat exchangers, EGR coolers, catalytic converters, fuel cells, and hybrid batteries.

BrazeLet® F300 is a Fe-based brazing filler metal and has excellent wetting properties and low brazing temperature, and creates a uniform joint with high strength, high corrosion resistance and oxidation resistance [73]. BrazeLet® F302 is also a Fe-based filler with a number of advantages, such as cost efficient, wide gap flexibility and high strength and has relatively good corrosion resistance to $H_2SO_4$, superior to $BNi_2$ [74].

Amdry 108 and 805 belong to B-free, high Cr containing filler metals that use relatively small amounts of silicon and phosphorus as melt depressants. Amdry 108 contains approximately 15 mass% Fe. A nominal cost savings could be accomplished without significantly affecting brazeability and high temperature performance. On the other hand, Amdry 805 is a stainless steel-based alloy with a small amount of nickel (15 mass%). The addition of nickel is made to optimize the melting point as well as to retain the austenitic phase structure in the alloy. Based on the significantly lower cost of iron compared with nickel, the raw material costs for Amdry 108 and Amdry 805 will be 30% and 70% less than those of conventional BNi-2 and BNi-5 alloys. These new filler metals are especially suited for brazing in automotive applications and offer technical and commercial advantages particularly in the manufacture of brazed stainless-steel heat exchangers and metallic catalytic converters [75].

Although the disclosed important information on mechanical properties and corrosion resistance of Fe containing brazing filler metals almost comes from technical papers of own company or academic conference, the more persuasive research articles, published in professional journals, have not been found. Moreover, it is found in practice that a smaller clearance is required for some Fe-Cr-based brazing filler metals than that for Ni-based brazing filler metals to obtain appropriate joint strength. In consequence, high production costs arise up owing to small clearance and the size of brazed components is also limited. In addition, corrosion resistance of some Fe containing brazing filler metals fluctuates according to corrosion solutions and type of base metals. In conclusion, there are not convincing research as yet to verify whether these Fe containing brazing filler metals will be comparable to conventional Ni-based brazing filler.

Table 1.5.1 Chemical compositions and melting properties of Fe containing brazing filler metals developed and utilized practically.

| Filler Metal | Chemical Compositions（mass%） | | | | | | | | Solidus temperature | Liquidus temperature |
|---|---|---|---|---|---|---|---|---|---|---|
| | Fe | Cr | Ni | P | Si | Mo | Cu | B | (K) | (K) |
| IronBraze™ TB-2720 | 27 | 20 | 43 | 10 | - | - | - | - | 1283 | 1338 |
| IronBraze™ TB-4520 | 45 | 20 | 20 | 8 | 5 | 2 | - | - | 1293 | 1353 |
| VITROBRAZE® VZ2106 | 35 | 11.0 | 43.6 | - | 6.4 | 1.5 | 1.0 | 1.5 | 1317 | 1427 |
| VITROBRAZE® VZ2099 | 51 | 11.5 | 29 | 1.8 | 2.8 | 1.5 | 0.5 | 1.9 | 1207 | 1419 |
| Niferobraz™ 9080 | 37.5 | 29.5 | 20 | 6 | 7 | - | - | - | Not clear | |
| BrazeLet® F300 | 34 | 24 | 20 | 7 | 5 | - | 10 | - | 1273 | 1343 |
| BrazeLet® F302 | 54 | 15 | 10 | 9 | 7 | - | 5 | - | 1373<br>(Brazing Temperature) | |
| Amdry 108 | 15 | 23 | 51 | 4.5 | 6.5 | - | - | - | 1298 | 1328 |
| Amdry 805 | 43 | 29 | 15 | 6.5 | 6.5 | - | - | - | 1348 | 1378 |

## 1.6 New development trend in brazing filler metals for EGR coolers

Joining of stainless steel components with Ni-based filler metals in vacuum furnaces has been a well-established process in the industry for many decades [30]. In the last years, it is becoming more common for the automotive producers to use continuous conveyer-belt furnaces under controlled atmosphere (shown in Fig. 1.6.1) to braze stainless steels components including EGR coolers due to the lower costs and high efficiency. However, the change has brought two associated challenges [30, 37].

Issue one: compact and complex configurations result in very convoluted, internal areas of the cooler. As a result, the exchange of protective atmosphere and residual oxygen is becoming the key. An inadequate brazing atmosphere leads to defects of the brazed parts, for instance, insufficient strength and leak tightness. This problem is getting even more critical when brazing pastes are used because the decomposition of the organics will cause additional volatile residues during heating up to brazing temperature [35].

Issue two: the temperature of this continuous conveyer-belt furnace is below 1423 K so that BNi-5 (brazing temperature: 1463 K) is not used.

Thus, amorphous brazing foils which contain no organic binders and own the low melting temperature are the preferred brazing filler material for EGR coolers [35].

VITROBRAZE® VZ2099 (shown in Fig. 1.6.2) with 51% Fe is the worldwide first commercialized Fe-based amorphous brazing foil. Both VITROBRAZE® VZ2106 and VZ2099 are available as strip with a width from 0.5 mm to 125 mm and a thickness from 20 μm up to

Fig. 1.6.1 Controlled atmosphere conveyer belt furnace (Tokyo Braze).

50 μm [72]. In addition, IronBraze™ TB-2720 and Amdry 108 and 805 can been provided in the form of foil and used in continuous conveyer-belt furnaces.

Fig. 1.6.2 Variety of different type’s VITROBRAZE® VZ2099 amorphous brazing foils (Vacuumschmelze).

## 1.7 Purposes and scope of this study

Ni-based brazing filler metals have been suffered from high cost in recent years. To reduce the cost of Ni-based filler metals, one of alternative approaches is to replace partial the Ni content by Fe in the brazing filler metals. New Fe-Cr brazing filler metals, extremely decreasing in the Ni content, have been developed as substitutions for expensive Ni-based brazing filler metals. However, mechanical properties and corrosion resistance of the Fe-Cr brazing filler metals are inferior to conventional Ni-based brazing filler, and thus the Fe-Cr based filler metals still need improving or modifying. These problems can only be solved with revealing mechanism on joint strength and corrosion resistance.

This study focuses on the Fe-Cr brazing filler metals and discussed electrochemical characteristics of the Fe-Cr brazing filler metals, joint strength and corrosion behavior of the joints brazed with the Fe-Cr brazing filler metals.

The thesis is divided into five chapters. The relationship among the chapters is presented in Fig. 1.7.1.

In chapter one, environmental problems in recent years and significance of substitution for Ni-based brazing filler metal are explored. The purposes of this study and composition of the thesis are described as well.

In chapter two, the microstructures and melting properties are analyzed for two kinds of new Fe-Cr brazing filler metals, Fe-20Cr-43Ni-10P (mass%) and Fe-20Cr-20Ni-8P-5Si-2Mo (mass%). Electrochemical characterization and corrosion behavior are investigated by electrochemical and surface analysis techniques as well.

In chapter three, SUS304 stainless steel joints are brazed with the Fe-Cr brazing filler metals. Microstructure, joint strength, fracture mechanism and the effect of clearance on shear strength are investigated in order to understand brazing characteristics of the Fe-Cr brazing filler metals.

In chapter four, the scope of this chapter is to investigate the corrosion resistance of stainless steel joints brazed with the Fe-Cr brazing filler metals. To evaluate the corrosion behavior of the joints, immersion tests in artificial compound solutions are performed. The corrosion behavior of the joints are analyzed and compared by means of morphology of corrosion attack, quantitative analysis and penetration depth. This chapter also aims to explore the reasons for the change in corrosion resistance of the brazed joints.

In chapter five, the main findings of this thesis are concluded, and some proposals for further study are offered as well.

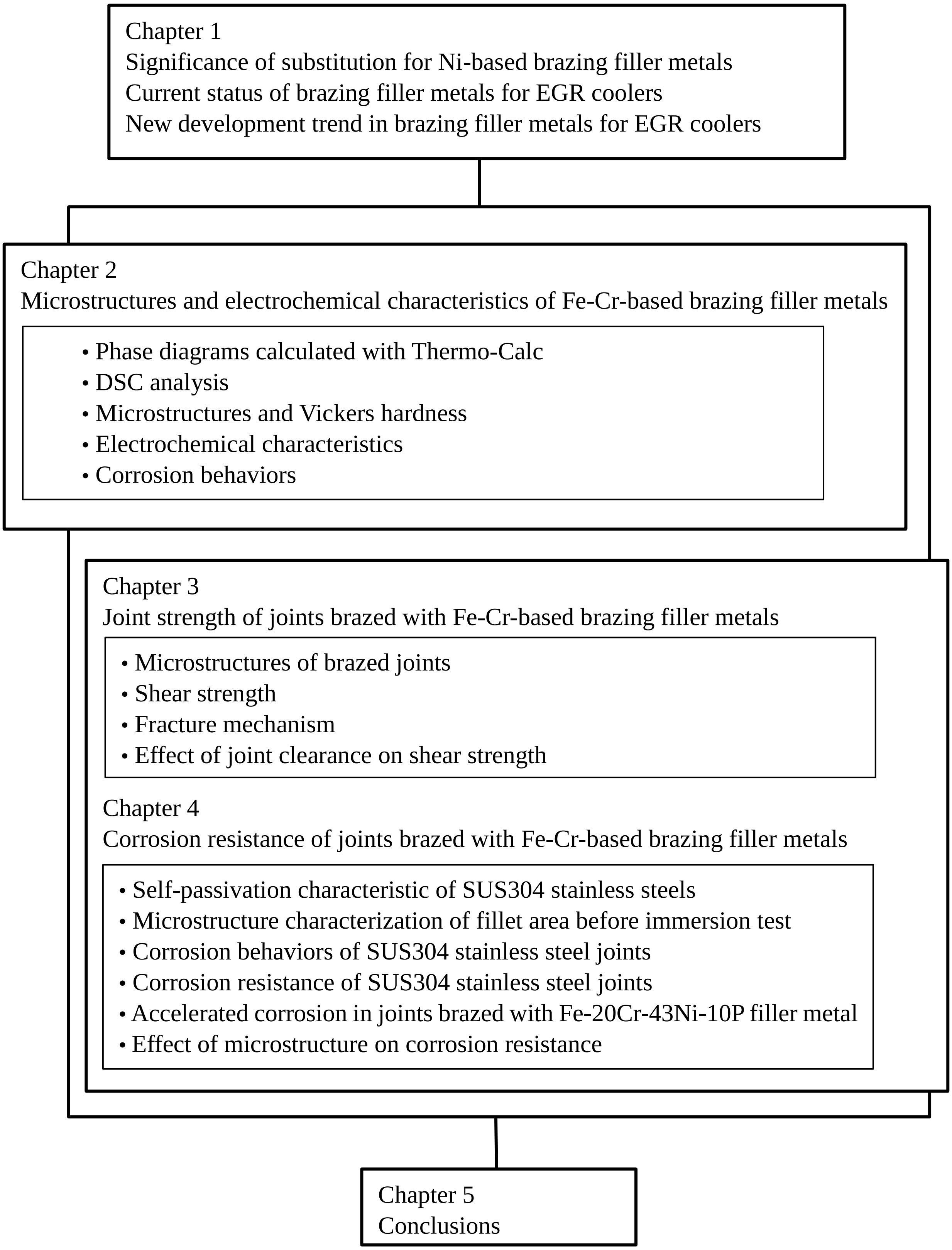

Fig. 1.7.1 Flow chart of this study.

References

[1] K. Nagendra, D.K. Tafti and A.K. Viswanathan: International Journal of Heat and Mass Transfer, **54** (2011) 1671-1681.

[2] L. Liu, X. Ling and H. Peng: Applied Thermal Engineering, **54** (2013) 145-152.

[3] S.C. Heo, Y.H. Seo, T.W. Ku and B.S. Kang: Journal of Mechanical Science and Technology, **25** (2011) 429-439.

[4] L.L.F. Squaiella, C.A. Martins and P.T. Lacava: Fuel, **104** (2013) 183-193.

[5] M.K. Khair: Proceedings of SAE International Future Transportation Technology Conference, (1997) 81-88.

[6] M.S. Abd-Elhady, T. Zornek, M.R. Malayeri, S. Balestrino, P.G. Szymkowicz and H. Muller-Steinhagen: International Journal of Heat and Mass Transfer, **54** (2011) 838-846.

[7] T. Nakada: Journal of the Surface Finishing Society of Japan, **52** (2001) 20-24.

[8] Y. Kiyota: Transactions of the Japan Society of Mechanical Engineers (B), **58** (1992) 3225-3230.

[9] M. Ikegami: Journal of the Japan Institute of Marine Engineering, **36** (2001) 287-292.

[10] G. Sugiyama: Journal of the Japan Institute of Marine Engineering, **43** (2008) 24-28.

[11] S.K. Park, J. Lee and H.M. Kim: Heat Mass Transfer, **50** (2014) 1783-1789.

[12] H.Y. Peng, Y. Cui, L. Shi and K.Y. Deng: Energy, **33** (2008) 471-479.

[13] H.M. Kim, D.H. Lee, S.K. Park, K.S. Choi and H.M. Wang: Journal of Mechanical Science and Technology, **22** (2008) 361-366.

[14] J.M. Wang: Control Engineering Practice, **16** (2008) 1479-1486.

[15] N. Ladommatos, S.M. Abdelhalim, H. Zhao and Z. Hu: SAE Technical Paper 961165, (1996) 35-57.

[16] N. Ladommatos, S.M. Abdelhalim, H. Zhao and Z. Hu: SAE Technical Paper 971659, (1997) 221-235.

[17] A. Maiboom, X. Tauzia and J.F. Hétet: Applied Thermal Engineering, **29** (2009) 2043-2050.

[18] S.H. Jang, S.K. Park, K.S. Choi and H.M. Kim: Heat Mass Transfer, **47** (2011) 621-628.

[19] K.S. Hong, J.S. Park and K.S. Lee: International Journal of Automotive Technology, **12** (2011) 813-820.

[20] K.S. Hong, K.S. Lee, S. Song, K.M. Chun, D. Chung and S. Min: Atmospheric Environment, **45** (2011) 5677-5683.

[21] S.H. Jang, S.J. Hwang, S.K. Park, K.S. Choi and H.M. Kim: Heat Mass Transfer, **48** (2012) 1081-1087.

[22] S. Aldajah, O.O. Ajayi, G.R. Fenske and I.L. Goldblatt: Wear, **263** (2007) 93-98.

[23] G.H. Abd-Alla: Energy Conversion and Management, **43** (2002) 1027-1042.

[24] M. Zheng, G.T. Reader and J.G. Hawley: Energy Conversion and Management, **45** (2004) 883-900.

[25] A. Maiboom, X. Tauzia and J.F. He´ tet: Energy, **33** (2008) 22-34.

[26] G.S. Hebbar and A.K. Bhat: International Journal of Automotive Technology, **14** (2013) 333-341.

[27] D. Agarwal, S.K. Singh and A.K. Agarwal: Applied Energy, **88** (2011) 2900-2907.

[28] T. Miyamoto, H. Hasegawa, M. Mikami, N. Kojima, H. Kabashima and Y. Urata: International Journal of Hydrogen Energy, **36** (2011) 13138-13149.

[29] D.T. Hountalas, G.C. Mavropoulos and K.B. Binder: Energy, **33** (2008) 272-283.

[30] T. Hartmann and D. Nuetzel: Proceedings of the 9th International Conference of Brazing, High Temperature Brazing and Diffusion Bonding, LÖT 2010, (2010) 42-47.

[31] K. Matsu: Welding Technology, **57** (2009) 73-76.

[32] K. Matsu: Welding Technology, **59** (2011) 54-57.

[33] T. Hartmann and D. Nuetzel: Proceedings of the 5th International Brazing and Soldering Conference, (2012) 394-401.

[34] Y. Sasaki: Journal of Gas Turbine Society of Japan, **39** (2011) 224-233.

[35] T. Hartmann and D. Nuetzel: Proceedings of the 4th International Brazing & Soldering Conference, (2009) 110-117.

[36] M. Weinstein, L. Lee, L. Johnson, A. Battenbough and A.M. Osmanda: Technical Paper in Wallcolmonoy, April 2015.

[37] K. Matsu, T. Sawada, S. Fukumoto, Y. Miyazawa and T. Ariga: Proceedings of the 9th International Conference of Brazing, High Temperature Brazing and Diffusion Bonding, LÖT 2010, (2010) 48-51.

[38] K. Matsu: Welding Technology, **56** (2008) 92-95.

[39] S.K. Park, J.K. Lee, K.C. Kim, S.H. Park and H.M. Kim: Heat Mass Transfer, **51** (2015) 1639-1651.

[40] P.S. Gowthaman and S. Sathish: International Journal of Current Engineering and Technology, **2** (2014) 625-628.

[41] Y.Q. Huang, X.L. Yu and G.D. Lu: Journal of Zhejiang University Science A, **9** (2008) 1270-1276.

[42] Y.G. Lei, Y.L. He, P. Chu and R. Li: Chemical Engineering Science, **63** (2008) 4386-4395.

[43] S.K. Park, K.S. Choi, H.M. Kim and K.H. Lee: Heat Mass Transfer, **46** (2010) 1221-1227.

[44] N.R. Philips, C.G. Levi and A.G. Evans: Metallurgical and Materials Transactions A, **39** (2008) 142-149.

[45] S. Zhu, G. Xie, F. Qin, X. Wang and T. Hanawa: Materials Transactions, **54** (2013) 1335-1338.

[46] H. Ström and S. Sasic: Catalysis Today, **188** (2012) 14-23.

[47] O.M. Akselsen: Journal of Materials Science, **27** (1992) 1989-2000.

[48] M. Shabani-Nooshabadi and M.S. Ghandchi: Journal of Industrial and Engineering Chemistry, **31** (2015) 231-237.

[49] Y. Inoue and M. Kikuchi: Nippon Steel Technical Report, **88** (2003) 62-69.

[50] M. Weinstein, R.L. Peaslee and F.M. Miller: Welding Journal, **4** (2009) 59-61.

[51] T. Onzawa and T. Matsu: Hajimetenoroduke, (2013) 136.

[52] T. Takemoto: Journal of the Japan Welding Society, **61** (1992) 67-74.

[53] A. Rabinkin, E. Wenski and A. Ribaudo: Welding Research Supplement, **2** (1998) 66-75.

[54] Y. Miyazawa and T. Ariga: Welding Research Supplement, **6** (1993) 294-300.

[55] X.W. Wu, R.S. Chandela, H. Li, H.P. Seowa and S.C. Wu: Journal of Materials Processing Technology, **104** (2000) 34-43.

[56] T. Onzawa and K. Sasabe: Journal of the Japan Welding Society, **69** (2000) 45-53.

[57] G. Stratford, A. Battenbouch, L. Lee and M. Weinstein: Welding Journal, **3** (2011) 54-59.

[58] T. Watanabe, K. Wakatsuki, A. Yanagisawa and T. Sasaki: Quarterly Journal of the Japan Welding Society, **29** (2011) 241-247.

[59] X.W. Wu, R.S. Chandel, H.P. Seow and H. Li: Journal of Materials Processing Technology, **113** (2001) 215-221.

[60] Y.N. Lia, M.I. Osendi and P. Miranzo: Journal of the American Ceramic Society, **86** (2003) 1226-1229.

[61] G. Dehm, B. Medres, L. Shepeleva, C. Scheu, M. Bamberger, B.L. Mordike, S. Mordike, G. Ryk, G. Halperin and I. Etsion: Wear, **18** (1999) 225-229.

[62] C.Y. Su, C.P. Chou, W.J. Chang and M.H. Liu: Journal of Materials Engineering and Performance, **9** (2000) 663-668.

[63] I.W. Donald and H.A. Davies: Journal of Materials Science, **15** (1980) 2754-2760.

[64] F. Fernandes, B. Lopes, A. Cavaleiro, A. Ramalho and A. Loureiro: Surface and Coatings Technology, **205** (2011) 4094-4106.

[65] G.Q. Xie, D.V. L. Luzgina, H. Kimura and A. Inoue: Intermetallics, **18** (2010) 851-858.

[66] W.S. Chen and R.K. Shiue: ISIJ International, **52** (2012) 939-941.

[67] R.K. Roya, A.K. Panda, S.K. Das, Govind and A. Mitra: Materials Science and Engineering A, **523** (2009) 312-315.

[68] N. Wu, Y.J. Li, J. Wang and U.A. Puchkov: Journal of Materials Processing Technology, **212** (2012) 794-800.

[69] Y. Hisamori: Quarterly Journal of the Japan Welding Society, **10** (1992) 211-216.

[70] C.L. Ou, D.W. Liaw, Y.C. Du and R.K. Shiue: Journal of Materials Science, **41** (2006) 6353-6361.

[71] K. Matsu: Proceedings of International Symposium on Interfacial Joining and Surface Technology Solid State Joining, Brazing and Soldering, Surface Treatment, Advanced Packaging, (2013) 17-18.

[72] VACUUMSCHMELZE GmbH & Co. KG: Technical Data Sheet Edition 01 (2014).

[73] Hoganas AB (publ.): Technical Data Sheet 0028HOG (2012).

[74] Hoganas AB (publ.): Technical Data Sheet 0158HOG (2012).

[75] Sulzer Metco (US) Inc.: Sulzer Technical Review (2008).

# Chapter 2 Microstructures and electrochemical characteristics of Fe-Cr-based brazing filler metals

## 2.1 Introduction

Modern exhaust gas recirculation (EGR) designs employ thinner wall sections and more variable gap tolerances than previous models. Consequently, it is essential that brazing filler metals provide good flow, gap filling performance with minimal erosion in addition to sufficient mechanical strength, corrosion resistance and high temperature performance characteristics [1].

IronBraze$^{TM}$ TB-2720 (Fe-20Cr-43Ni-10P, mass%) and TB-4520 (Fe-20Cr-20Ni-8P-5Si-2Mo, mass%) are B-free brazing filler metals (refer to Table 1.5.1). B-free reduces the level of erosion for components with thin sections because the boron diffuses into thin stainless steel sheets and forms $Cr_3B$ precipitates at the stainless steel base metals. Although P may result in low strength of joints because of the formation of the brittle phosphides [2-14], it is necessary to add P because the effect of melting-point depression is stronger than B or Si in iron. In binary systems, the effect is about 28.8 K/mol% for Fe-P, whereas boron shows 21.4 K/mol% for the Fe-B system and silicon only 10.5 K/mol% for Fe-Si alloys [15]. Moreover, P provides a good amorphous state catalyst [16, 17] and wettability improvement [18, 19], and acts like a solvent during the brazing process. In the case of TB-4520, 5 % Si is added to replace a part of P addition for melting-point depression because Si can be dissolved in Ni or Fe by 8-10% [20] and avoid the formation of the brittle intermetallic phase of $Ni_3Si$. At the same time, Mo is added to obtain fine microstructure and corrosion resistance improvement [21-23].

In this chapter, melting properties, microstructures and micro hardness of phases are analyzed for Fe-20Cr-43Ni-10P (mass%) and Fe-20Cr-20Ni-8P-5Si-2Mo (mass%). Electrochemical characteristics and corrosion behaviors are investigated by electrochemical and surface analysis techniques as well.

## 2.2 Experimental procedure

### 2.2.1. Materials and electrolyte solution

The brazing filler metals, which are Fe-20Cr-43Ni-10P and Fe-20Cr-20Ni-8P-5Si-2Mo, were produced by conventional ingot metallurgy. The powders of Fe, Ni, Cr, P, Si and Mo, having a purity of 99.9%, were prepared. The particle sizes of the powders were less than 106 μm. The powders were mixed according to the ratio shown in Table 1.5.1. The mixed powders were put in the alumina molds respectively and melted in a hydrogen furnace at 1373 K for 10 minutes. For comparison, Ni-29Cr-6P-4Si (mass%) was also prepared in the same way. The alloy ingots were cooled to room temperature in air and cut in half. One half was used for the differential scanning calorimeter (DSC) analysis and electrochemical measurement. The other was used as the specimen for the microstructure analysis.

The base metal used in the experiment was commercial SUS304 stainless steel sheet with the thickness of 1 mm. Its chemical compositions are given in Table 2.2.1.

Table 2.2.1 Chemical compositions of base metal (mass%).

| The base metal | C | Si | Mn | P | S | Ni | Cr | Fe |
|---|---|---|---|---|---|---|---|---|
| SUS304 | 0.05 | 0.38 | 1.86 | 0.035 | 0.025 | 8.17 | 18.5 | bal. |

In accordance with the standards of the Automobile Manufacturers Association of Germany [24], electrolyte solution was made as follows: 1650 mg NaCl, 3.4 ml nitric acid (60%) and 1.4 ml sulphuric acid (98.08%) were added into 500 ml $H_2O$, and then $H_2O$ was added to form 1000 ml aqueous solution. The pH value of the solution was 1.0 by pH test paper (accuracy class 0.3).

### 2.2.2 Phase diagrams calculated with Thermo-Calc

The amounts of Fe, Cr, Si and Mo were fixed in accordance with the compositions of the brazing filler metals. By changing the Ni and P content, phase diagrams were calculated with Thermo-Calc 2015a for Fe-Cr-Ni-P and Fe-Cr-Ni-P-Si-Mo system alloys. Databases used were SSOL5 and SSUB5. Liquidus temperatures and phase compositions were predicted for Fe-Cr-Ni-P and Fe-Cr-Ni-P-Si-Mo system alloys.

### 2.2.3 DSC analysis

Approximately 30 mg brazing filler metals were cut from the ingots and inserted into ceramic crucibles for DSC analysis. DSC analysis was carried out from 923 K to 1450 K at the heating rate of 10 K/min in an atmosphere of nitrogen (10 mL /min), followed by cooling to 923 K at the same rate.

### 2.2.4 Microstructure analysis and Vickers hardness test

The specimens were prepared for microstructure analysis according to the standard metallographic techniques. The ingots were buried in an epoxy resin and cut with a fine cutter as the specimens for microstructure analysis. The cross-sections of the specimens were abraded in, #100, #400, #800, #1200, #2400 and #4000 grit emery papers and then polished by 1.0 μm aluminum suspension. The microstructure analysis was carried out by an electron probe X-ray micro analyzer (EPMA).

Vickers hardness was obtained using a Vickers diamond indentator at a 100 gf load for 15 seconds. Vickers hardness test was performed for five times on every analyses area, and then the average was took.

### 2.2.5 Electrochemical measurement

The specimen in the electrochemical test is shown in Fig. 2.2.1. The brazing filler metal ingots of approximately 300 mg were placed on SUS304 stainless steel plates (40 mm×40 mm×2 mm) respectively. The plates were carefully put into a semicontinuous vacuum furnace. The ingots were melted at 1373 K for 30 minutes in a vacuum degree of 50 Pa. Then, the SUS304 stainless steel plates were slowly cooled to 1173 K at a cooling rate of approximately 7 K/min, followed by quenching to room temperature at a cooling rate of approximately 15 K/min in a nitrogen atmosphere (5 L /min). Subsequently, they were cut out into 15 mm×15 mm chips, and coated with epoxy resin with an area of 1 cm$^2$ area remaining uncoated.

Both potentiodynamic polarization test and constant potential polarization test were performed by the standard three-electrode method at room temperature. The counter electrode was a thin platinum piece. The reference electrode was a silver-silver chloride electrode (SSE) and linked to the test cell through a salt bridge. All potentials were referred to the SSE electrode. The solution was deaerated with nitrogen gas during the tests (10 mL/min). The open circuit potential (OCP) was monitored. When the change of the OCP was less than 10 mV/hour, the

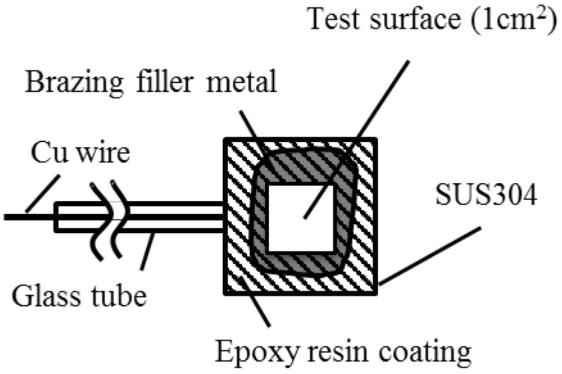

Fig. 2.2.1 Schematic view of specimen for electrochemical test.

potentiodynamic polarization test was performed. The scan started from 200 mV below the OCP and swept toward more positive potential. The scan rate was 0.2 mV/sec. For every test condition, the result was repeated 2 times for repeatability and reliability.

At a potential of -0.11 V-SSE and -0.17 V-SSE for Fe-20Cr-43Ni-10P and Fe-20Cr-20Ni-8P-5Si-2Mo respectively, constant potential polarization tests were performed for 3 h, 10 h, 50 h and 100 h.

The surfaces of the specimens after constant potential polarization tests were analyzed using a field emission scanning electron microscopy (FE-SEM) and the EPMA.

## 2.3 Results and discussion

### 2.3.1 Phase diagrams calculated with Thermo-Calc

Calculated phase diagrams when the Ni and P contents were changed are shown in Fig. 2.3.1. For 27Fe-20Cr-Ni-P, the calculated ratio of Fe: Cr: Ni: P in the eutectic structure is 27: 20: 44.5: 8.5 and the calculated eutectic temperature of the eutectic structure is 1224 K. According to the calculated phase diagrams, Fe-20Cr-43Ni-10P is a hypereutectic alloy and consists of a solid-solution phase and phosphide phase. Calculated liquidus temperature is 1267 K.

For 45Fe-20Cr-5Si-2Mo-Ni-P, the calculated ratio of Fe: Cr: Si: Mo: Ni: P in the eutectic structure is 45: 20: 5: 2: 23: 5 and calculated eutectic temperature of the eutectic structure is 1361 K. Based on the calculated results, Fe-20Cr-20Ni-8P-5Si-2Mo is a hypereutectic alloy and consists of a solid-solution phase and phosphide phase as also. Calculated liquidus temperature is 1445 K.

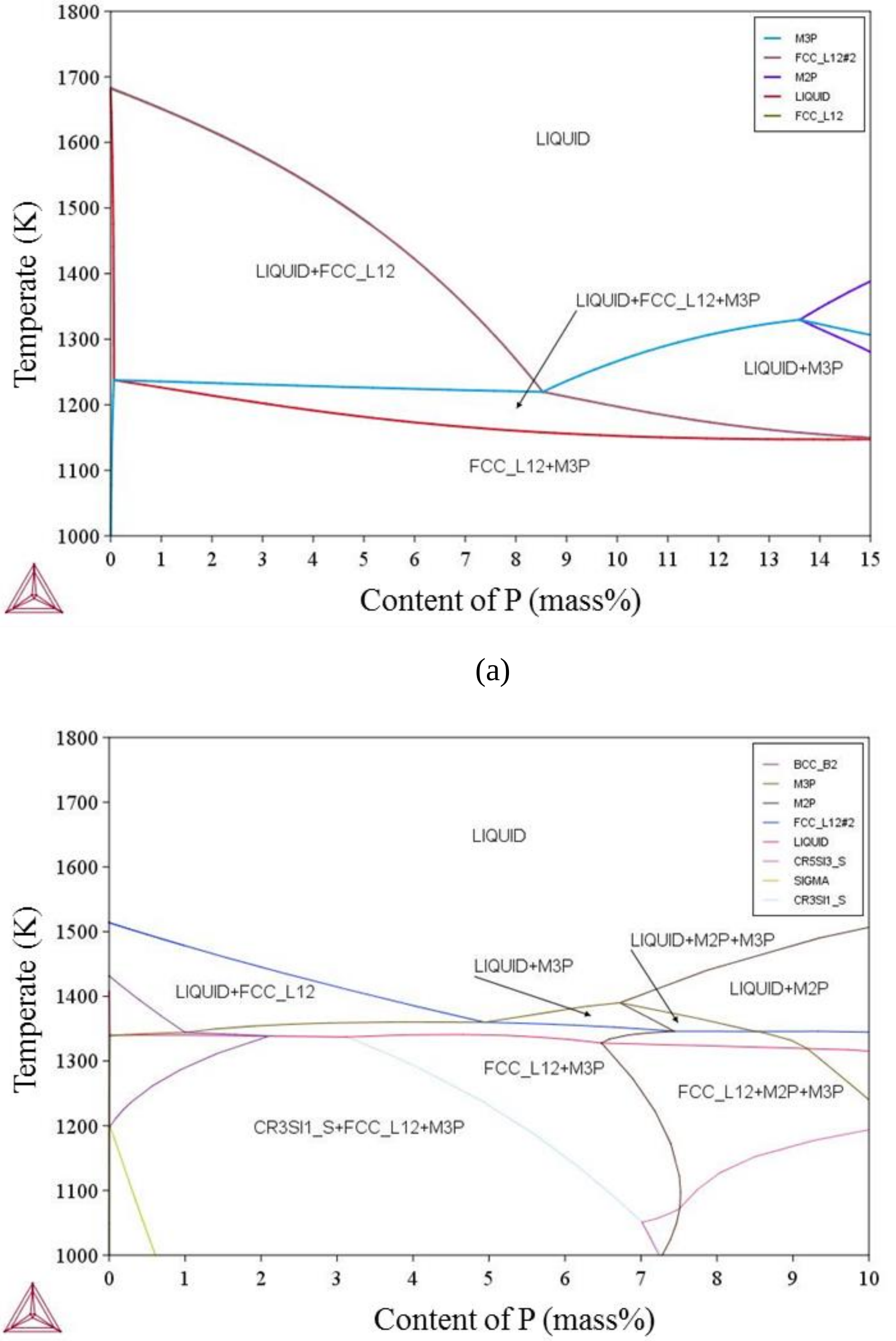

(a)

(b)

Fig. 2.3.1 Calculated phase diagrams when Ni and P contents are changed. (a) 27Fe-20Cr-Ni-P, (b) 45Fe-20Cr-5Si-2Mo-Ni-P.

### 2.3.2 DSC analysis

The obtained DSC curves are shown in Fig. 2.3.2. On the basis of the DSC analysis, the solidus and liquidus temperatures for each brazing filler metal were obtained. These values are presented in Table 2.3.1. In the table, the calculated liquidus temperatures with Thermo-Calc are also presented.

Table 2.3.1 Solidus and liquidus temperatures from DSC analysis and calculated liquidus temperatures.

| Brazing filler metal (mass%) | Solidus temperature (K) | Liquidus temperature (K) | Calculated liquidus temperature (K) |
|---|---|---|---|
| Ni-29Cr-6P-4Si | 1259 | 1297 | -- |
| Fe-20Cr-43Ni-10P | 1175 | 1313 | 1267 |
| Fe-20Cr-20Ni-8P-5Si-2Mo | 1328 | 1359 | 1445 |

For Fe-20Cr-43Ni-10P, the measured liquidus temperature is 46 K higher than the calculated liquidus temperature, but is 1313 K and much close to the liquidus temperature of Ni-29Cr-6P-4Si (1297 K). Furthermore, it exhibits an extended melting range of 138 K while the melting range of Ni-29Cr-6P-4Si and Fe-20Cr-20Ni-8P-5Si-2Mo is 38 K and 31 K, respectively. Wide solidus/liquidus temperature range often indicates the ability to fill larger joint clearances.

For Fe-20Cr-20Ni-8P-5Si-2Mo, the measured liquidus temperature is 86 K lower than the calculated liquidus temperature, and 62 K higher than the liquidus temperature of Ni-29Cr-6P-4Si (1297 K). As shown in Fig. 2.3.2 (c), two distinct exothermic peaks are very close to each other in the cooling curve. This implies that Fe-20Cr-20Ni-8P-5Si-2Mo has a narrower solid-liquid two-phase region than that shown in Fig. 2.3.1 (b). Therefore, it is possible that some $M_2P$ melted in ‘liquid + $M_2P$’ phase region shown in Fig. 2.3.1 (b), resulting in a large difference between the measured and calculated liquidus temperatures.

In terms of the cooling curves, Ni-29Cr-6P-4Si shows one extinct exothermic event and a weak exothermic peak (marked with a circle), but an endothermic peak corresponding to the weak exothermic peak is not observed in the heating curve. Fe-20Cr-43Ni-10P indicates two distinct exothermic events and a weak exothermic peak (marked with a circle), and there is also an endothermic peak to correspond to the weak exothermic peak in the heating curve. In contrast, Fe-20Cr-20Ni-8P-5Si-2Mo only shows two close exothermic events. The phenomenon will be discussed in 2.3.3, combined with the microstructures.

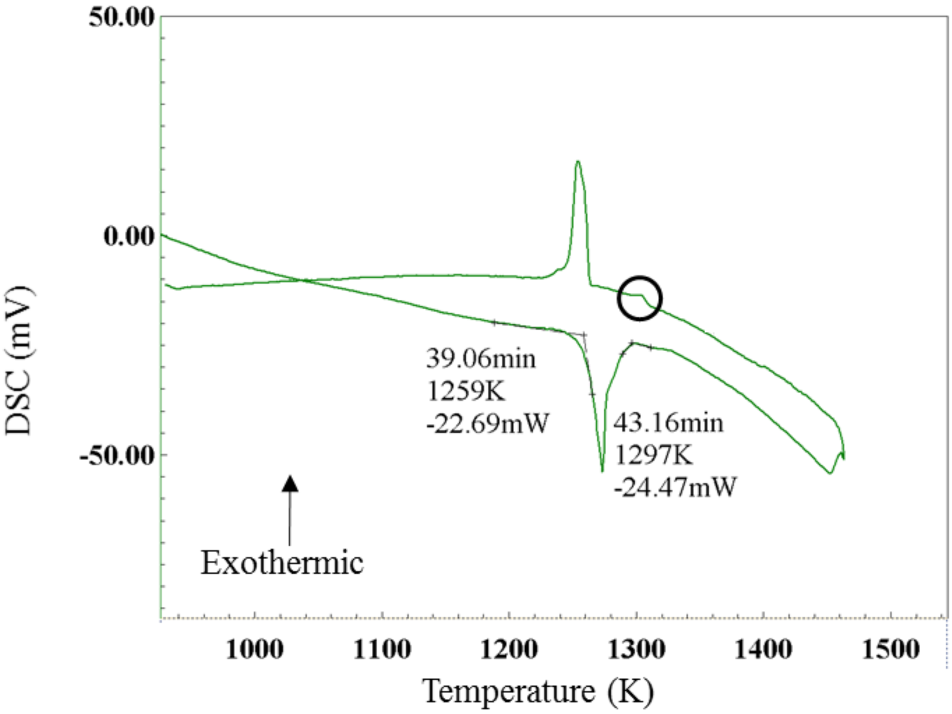

(a)

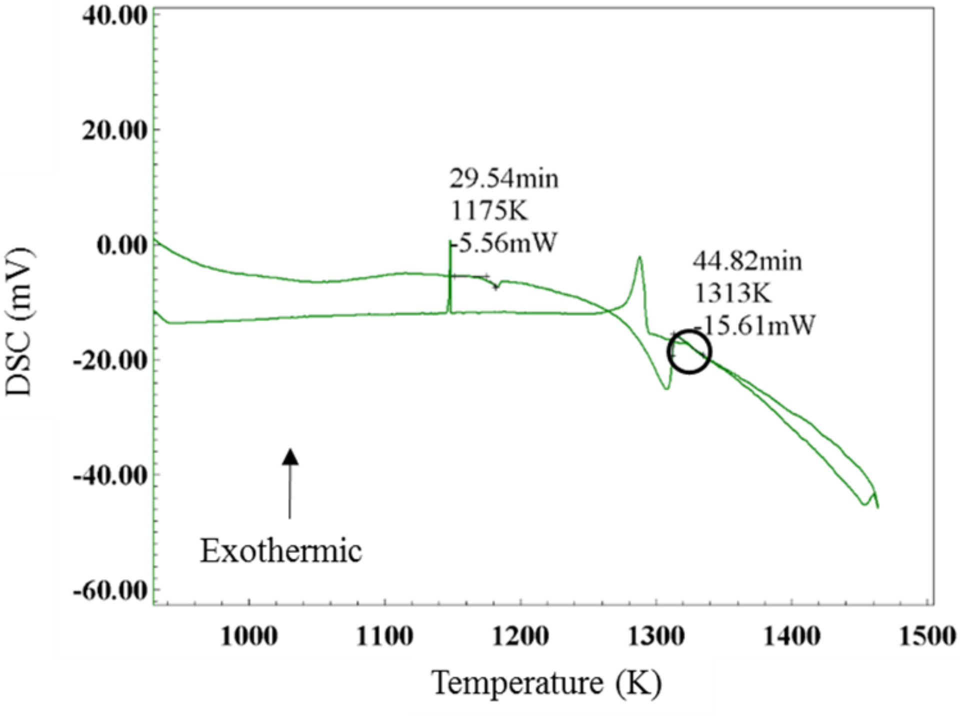

(b)

Fig. 2.3.2 DSC curves of brazing filler metals. (a) Ni-29Cr-6P-4Si, (b) Fe-20Cr-43Ni-10P.

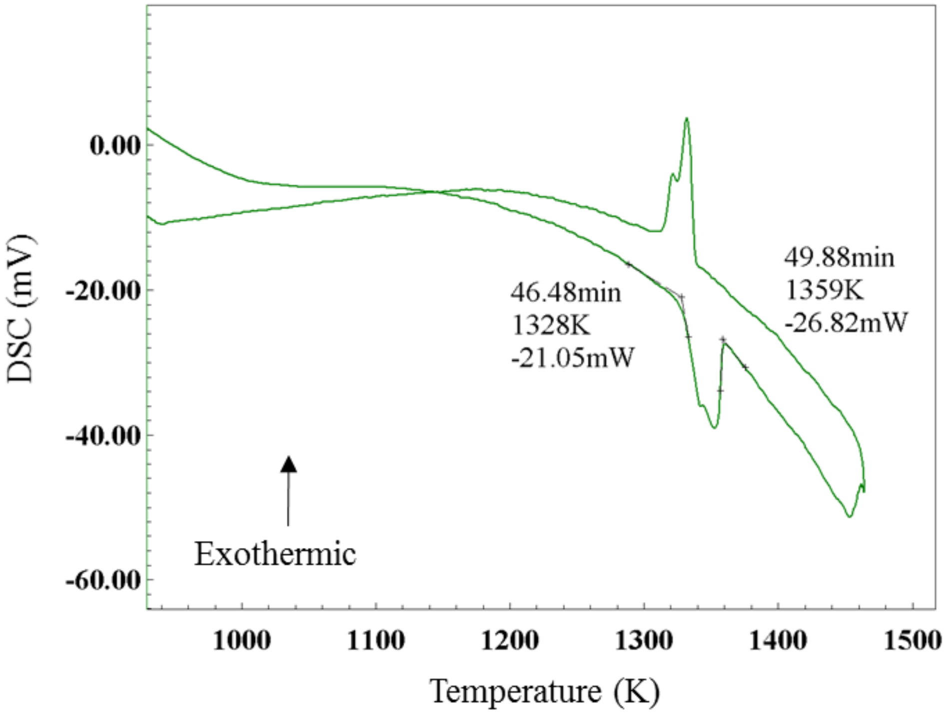

(c)

Fig. 2.3.2 DSC curves of brazing filler metals. (a) Ni-29Cr-6P-4Si, (b) Fe-20Cr-43Ni-10P, (c) Fe-20Cr-20Ni-8P-5Si-2Mo.

### 2.3.3 Microstructures and Vickers hardness

Back-scattered electron images of the brazing filler metals are shown in Fig. 2.3.3. Dark gray phases and bright gray phases are observed in all the brazing filler metals. Meanwhile, the bright gray phase consists of coarse and fine phases in all the brazing filler metals. In addition, some phases are observed in small amounts marked with a circle in all the brazing filler metals.

Fig. 2.3.4 shows mapping analysis results for cross sections of every brazing filler metals. Each element is unevenly distributed in the light gray or dark gray phase in all the brazing filler metals.

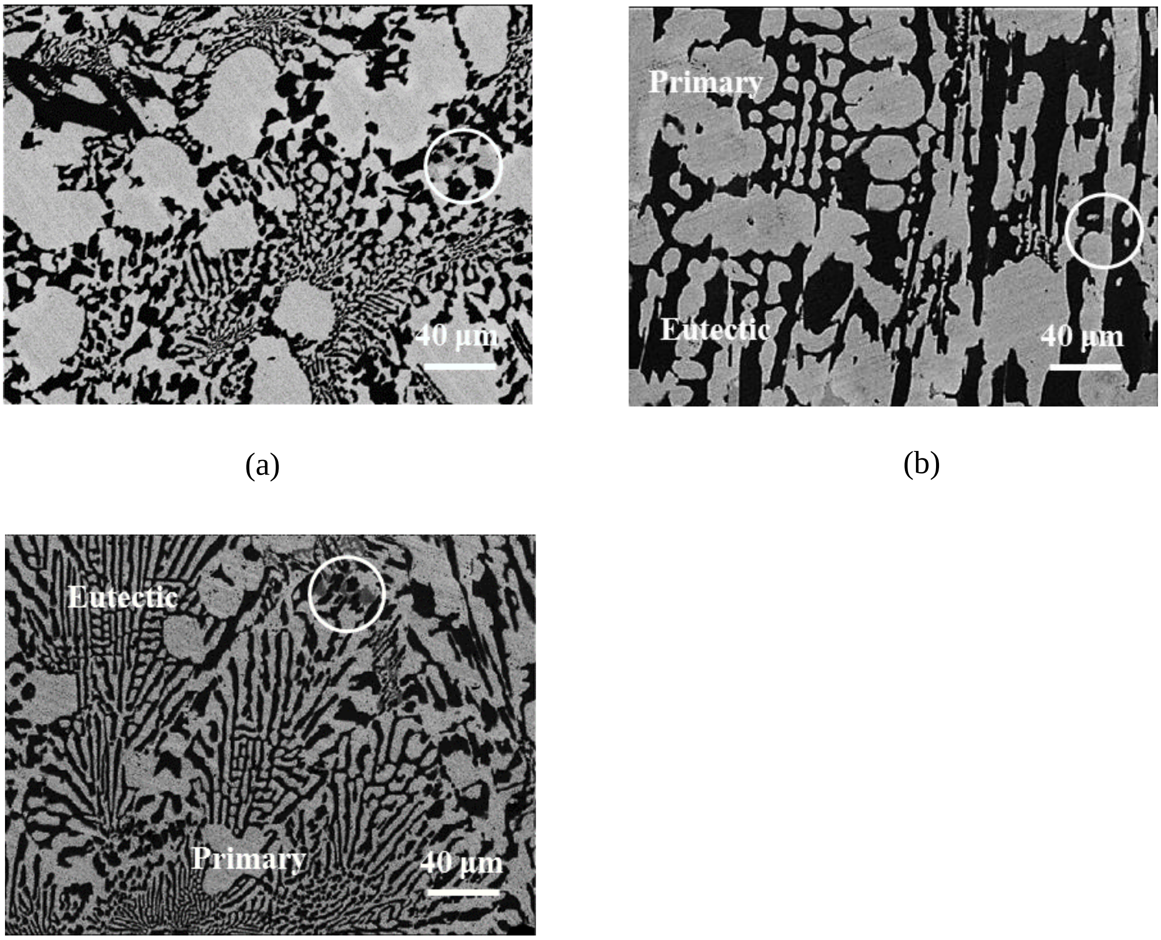

(a) (b)

(c)

Fig. 2.3.3 Microstructures of cross sections of as-cast brazing filler metals (back-scattered electron images). (a) Ni-29Cr-6P-4Si, (b) Fe-20Cr-43Ni-10P, (c) Fe-20Cr-20Ni-8P-5Si-2Mo.

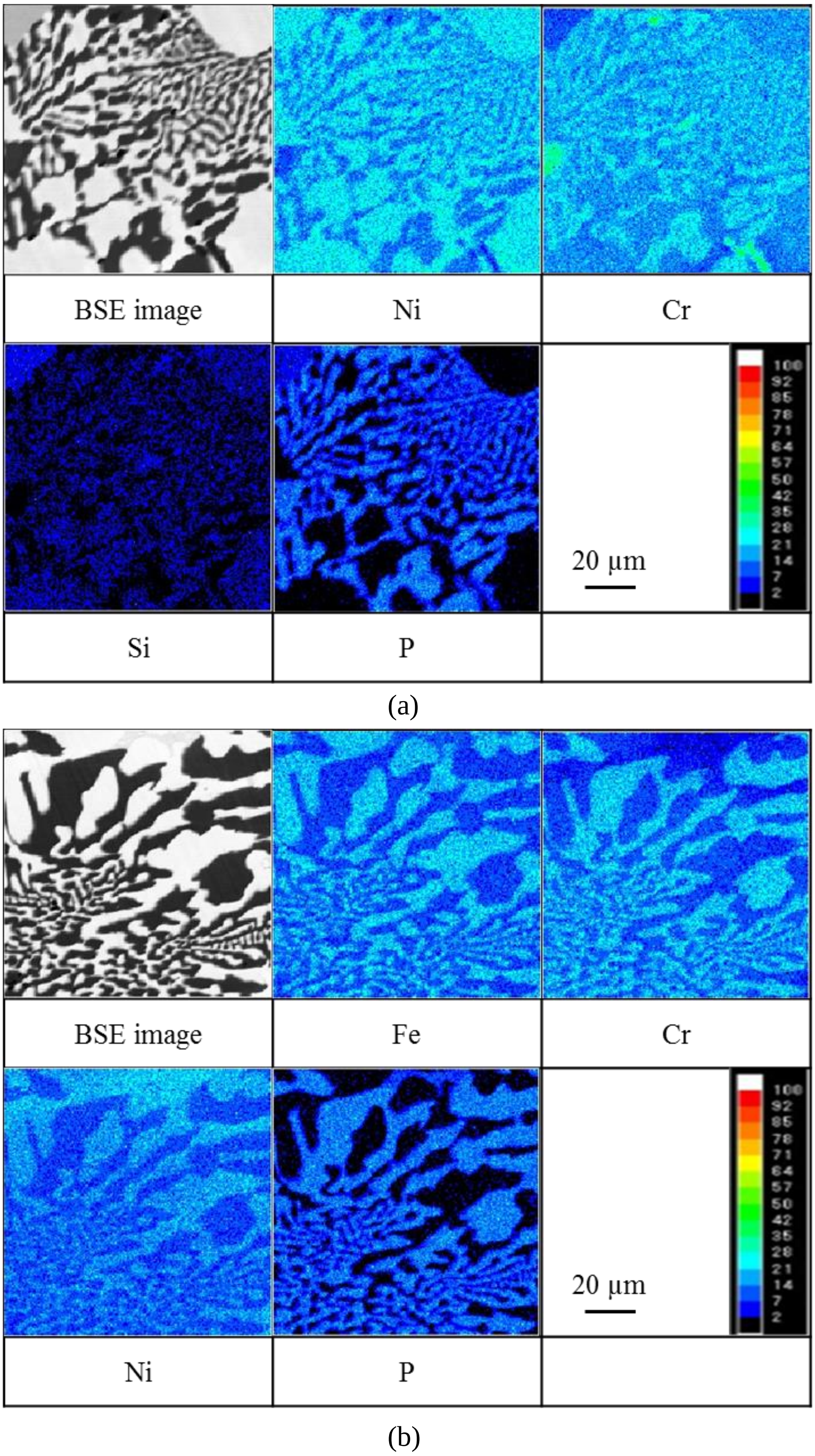

Fig. 2.3.4 Mapping analysis results for cross sections of as-cast filler metals. (a) Ni-29Cr-6P-4Si, (b) Fe-20Cr-43Ni-10P.

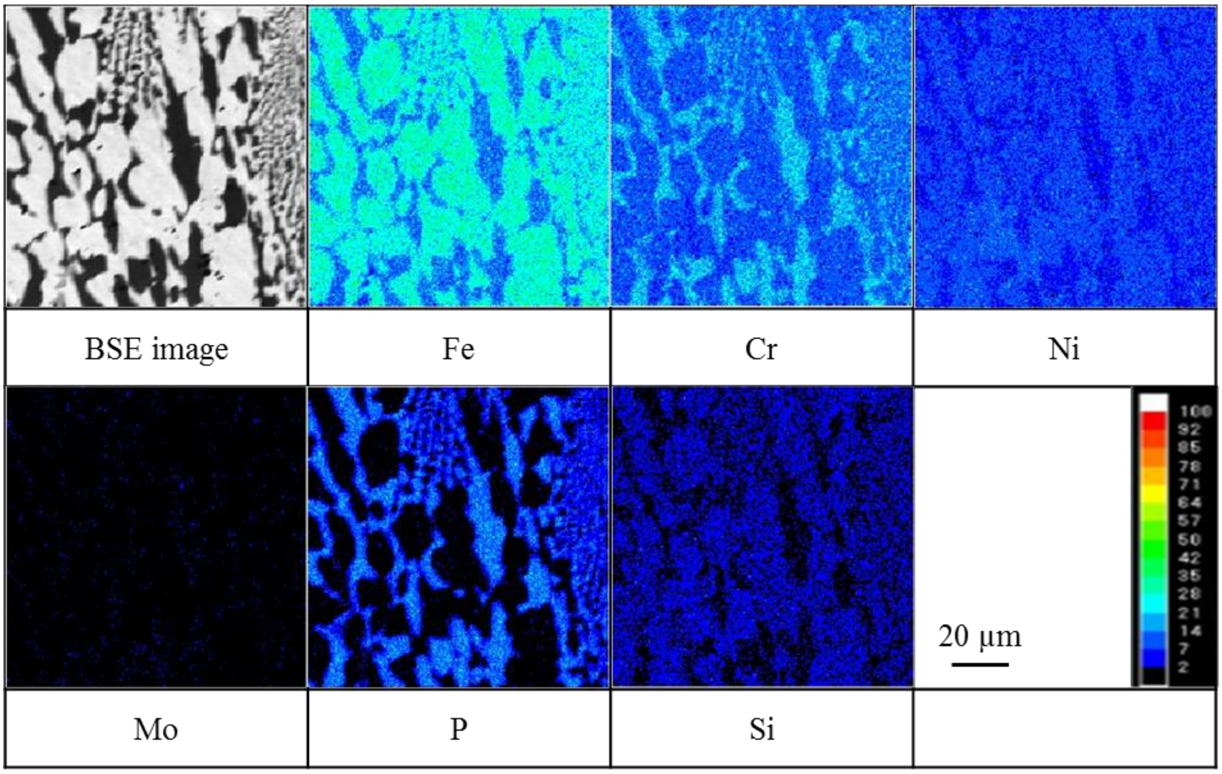

(c)

Fig. 2.3.4 Mapping analysis results for cross sections of as-cast filler metals. (a) Ni-29Cr-6P-4Si, (b) Fe-20Cr-43Ni-10P, (c) Fe-20Cr-20Ni-8P-5Si-2Mo.

#### 2.3.3.1 Ni-29Cr-6P-4Si filler metal

As shown in Fig. 2.3.4 (a), for Ni-29Cr-6P-4Si, Ni is observed to be remarkably present in the light gray phase. Cr is the less in the light gray phase than in the dark gray phase. On the other hand, it is observed that P is almost segregated into the dark gray phase and Si is almost segregated into the light gray phase. Table 2.3.2 and 2.3.3 show the chemical compositions and Vickers hardness of the phases in Ni-29Cr-6P-4Si, respectively. The coarse and fine light gray phases are of almost same the chemical compositions and Vickers hardness. Due to the segregation of elements, the compositions of all the phases are different from that in the brazing filler metal. In particularly, the P content in the dark gray phase is 23.3 mass% and much higher than 6 mass% of that in the filler metal. It is confirmed that P is enriched in the dark gray phase. Enrichment of P results in Vickers hardness of 424.6 HV in the dark gray phase. From the quantitative analysis result, the light gray phase is a Ni-Cr-Si solid-solution phase and the dark gray phase is a Ni-Cr-P based phosphide phase.

The Ni: Cr: Si: P ratio of the phase marked with ④ in Table 2.3.2. is 67.4:17.0: 6.1: 9.5 (mass%). Compared with the solid-solution phase in Ni-29Cr-6P-4Si, the Ni content is almost same, the Cr content is low and the contents of Si and P are high. Compared with the Ni-Cr-P based phosphide phase in Ni-29Cr-6P-4Si, the contents of Ni and Si are high and the contents of Cr and P are low. It is clear that the Cr content in the phase is lower than that in both the solid-solution phase and phosphide phase in Ni-29Cr-6P-4Si. Furthermore, the phase is not found in the specimen in the electrochemical measurement shown in Fig. 2.3.5, in the brazing layer shown in Fig. 2.3.6 and in the fillet area shown in Fig. 4.3.17 (a). The three microstructures were obtained after Ni-29Cr-6P-4Si was melt at the brazing temperature of 1373 K for 10 minutes (see 2.2.1) or 30 minutes (see 3.2.3 and 4.2.1). In other words, the phase disappeared because of each element fully diffusing after the longer heating time. Hence, the phase is confirmed an abnormal phase formed because of localized Cr deficiency during the ingot process.

Connecting with the DSC results shown in Fig. 2.3.2 (a), the weak exothermic peak (1305 K) corresponds to the formation of the abnormal phase, and there is not a corresponding endothermic peak in the heating curve because the abnormal phase is not a stable phase. The extinct exothermic peak corresponds to the formation of a eutectic structure. It is indicated that Ni-29Cr-6P-4Si is a eutectic alloy.

Table 2.3.2 Chemical compositions of phases in Ni-29Cr-6P-4Si filler metal.

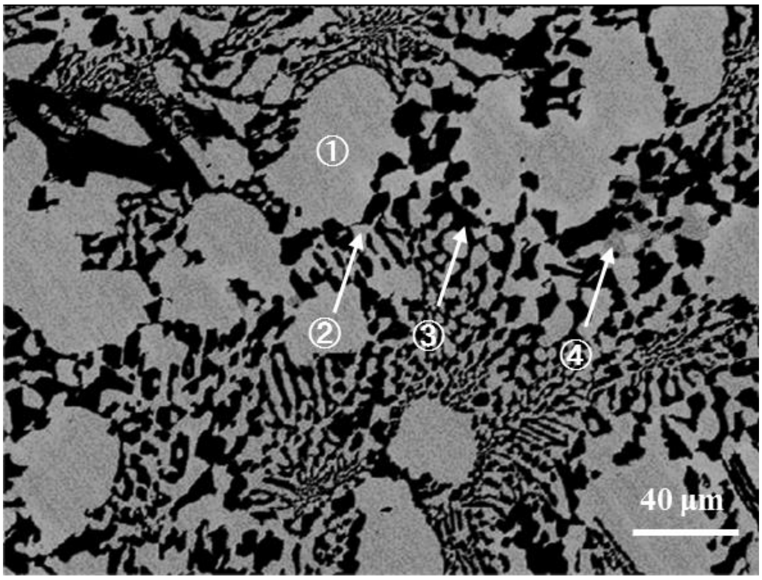

| Analysis area | Chemical compositions (mol%/mass%) | | | |
|---|---|---|---|---|
| | Ni | Cr | Si | P |
| ① | 58.3/63.2 | 34.2/32.8 | 6.6/3.5 | 0.9/0.5 |
| ② | 56.7/61.6 | 35.8/34.4 | 6.7/3.5 | 0.8/0.5 |
| ③ | 25.1/31.9 | 39.2/44.2 | 0.9/0.6 | 34.8/23.3 |
| ④ | 57.4/67.4 | 16.4/17.0 | 10.9/6.1 | 15.3/9.5 |

Table 2.3.3 Vickers hardness of phases in Ni-29Cr-6P-4Si filler metal.

| Phase | Vickers hardness (HV) |
|---|---|
| Coarse light gray phase | 238.7 |
| Fine light gray phase | 243.6 |
| Dark gray phase | 424.6 |

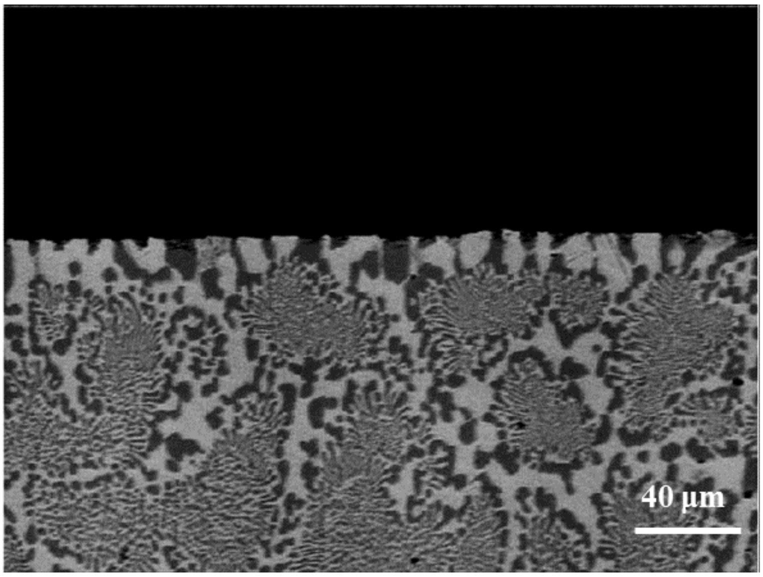

Fig. 2.3.5 Cross section morphology of Ni-29Cr-6P-4Si filler metal in electrochemical measurement shown in 2.2.5 (back-scattered electron image).

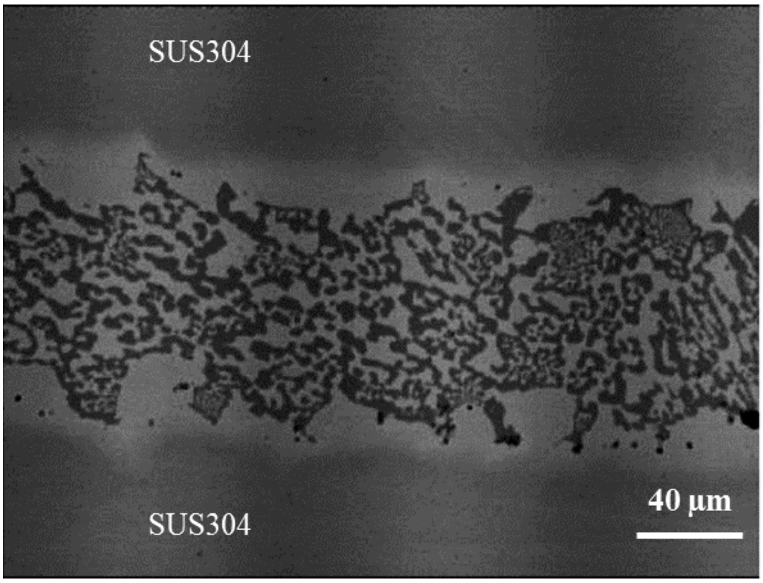

Fig. 2.3.6 Microstructure of SUS304 joints brazed with Ni-29Cr-6P-4Si filler metal in clearances of 100 μm (back-scattered electron image).

#### 2.3.3.2 Fe-20Cr-43Ni-10P filler metal

For Fe-20Cr-43Ni-10P, as shown in Fig. 2.3.4 (b), Fe and Ni are mainly segregated into the light gray phase, and P is almost enriched in the dark gray phase as well. Cr is much less in the light gray phase than in the dark gray phase. Table 2.3.4 and 2.3.5 show the chemical compositions and Vickers hardness of the phases in Fe-20Cr-43Ni-10P, respectively. The Fe: Cr: Ni: P ratio of the dark gray phase is 13.5: 38.0: 24.3: 24.2 (mass %), thus it is confirmed as a phosphide phase, and the phase has more than twice as high Vickers hardness as the light gray phase. The Fe: Cr: Ni: P ratio of the coarse bright gray phases is 40.2: 19.7: 39.0: 1.1 (mass %), and that of the fine bright gray phases is 37.7: 15.6: 45.6: 1.1 (mass %). The compositions of the coarse bright gray phase is different from that of the fine bright gray phase, and they are identified as solid-solution phases.

The Fe: Cr: Ni: P ratio of the phase marked with ④ in Table 2.3.4 is 21.3: 6.7: 59.7: 12.3 (mass%). Compared with the solid-solution phase in Fe-20Cr-43Ni-10P, the contents of Fe and Cr are low and the contents of Ni and P are high. Compared with the phosphide phase in Fe-20Cr-43Ni-10P, the contents of Fe and Ni are high and the contents of Cr and P are low. It is clear that the Cr content in the phase is lower than that in both the solid-solution phase and phosphide phase in Fe-20Cr-43Ni-10P. Furthermore, the phase is not found in the specimen for the electrochemical measurement shown in Fig. 2.3.14, in the brazing layer shown in Fig. 3.3.1 and in the fillet area shown in Fig. 4.3.15 (a). The three microstructures are also obtained after melting at the brazing temperature of 1373 K for 10 minutes (see 2.2.1) or 30 minutes (see 3.2.3 and 4.2.1). The phase also disappeared because of each element fully diffusing after the longer heating time. Hence, the phase is also confirmed an abnormal phase formed because of localized Cr deficiency during the ingot process.

Connecting with the DSC results shown in Fig. 2.3.2 (b), the weak exothermic peak (1321 K) corresponds to the formation of the abnormal phase, and there is not a corresponding endothermic peak in the heating curve because the abnormal phase is not a stable phase as well. Corresponding to the extinct exothermic peak at 1288 K, the coarse bright gray phase is confirmed as a primary crystal. Corresponding to the extinct exothermic peak at 1145 K, the fine bright gray phase and the dark gray phase are confirmed as a eutectic structure.

As indicated above, the composition of the coarse bright gray phase is different from the fine bright gray phase. Based on the DSC analysis results, the coarse bright gray phase solidified at 1288 K and the fine bright gray phase solidified at 1145 K. It is known that the solidifying temperature can make an effect on element segregation [25]. It is the more difference of the solidifying temperature that results in the composition difference of two kinds of the bright gray phases. In addition, the Cr content is higher than Fe and Ni in the phosphide phase because Cr is easier to be combined into a phosphide than Fe and Ni [26].

Table 2.3.4 Chemical compositions of phases in Fe-20Cr-43Ni-10P filler metal.

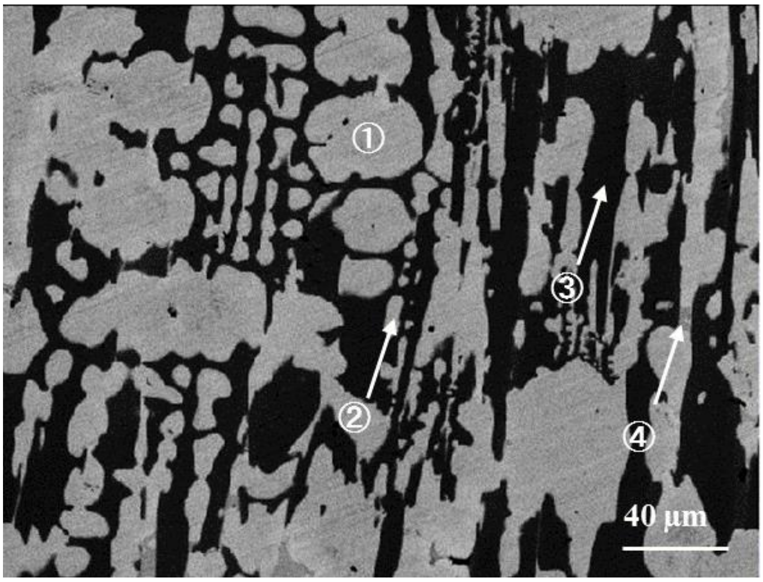

| Analysis area | Chemical compositions (mol %/mass%) | | | |
|---|---|---|---|---|
| | Fe | Cr | Ni | P |
| ① | 40.1/40.2 | 21.1/19.7 | 36.9/39.0 | 1.9/1.1 |
| ② | 37.8/37.7 | 16.7/15.6 | 43.6/45.6 | 1.9/1.1 |
| ③ | 11.2/13.5 | 33.7/38.0 | 19.1/24.3 | 36.0/24.2 |
| ④ | 19.8/21.3 | 6.6/6.7 | 52.8/59.7 | 20.8/12.3 |

Table 2.3.5 Vickers hardness of phases in Fe-20Cr-43Ni-10P filler metal.

| Phase | Vickers hardness (HV) |
|---|---|
| Coarse light gray phase | 273.4 |
| Fine light gray phase | 283.1 |
| Dark gray phase | 560.6 |

### 2.3.3.3 Fe-20Cr-20Ni-8P-5Si-2Mo filler metal

As shown in Fig. 2.3.4 (c), Fe-20Cr-20Ni-8P-5Si-2Mo is similar to Ni-29Cr-6P-4Si and Fe-20Cr-43Ni-10P in element distribution. Table 2.3.6 and 2.3.7 show the chemical compositions and Vickers hardness of the phases in Fe-20Cr-20Ni-8P-5Si-2Mo, respectively. The Fe: Cr: Ni: P: Si: Mo ratio of the dark gray phase is 27.4: 38.8: 8.5: 22.9: 0.9: 1.5 (mass%). The dark gray phase is identified as a phosphide phase, and Vickers hardness of the phase is up to 434.8 HV. The Fe: Cr: Ni: P: Si: Mo ratio of the fine bright gray phase is 60.5: 19.7: 13.8: 0.3: 5.4: 0.3 (mass%), and the Fe: Cr: Ni: P: Si: Mo ratio of the coarse bright gray phase is 58.7: 19.7: 16.7: 0.4: 4.3: 0.2 (mass%). The chemical compositions of the fine bright gray phase are almost same as that of the fine bright gray phase. Both coarse bright gray phase and fine bright gray phase are Fe-based solid-solution phases.

The Fe: Cr: Ni: P: Si: Mo ratio of the phase marked with ④ in Table 2.3.6 is 15.0: 49.7: 24.2: 1.7: 5.8: 3.6 (mass%). The phase has almost the same contents of Si and P as the solid-solution phase in Fe-20Cr-20Ni-8P-5Si-2Mo. However, the Cr content is almost twice as much as that of the solid-solution phase in Fe-20Cr-20Ni-8P-5Si-2Mo. As same as Ni-29Cr-6P-4Si and Fe-20Cr-43Ni-10P, the phase is not found in the specimen for the electrochemical measurement shown in Fig. 2.3.16, in the brazing layer shown in Fig. 3.3.3 and in the fillet area shown in Fig. 4.3.16 (a). The three microstructures were also obtained after melting at the brazing temperature of 1373 K for 10 minutes (see 2.2.1) or 30 minutes (see 3.2.3 and 4.2.1). The phase also disappeared because of each element fully diffusing after the longer heating time. Hence, the phase is also confirmed an abnormal phase formed because of localized Cr enrichment during the ingot process.

By terms of the DSC results shown in Fig. 2.3.2 (c), different from Ni-29Cr-6P-4Si and Fe-20Cr-43Ni-10P, both the weak exothermic peak and the corresponding endothermic peak are not found in the DSC curves. It is implied that the number of the abnormal phase is very small. According to the DSC results, the coarse bright gray phase is a primary crystal solidifying at 1331 K, the fine bright gray phase and the dark gray phase are a eutectic phase solidifying at 1322 K. The bright gray phases in the primary crystal and eutectic phase are almost same compositions in the principal components of Fe, Cr and Ni. This benefits very close solidifying temperatures.

Table 2.3.6 Chemical compositions of phases in Fe-20Cr-20Ni-8P-5Si-2Mo filler metal.

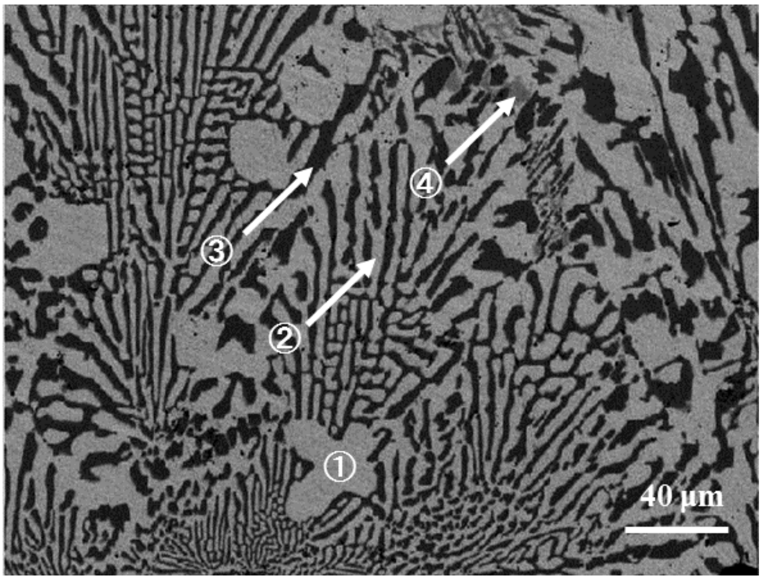

| Analysis area | Chemical compositions (mol %/mass%) | | | | | |
|---|---|---|---|---|---|---|
| | Fe | Cr | Ni | P | Si | Mo |
| ① | 55.8/58.7 | 20.0/19.7 | 15.2/16.7 | 0.7/0.4 | 8.2/4.3 | 0.1/0.2 |
| ② | 56.9/60.5 | 19.9/19.7 | 12.4/13.8 | 0.5/0.3 | 10.2/5.4 | 0.1/0.3 |
| ③ | 22.6/27.4 | 34.5/38.8 | 6.7/8.5 | 34.0/22.9 | 1.5/0.9 | 0.7/1.5 |
| ④ | 13.9/15.0 | 49.5/49.7 | 21.3/24.2 | 2.7/1.7 | 10.7/5.8 | 1.9/3.6 |

Table 2.3.7 Vickers hardness of phases in Fe-20Cr-20Ni-8P-5Si-2Mo filler metal.

| Phase | Vickers hardness (HV) |
|---|---|
| Coarse light gray phase | 256.3 |
| Fine light gray phase | 264.1 |
| Dark gray phase | 434.8 |

### 2.3.4 Electrochemical characteristics

Anodic and cathodic polarization curves are shown in Fig. 2.3.7. All the brazing filler metals exhibit active-passive transitions distinctly in terms of the anodic polarization behaviors. Nevertheless, the specific potential ranges of these transitions are different from one another. The Fe-Cr-based brazing filler metals display extremely narrow passive regions, compared with Ni-29Cr-6P-4Si. In contrast, SUS304 stainless steel does not nearly present an obvious active region, and the critical current ($i_{crit}$) required for passivation is extremely close to the passivation current ($i_{pass}$). Moreover, a wide range passive region (potential: -0.1- 0.5 V-SSE) is shown. Self-passivation characteristic is particularly apparent. It will be investigated in chapter 4.

To obtain a quantitative understanding of the anodic reaction, electrochemical parameters such as corrosion potential ($E_{corr}$), corrosion current density ($i_{corr}$), Tafel anodic slope ($\beta_a$) and Tafel cathodic slope ($\beta_c$) were estimated by Tafel extrapolation. Tafel's law is one of the major

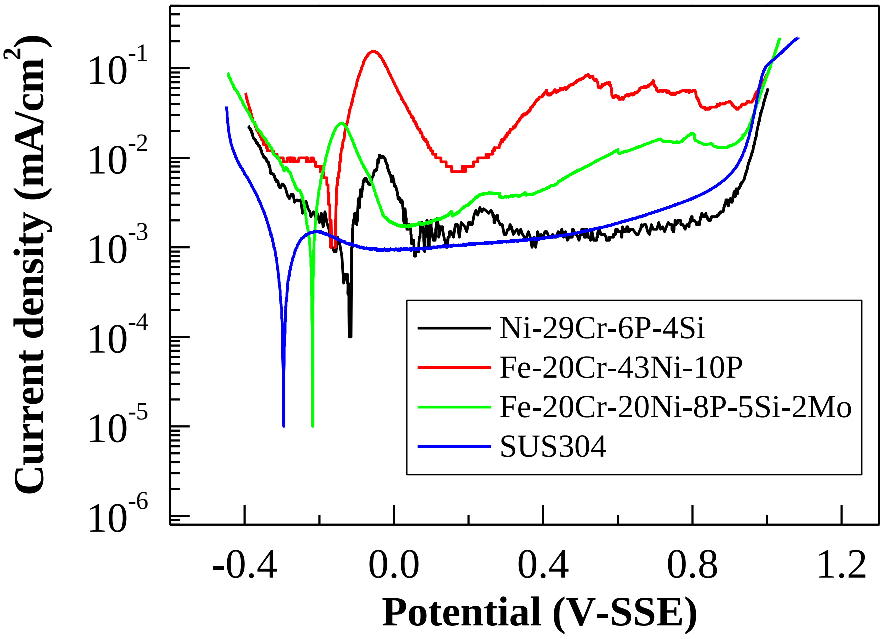

Fig. 2.3.7 Potentiodynamic polarization curves.

laws in electrochemistry. According to the Tafel's law, logarithm of the current density in an electrochemical reaction varies linearly with the electrode potential (at potentials removed from the open-circuit rest potential). In other words, the Tafel's law can be expressed with Eq. (2.3.1),

$$E = a+b \ln i \qquad (2.3.1)$$

where $a$ and $b$ are constants, $E$ and $i$ are electrode potential and the current density respectively. Moreover, when $E = E_{\mathrm{corr}}$, then $i = i_{\mathrm{corr}}$. This is the basis for the Tafel extrapolation [27].

The Tafel region of the polarization curve is fitted with linear fitting of Origin 6.1 in this study. The results of the Tafel extrapolation are shown in Fig. 2.3.8. The fitting lines are shown in red and the linear fitting equations are presented in Table 2.3.8. In addition, polarization resistance ($R_{\mathrm{p}}$) was calculated by Eq. (2.3.2) [28]. The results are summarized in Table 2.3.9.

$$R_{\mathrm{p}} = \beta_{\mathrm{a}}\beta_{\mathrm{c}}/[2.3\ i_{\mathrm{corr}}\ (\beta_{\mathrm{a}}+\beta_{\mathrm{c}})] \qquad (2.3.2)$$

Table 2.3.8 Linear fitting equations of Tafel region.

| Brazing filler metal | Linear fitting equations | |
|---|---|---|
| | Anode | Cathode |
| Fe-20Cr-43Ni-10P | $y = -0.03314+0.02477x$ | $y = -1.497-0.2664x$ |
| Fe-20Cr-20Ni-8P-5Si-2Mo | $y = -0.06541+0.02513x$ | $y = -0.6163-0.06616x$ |
| Ni-29Cr-6P-4Si | $y = 0.04934+0.02496x$ | $y = -0.7511-0.08716x$ |

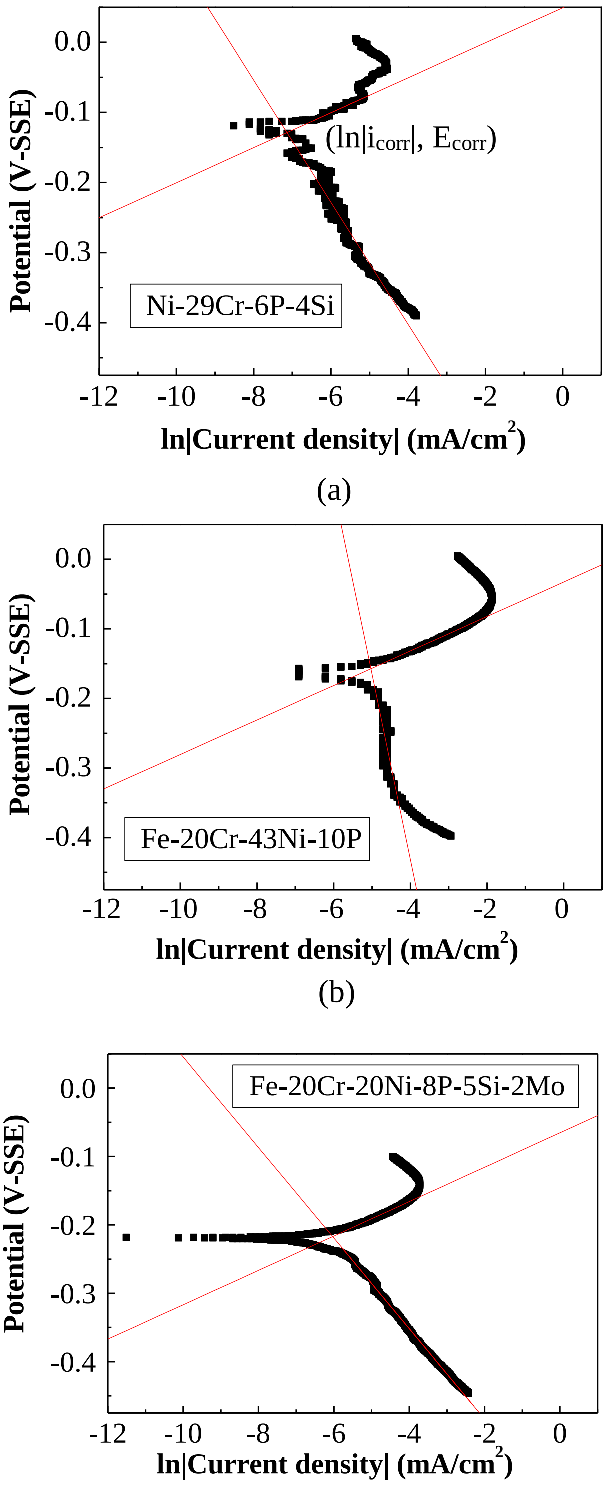

(a)

(b)

(c)

Fig. 2.3.8 Liner fitting of Tafel region of the polarization curves.

(a) Ni-29Cr-6P-4Si, (b) Fe-20Cr-43Ni-10P, (c) Fe-20Cr-20Ni-8P-5Si-2Mo.

Table 2.3.9 Electrochemical parameters obtained by Tafel extrapolation.

| Brazing filler metal | $E_{corr}$ (V) | $i_{corr}$ ( A/cm$^2$) | $\beta_a$ ( V/A) | $\beta_c$ ( V/A) | $R_p$ ($\Omega$cm$^2$) |
|---|---|---|---|---|---|
| Fe-20Cr-43Ni-10P | -0.16 | $6.55\times10^{-6}$ | 24.77 | 266.35 | $1.51\times10^{3}$ |
| Fe-20Cr-20Ni-8P-5Si-2Mo | -0.22 | $2.40\times10^{-6}$ | 25.13 | 66.16 | $3.30\times10^{3}$ |
| Ni-29Cr-6P-4Si | -0.13 | $7.93\times10^{-7}$ | 24.96 | 87.16 | $1.06\times10^{4}$ |

$E_{corr}$ represents how difficult materials are corroded [29]. The nobler $E_{corr}$ is, the more difficultly the material is subjected to corrosion attack. $E_{corr}$ is the most negative for Fe-20Cr-20Ni-8P-5Si-2Mo, followed by Fe-20Cr-43Ni-10P and Ni-29Cr-6P-4Si, respectively. It means that Fe-20Cr-20Ni-8P-5Si-2Mo is easiest and Ni-29Cr-6P-4Si is the most difficult to be corroded. The difference of $E_{corr}$ is connected with the Ni content because Ni processes nobler potential than Fe [30]. It is implied that the proportion of Ni and Fe is critical in order to obtain suitable $E_{corr}$ for Fe-Cr brazing filler metals.

$i_{corr}$ expresses corrosion rate [28]. Corrosion attack will evolve at a high speed when $i_{corr}$ increases. Some guidelines have been developed to establish a relationship between the corrosion current density and corrosion rate, as shown in Table 2.3.10 [31]. $i_{corr}$ is the highest for Fe-20Cr-43Ni-10P and the lowest for Ni-29Cr-6P-4Si. According to Table 2.3.10, Fe-20Cr-43Ni-10P and Fe-20Cr-20Ni-8P-5Si-2Mo have high corrosion rate while Ni-29Cr-6P-4Si has a moderate corrosion rate.

$R_p$ suggests the charges transfer across the metal/electrolyte interface, and it is utilized to evaluate corrosion resistance [31]. The greater $R_p$ is, the more difficult the charges transfer, and consequently the great corrosion resistance is presented. $R_p$ of the specimens can be ranked in the following order: Ni-29Cr-6P-4Si>Fe-20Cr-20Ni-8P-5Si-2Mo>Fe-20Cr-43Ni-10P.

Corrosion rate and corrosion resistance for Fe-20Cr-43Ni-10P and Fe-20Cr-20Ni-8P-5Si-2Mo are discussed in 2.3.5.2.

Table 2.3.10 Relationship between corrosion current density and corrosion rate.

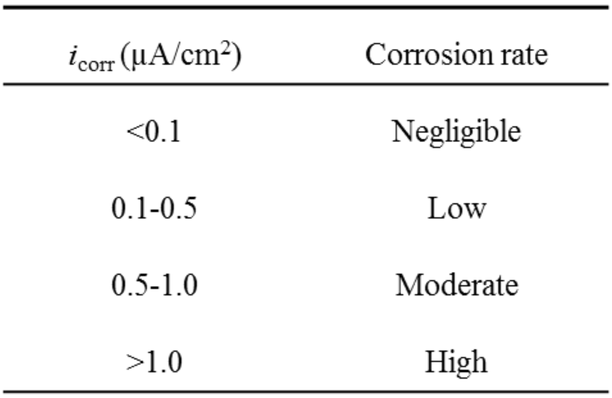

| $i_{corr}$ (μA/cm$^2$) | Corrosion rate |
|---|---|
| <0.1 | Negligible |
| 0.1-0.5 | Low |
| 0.5-1.0 | Moderate |
| >1.0 | High |

### 2.3.5 Corrosion behaviors

#### 2.3.5.1 Anode and cathode in electrode reaction

Fig. 2.3.9 and Fig. 2.3.10 show the surface morphologies after the constant potential polarization for 3 h, 10 h, 50 h and 100 h for Fe-20Cr-43Ni-10P and Fe-20Cr-20Ni-8P-5Si-2Mo, respectively. At the polarization time of 3 h, it is obvious that the bright gray solid-solution phases are preferentially dissolved for both brazing filler metals. It is confirmed that the solid-solution phases are the anodes in both brazing filler metals.

Compared with the surface morphologies, the surface greatly changed for 100 h. In order to determine the survival phases, mapping analysis for the surfaces were conducted and the results are shown in Fig. 2.3.11. P detection reveals that the phosphide phases avoid the corrosion and become the cathodes in both brazing filler metals because P exists almost only in the phosphide phase.

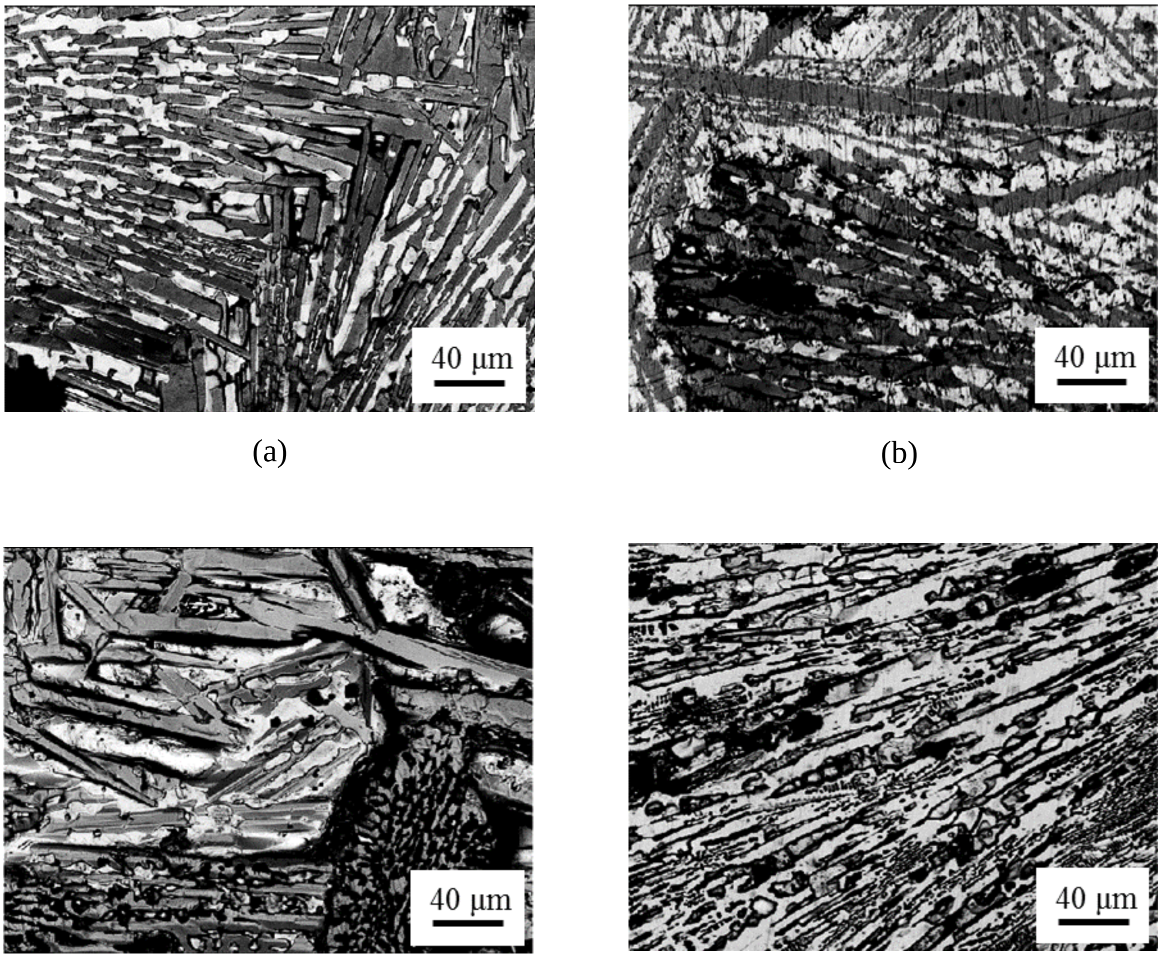

(a) (b)

(c) (d)

Fig. 2.3.9 Surface microstructures of Fe-20Cr-43Ni-10P brazing filler metal after constant potential polarization at potential of -0.11 V-SSE (back-scattered electron images).
(a) polarized for 3 h, (b) polarized for 10 h, (c) polarized for 50 h, (d) polarized for 100 h.

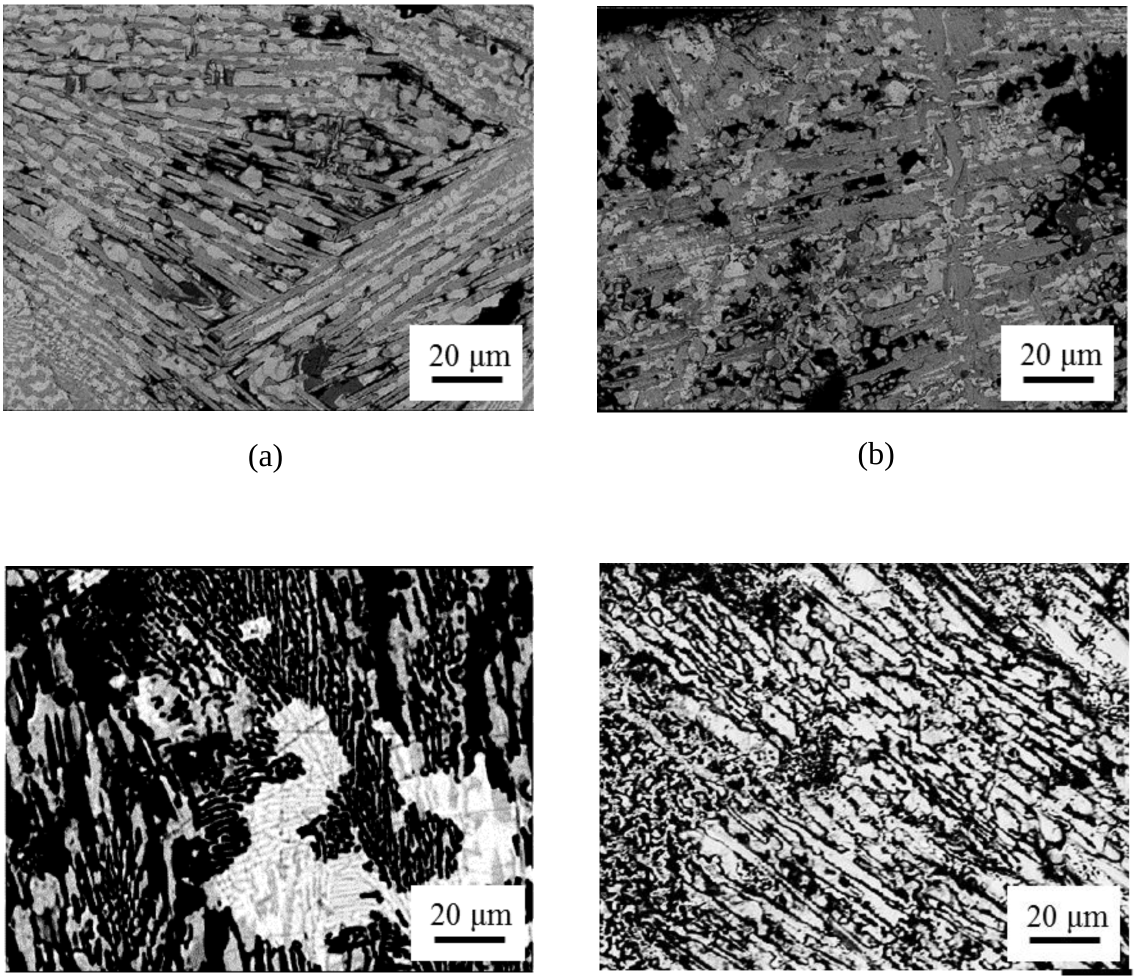

(a) (b)

(c) (d)

Fig. 2.3.10 Surface microstructures of Fe-20Cr-20Ni-8P-5Si-2Mo brazing filler metal after constant potential polarization at potential of -0.17 V-SSE (back-scattered electron images). (a) polarized for 3 h, (b) polarized for 10 h, (c) polarized for 50 h, (d) polarized for 100 h.

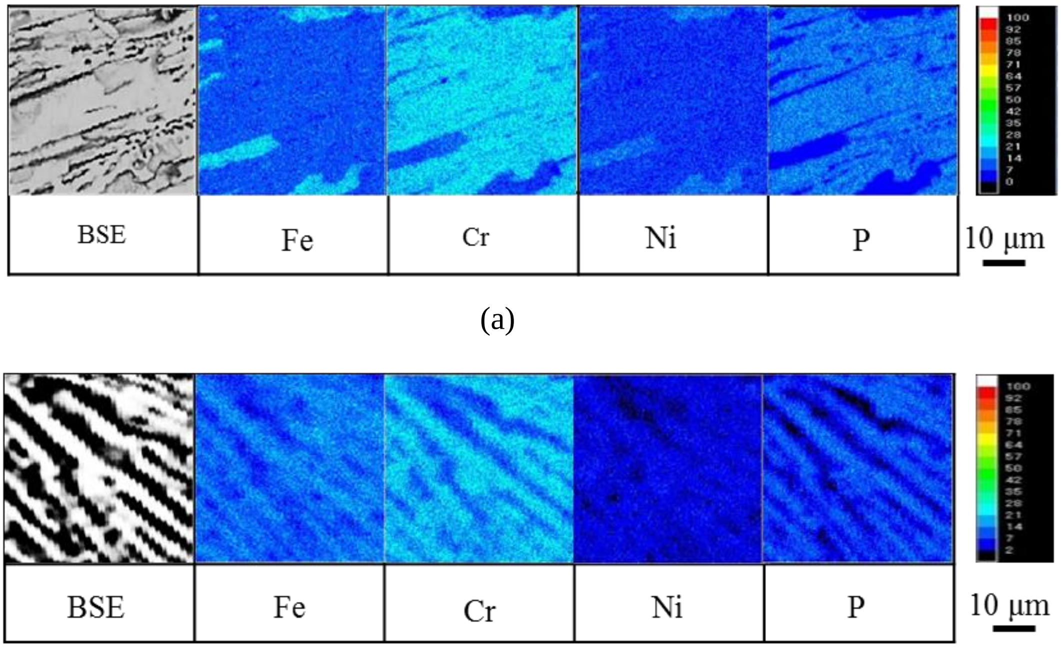

(a)

(b)

Fig. 2.3.11 Mapping analysis results for surfaces of brazing filler metals after constant potential polarization for 100 h.

(a) Fe-20Cr-43Ni-10P, potential: -0.11 V-SSE,

(b) Fe-20Cr-20Ni-8P-5Si-2Mo, potential: -0.17 V-SSE.

2.3.5.2 Corrosion mechanism

In order to further understand the anti-corrosion mechanism, the corrosion processes are studied by the results of the constant potential polarization tests. The change in current density as a function of polarization time can be used to monitor the chemical stability and corrosion process. Fig. 2.3.12 shows the current vs. time relationship. Polarization potential is -0.11 V-SSE for Fe-20Cr-43Ni-10P and -0.17 V-SSE for Fe-20Cr-20Ni-8P-5Si-2Mo. As shown in Fig. 2.3.7, the polarization potentials lie in the active area, accordingly the results can represent corrosion process for the brazing filler metals.

For Fe-20Cr-43Ni-10P, the corrosion process can be divided into three different stages during about 100 h, these being in the 0-6 h, 6-56 h, and 56-110 h time periods, respectively. Fig. 2.3.13 presents field emission scanning electron microscopy (FE-SEM) images for every stage. In the initial stage (0-6 h), current density rapidly varied from 0.017 mA/cm$^2$ to the peak of 0.026 mA/cm$^2$ and then declined to the nadir of 0.009 mA/cm$^2$. Fig. 2.3.13 (a) displays the FE-SEM image at this stage. Several brighter areas are observed on the bright matrix. Brighter color

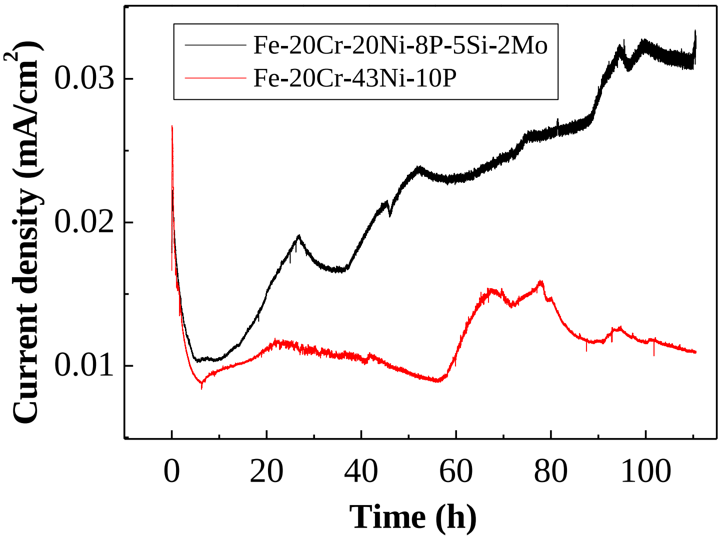

Fig. 2.3.12 Current density dependence on time during constant potential tests (potential: -0.11 V-SSE for Fe-20Cr-43Ni-10P,
potential: -0.17 V-SSE for Fe-20Cr-20Ni-8P-5Si-2Mo).

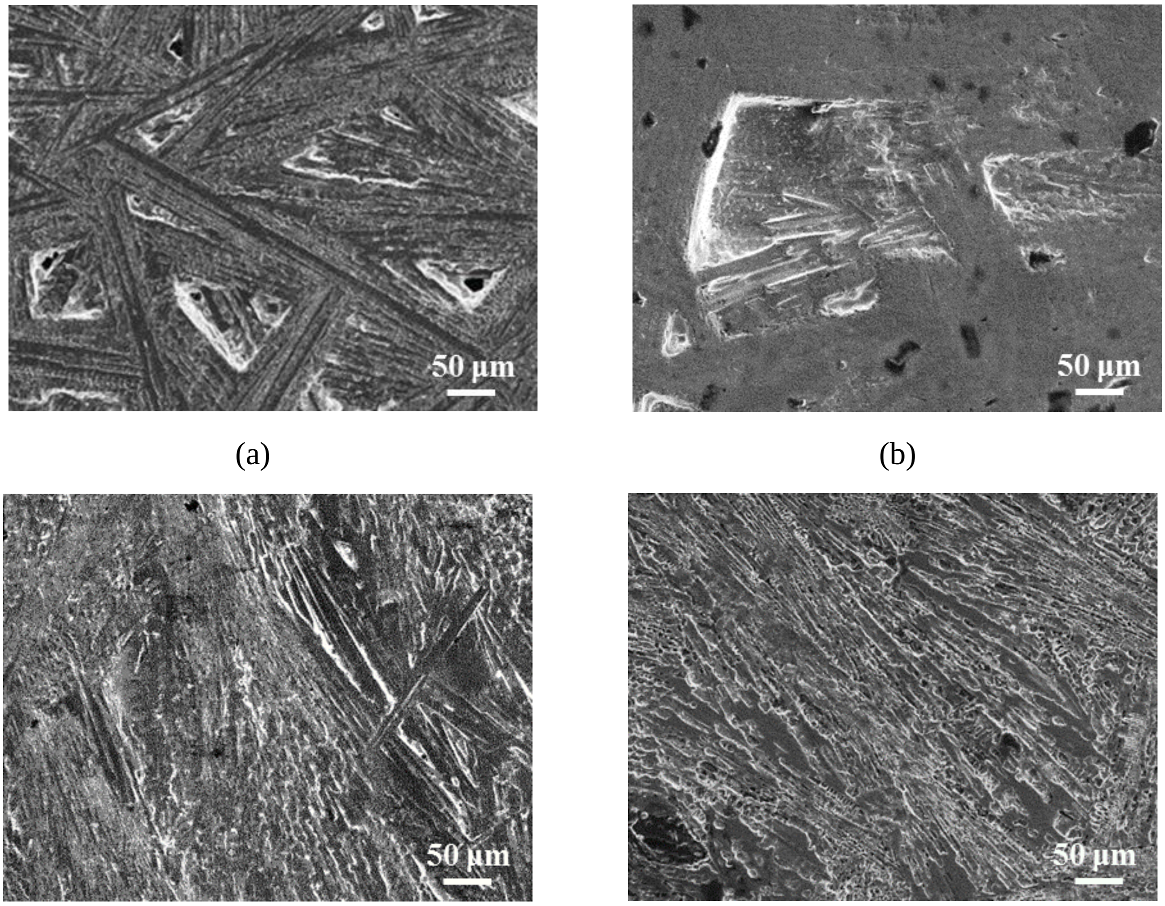

(a) (b) (c) (d)

Fig. 2.3.13 Surface morphologies of Fe-20Cr-43Ni-10P after constant potential polarization test at potential of -0.11 V-SSE for (a) 3 h, (b) 10 h, (c) 50 h, (d) 100 h.

implies that the localized electro dissolution surpasses the whole surface dissolution (the bright matrix). The brighter areas can been interpreted as dissolution of metal at surface defects [32]. At the first stage, corrosion process can been explained as follows. Onset of corrosion occurs at surface defects (such as void and inclusions). Current density rapidly increases with more defect pits activated, at the same time the areas around the defect pits have been driven so that corrosion tends to spread around. Current density reaches the peak and began to decline till the surface turns into a temporary steady state.

In the second stage (6-56 h), the current density displays fluctuation within a narrow range.

This reflects the heterogeneous reactions. Fig. 2.3.13 (b) and (c) show FE-SEM images at this stage. The stage can be described that corrosion tends to occur all over the surface with remaining localized electro dissolution continuing to spread out. Heterogeneous reactions in this stage are connected with surface morphologies confirmed by Fig. 2.3.9 (c).

From 56 to 100 h, the current density distinctly increases. As known, the current density is inversely proportional to the real soluble area in the logarithmic coordinate [33]. Increase of the current density reflects decrease of the real soluble area. This means that great changes have taken place on the surface, for instance, pit corrosion or formation of a cavity, and so on. However these cannot been verified according to Fig. 2.3.9 (d) and Fig. 2.3.13 (d). It is implied that the corrosion reactions do not only proceed on the surface but also permeate in the depth direction. Fig. 2.3.14 shows cross sectional morphologies for 3 h, 10 h, 50 h and 100 h. It is not observed that corrosion develops in the depth direction for 50 h, however, corrosion extends in the depth direction for 100 h. In addition, corrosion in depth direction is uniform and the cathode phase has been almost completely preserved. It is known that current density is directly proportional to the area ratio of the cathode to the anode for the galvanic corrosion [34]. The preserved cathode phase increases the area of the cathode resulting in the increase of current density. Moreover, increase of the current density will accelerate the corrosion. In summary, three corrosion development stages can be identified: initiation, uniform galvanic corrosion on the entire surface, accelerated corrosion in depth direction for Fe-20Cr-43Ni-10P.

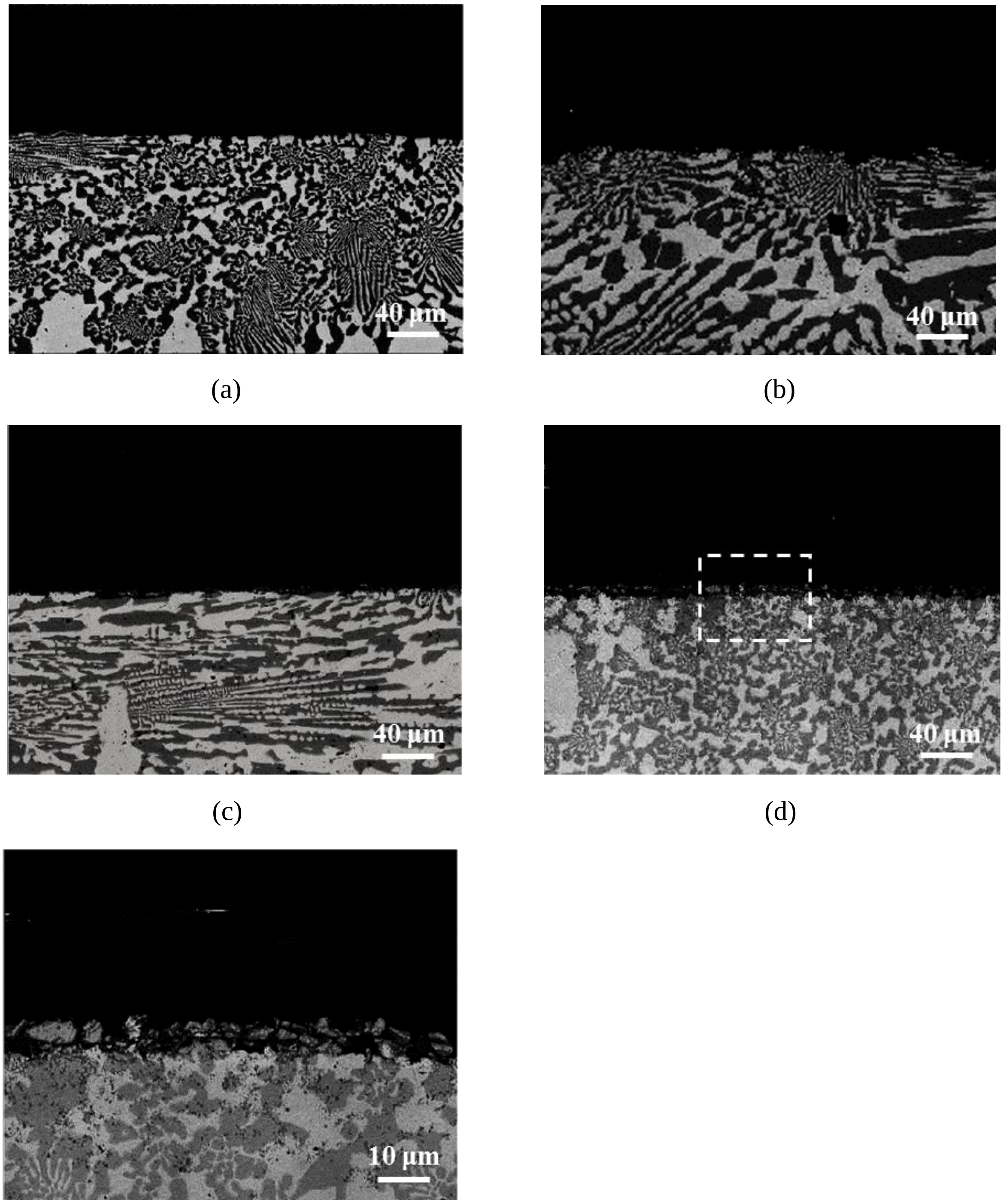

(a) (b) (c) (d) (e)

Fig. 2.3.14 Cross sectional morphologies of Fe-20Cr-43Ni-10P after constant potential polarization test at potential of -0.11 V-SSE for (a) 3 h, (b) 10 h. (c) 50 h, (d) 100 h, (e) magnified image of dotted area shown in (d).

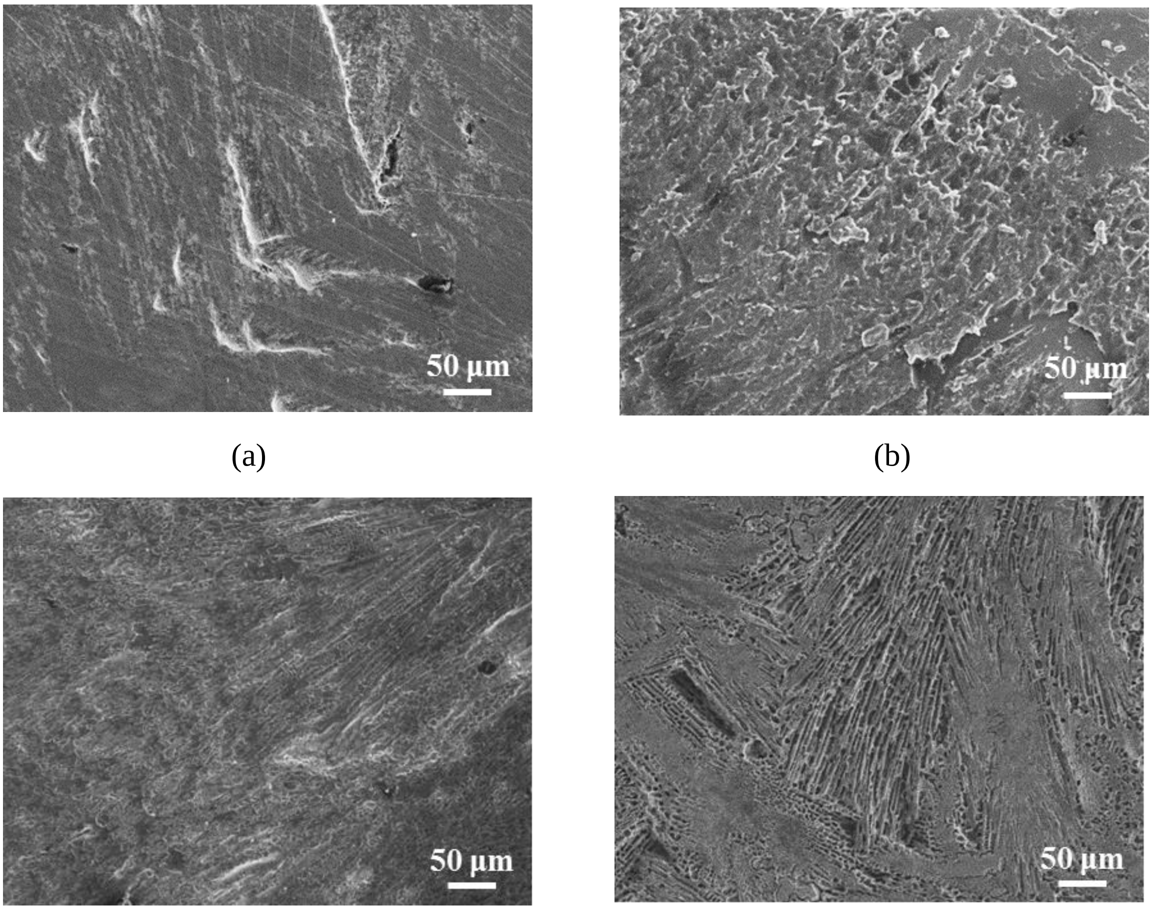

(a) (b)

(c) (d)

Fig. 2.3.15 Surface morphologies of Fe-20Cr-20Ni-8P-5Si-2Mo after constant potential polarization test at potential of -0.17 V-SSE for (a) 3 h, (b) 10 h, (c) 50 h, (d) 100 h.

In the case of Fe-20Cr-20Ni-8P-5Si-2Mo, the corrosion process is made up of three different stages as well, these being in the 0-5 h, 5-11 h, and 11-100 h time periods, respectively. Surface images with FE-SEM are presented in Fig. 2.3.15. The corrosion process is similar with Fe-20Cr-43Ni-10P for the first 11 hours. In the onset stage (0-5 h), current density varied rapidly from 0.019 mA/cm$^2$ to the peak of 0.022 mA/cm$^2$ and then declined to the nadir of 0.010 mA/cm$^2$. It is as well explained that corrosion occurs at surface defects and spreads out on the surface. However, the second stage (5-11h) continues for only 6 h. It is reflected that the surface of Fe-20Cr-20Ni-8P-5Si-2Mo is extremely unstable. This is connected with the more negative $E_{\mathrm{corr}}$. As for the third stage, the current density is sharply ascending and displays typical characteristics of the located corrosion [35]. As shown in Fig. 2.3.10 (c), Fig. 2.3.10 (d) and

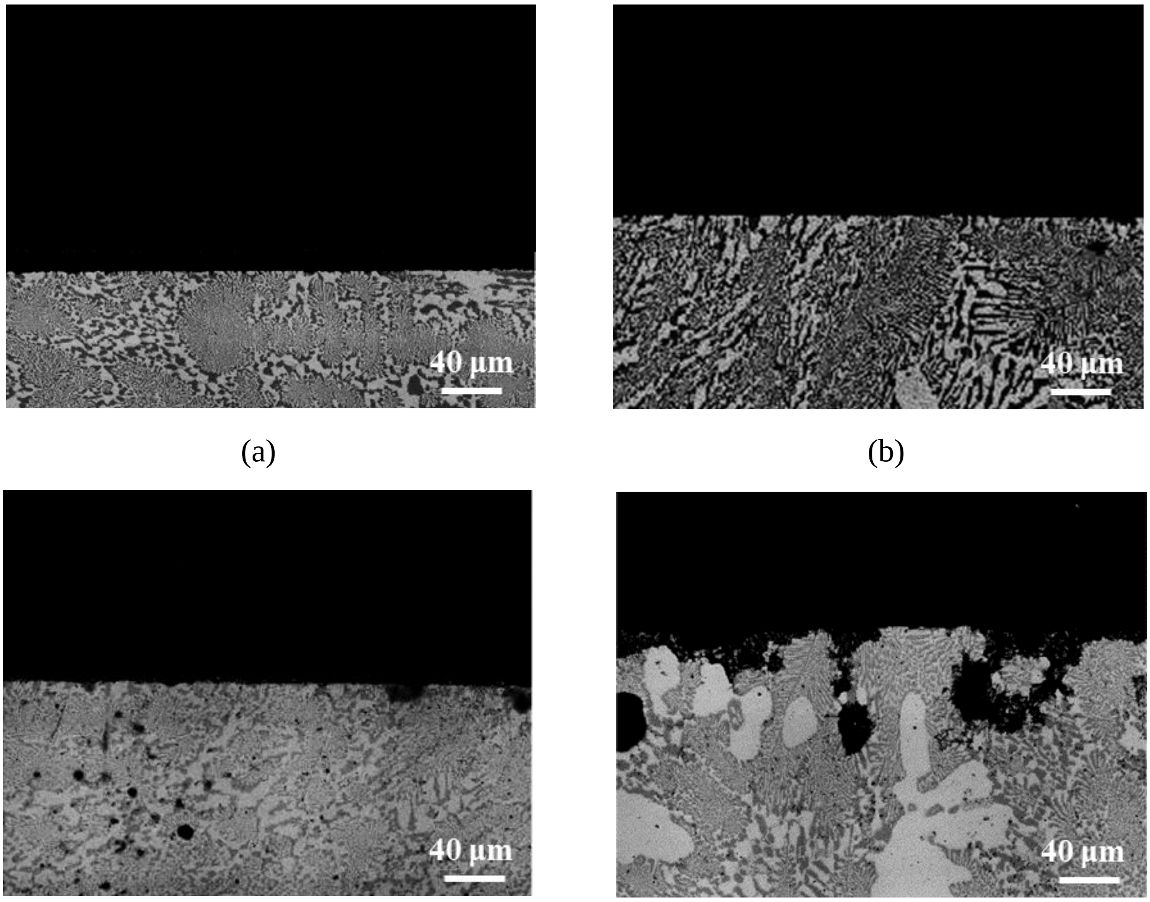

(a) (b)

(c) (d)

Fig. 2.3.16 Cross section morphologies of Fe-20Cr-20Ni-8P-5Si-2Mo after constant potential polarization test at potential of -0.17 V-SSE for (a) 3 h, (b) 10 h. (c) 50 h, (d) 100 h.

Fig. 2.3.15 (d), corrosion reactions do really occur on the localized areas of the surface. Furthermore, as shown in Fig. 2.3.15 (d), it is found that there are some black pits on the surface for 100 h. Nevertheless, it is not determined that these pits are cavities from the located corrosion or the surface defects shown in Fig. 2.3.15 (a), and it is not demonstrated whether or not corrosion reactions may spread all over the surface with time. Fig. 2.3.16 shows cross sectional morphologies for 3 h, 10 h, 50 h and 100 h. As shown in Fig. 2.3.16 (c) and (d), it is observed that corrosion developed in the depth direction at the third stage. Furthermore, corrosion in the depth direction is non uniform and corrosion depth explodes more quickly at some local area than that on the whole surface. It is confirmed that these pits shown in Fig.

2.3.15 (d) are the cavities from the located corrosion, and it can be forecasted that these cavities make corrosion proceed as autocatalysis agents [36]. In summary, three stages are identified in the development of corrosion of Fe-20Cr-20Ni-8P-5Si-2Mo: initiation, galvanic corrosion on the surface, and the formation of the cavities on the surface.

Due to the formation of the phosphide phase, the localized corrosion is presented for the two Fe-Cr-based brazing filler metals. For Fe-20Cr-43Ni-10P, corrosion proceeds in the form of uniform galvanic corrosion on the entire surface. Different from Fe-20Cr-43Ni-10P, for Fe-20Cr-20Ni-8P-5Si-2Mo, corrosion in the depth direction explodes more quickly at some local areas than that on the whole surface, resulting in the occurrence of the cavities. Fe-20Cr-20Ni-8P-5Si-2Mo is corroded along these cavities at some local areas of the surface.

Note that it has been assumed that the corrosion area corresponds to the whole surface exposed to the solution for the data shown in Table 2.3.9. In other words, a general corrosion has been assumed. In the case of the localized corrosion, the corrosion area is smaller than what is assumed, and then the actual corrosion current density will be greater than what is calculated. As a consequence, $i_{\mathrm{corr}}$ and $R_{\mathrm{p}}$ cannot be utilized to evaluate corrosion rate and corrosion resistance respectively for Fe-Cr brazing filler metals.

Although electrochemical parameters shown in Table 2.3.9 cannot quantitatively evaluate corrosion rate and corrosion resistance for the localized corrosion, the datas provide important information for qualitative understanding of electrochemical characteristics. As shown in Table 2.3.9, the two Fe-Cr-based brazing filler metals are close to Ni-29Cr-6P-4Si in terms of $\beta_{\mathrm{a}}$. In contrast, $\beta_{\mathrm{c}}$ is distinctly different for the two alloys compared to that of Ni-29Cr-6P-4Si, especially for Fe-20Cr-43Ni-10P. It should be concerted how the cathode impacts on corrosion behavior. Specifically, it will contribute to improvement of corrosion resistance to figure out the effect of the P content on the electrochemical characteristic for the Fe-Cr-based brazing filler metal.

## 2.4 Conclusions

Two kinds of Fe-Cr-based brazing filler metals, Fe-20Cr-43Ni-10P and Fe-20Cr-20Ni-8P-5Si-2Mo, have been developed as substitutes for expensive Ni-based brazing filler metals in brazing the EGR cooler. Microstructures and electrochemical corrosion behaviors of the alloys were extensively evaluated in this chapter. Important conclusions are summarized below:

1) For Fe-20Cr-43Ni-10P and Fe-20Cr-20Ni-8P-5Si-2Mo, the microstructures are composed of a solid-solution primary crystal and a eutectic phase, and the eutectic phase is made up of a solid-solution phase and phosphide phase. Vickers hardness of the phosphide phase is up to 560.6 and 434.8 HV in Fe-20Cr-43Ni-10P and Fe-20Cr-20Ni-8P-5Si-2Mo, respectively.

2) Fe-20Cr-43Ni-10P reveals the galvanic corrosion and Fe-20Cr-20Ni-8P-5Si-2Mo is attacked at a few localized areas so that the cavities form on the surface. The solid-solution phase becomes the anode and phosphide phase served as the cathode during the corrosion reaction in both brazing filler metals. The solid-solution phases are corroded and phosphide phases survive.

3) Corrosion potentials were -0.16 V-SSE and -0.22 V-SSE in the experimental compound solution for Fe-20Cr-43Ni-10P and Fe-20Cr-20Ni-8P-5Si-2Mo, respectively. Fe-20Cr-43Ni-10P is difficultly corroded almost as same as Ni-29Cr-6P-4Si. However, Fe-20Cr-20Ni-8P-5Si-2Mo is more easily corroded than Ni-29Cr-6P-4Si.

4) Corrosion rate and corrosion resistance cannot be evaluated by the corrosion current density and polarization resistance, respectively for the two Fe-Cr-based brazing filler metals because of the localized corrosion. Nevertheless, the difference of $\beta_c$ with Ni-29Cr-6P-4Si implies that corrosion rate and corrosion resistance are affected by the P content for Fe-Cr-based brazing filler metals.

References

[1] M. Weinstein, L. Lee, L. Johnson, A. Battenbough and A.M. Osmanda: Technical Paper in Wallcolmonoy, July 2012.

[2] T. Watanabe, K. Wakatsuki, A. Yanagisawa and T. Sasaki: Quarterly Journal of the Japan Welding Society, **29** (2011) 241-247.

[3] X.W. Wu, R.S. Chandel, H.P. Seow and H. Li: Journal of Materials Processing Technology, **113** (2001) 215-221.

[4] Y.N. Lia, M.I. Osendi and P. Miranzo: Journal of the American Ceramic Society, **86** (2003) 1226-1229.

[5] G. Dehm, B. Medres, L. Shepeleva, C. Scheu, M. Bamberger, B.L. Mordike, S. Mordike, G. Ryk, G. Halperin and I. Etsion: Wear, **18** (1999) 225-229.

[6] C.Y. Su, C.P. Chou, W.J. Chang and M.H. Liu: Journal of Materials Engineering and Performance, **9** (2000) 663-668.

[7] I.W. Donald and H.A. Davies: Journal of Materials Science, **15** (1980) 2754-2760.

[8] F. Fernandes, B. Lopes, A. Cavaleiro, A. Ramalho and A. Loureiro: Surface and Coatings Technology, **205** (2011) 4094-4106.

[9] G.Q. Xie, D.V. L. Luzgina, H. Kimura and A. Inoue: Intermetallics, **18** (2010) 851-858.

[10] W.S. Chen and R.K. Shiue: ISIJ International, **52** (2012) 939-941.

[11] R.K. Roya, A.K. Panda, S.K. Das, Govind and A. Mitra: Materials Science and Engineering A, **523** (2009) 312-315.

[12] N. Wu, Y.J. Li, J. Wang and U.A. Puchkov: Journal of Materials Processing Technology, **212** (2012) 794-800.

[13] Y. Hisamori: Quarterly Journal of the Japan Welding Society, **10** (1992) 211-216.

[14] C.L. Ou, D.W. Liaw, Y.C. Du and R.K. Shiue: Journal of Materials Science, **41** (2006) 6353-6361.

[15] T. Hartmann and D. Nuetzel: Proceedings of the 4th International Brazing & Soldering Conference, (2009) 110-117.

[16] V.A. Şerban, C. Codrean, D. Utu and C. Stoian: Proceeding of the 6th WSEAS International Conference on Energy, Environment, Ecosystems and Sustainable Development, (2010) 176-181.

[17] X.W. Wu, R.S. Chandela, H. Li, H.P. Seowa and S.C. Wu: Journal of Materials Processing Technology, **104** (2000) 34-43.

[18] T. Onzawa and K. Sasabe: Journal of the Japan Welding Society, **69** (2000) 45-53.

[19] G. Stratford, A. Battenbouch, L. Lee and M. Weinstein: Welding Journal, **3** (2011) 54-59.

[20] T. Watanabe, K. Wakatsuki, A. Yanagisawa and T. Sasaki: Quarterly Journal of the Japan Welding Society, **29** (2011) 241-247.

[21] T. Fujita, T. Yamada and N. Takahashi: Tetsu to Hagane, **61** (1975) 357-370.

[22] K. Hosomi, H. Morimoto and Y. Ashida: Tetsu to Hagane, **74** (1988) 2025-2032.

[23] T. Nakazawa, S. Date, M. Tendo and M. Yamazaki: Tetsu to Hagane, **91** (2005) 670-675.

[24] T. Hartmann and D. Nuetzel: Proceedings of the 5th International Brazing and Soldering Conference, (2012) 394-400.

[25] A. Heckl, R. Rettig and R.F. Singer: Metallurgical and Materials Transactions, **41**A (2010) 202-211.

[26] H. Kaneko, T. Nishizawa and K. Tamaki: Journal of the Japan Institute of Metals and Materials, **29** (1965) 159-165.

[27] E. McCafferty: Corrosion Science, **47** (2005) 3202-3215.

[28] K. Sugimoto: Kinzokuhusyokukougaku, Uchidarokakuho, (2009) 74.

[29] Y.Y. Chen, U.T. Hong, H.C. Shih, J.W. Yeh and T. Duval: Corrosion Science, **47** (2005) 2679-2699.

[30] H.H. Uhlig, M. Seigo (translator) and M. Iwao (translator): Corrosion Reaction and Control (second ed.), Sangyo Tosyo, (1974) 339.

[31] M. Mancio1, C. Carlos, J.Y. Zhang, J.T. Harvey, P.J.M. Monteiro and A. Ali: Journal of Material in Civil Engineering, **10** (2008) 650-657.

[32] C. Punckt, M. Bolscher, H.H. Rotermund, A.S. Mikhailov, L. Organ, N. Budiansky, J.R. Scully and J.L. Hudson: Science, **305** (2004) 1131-1136.

[33] Y. Gan, Y. Li and H.C. Lin: Corrosion Science, **43** (2001) 397-411.

[34] L. Kruger and M. Mandel: Corrosion Science, **53** (2011) 624–629.

[35] B. Elsener, M. Crobu, M.A. Scorciapino and A. Rossi: Journal of Applied Electrochemistry. **38** (2008) 1053-1060.

[36] C.N. Cao: Principles of Electrochemistry of Corrosion, Chemical Industry Press, (1985) 322-346.

# Chapter 3 Joint strength and microstructures of SUS304 stainless steel joints brazed with Fe-Cr-based brazing filler metals

## 3.1 Introduction

Ni-based brazing filler metals always contain B, Si and/or P in order to depress the melting point, and the addition of these elements results in the formation of brittle phases such as borides, silicide and phosphides [1-16]. For that reason, it is required to restrict a small clearance of 50 -100 μm to obtain a joint of high-strength and high reliability [2, 9]. For Fe-20Cr-43Ni-10P and Fe-20Cr-20Ni-8P-5Si-2Mo, it is found in practice that a smaller clearance is required than that for Ni-based brazing filler metals to obtain appropriate joint strength [17]. Consequently, as the large joint clearance must be necessary, high production costs arise up and the size of brazed components is also limited.

In this chapter, SUS304 stainless steel joints are brazed with Fe-Cr-based brazing filler metals. Microstructures, joint strength, fracture mechanism and the effect of clearance on shear strength are investigated in order to understand brazing characteristics of the Fe-Cr-based brazing filler metals.

## 3.2 Experimental procedure

### 3.2.1. Materials

The base metal used in the experiment was commercial SUS304 stainless steel sheet with the thickness of 1 mm. Its chemical compositions in mass percent are given in Table 3.2.1.

Brazing filler metals were made by Tokyo Braze Co. Ltd. For comparison, the conventional Ni-29Cr-6P-4Si (mass%) filler metal was also prepared. The brazing filler metals were in the form of paste. Chemical compositions and melting properties are summarized in Table 3.2.2.

Table 3.2.1 Chemical compositions of base metal (mass%).

| The base metal | C | Si | Mn | P | S | Ni | Cr | Fe |
|---|---|---|---|---|---|---|---|---|
| SUS304 | 0.05 | 0.38 | 1.86 | 0.035 | 0.025 | 8.17 | 18.5 | bal. |

Table 3.2.2 Chemical compositions and melting properties of brazing filler metals.

| Brazing filler metal (mass%) | Solidus temperature (K) | Liquidus temperature (K) |
|---|---|---|
| Fe-20Cr-43Ni-10P | 1175 | 1313 |
| Fe-20Cr-20Ni-8P-5Si-2Mo | 1328 | 1359 |
| Ni-29Cr-6P-4Si | 1259 | 1297 |

### 3.2.2. Specimen preparation

The specimens were prepared according to No. B of JIS Z 3192-3. For brazing experiments, SUS304 stainless steel chips were first ground with SiC emery paper to produce good mating surfaces, and then cleaned in an ultrasonic bath filled with acetone for 15 min. Subsequently, these SUS304 stainless steel chips were dried by hot air before assembly. Clearance is adjusted by sandwiching W wire: no W wire, 50 μm, 100 μm, 200 μm and 300 μm. It should be noted that the clearance without the W wire is about 10 μm. Schematic diagram of a joint is presented in Fig. 3.2.1.

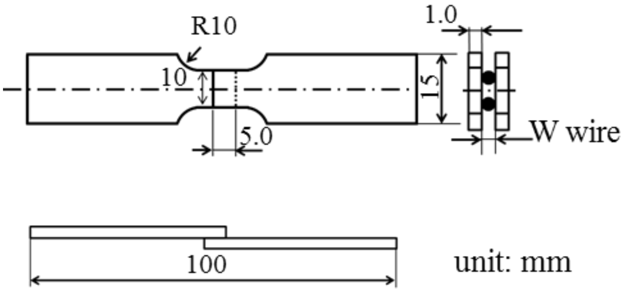

Fig. 3.2.1 Schematic diagram of specimen.

3.2.3 Brazing

Brazing filler metal paste was sandwiched between the base metals, and then fixed with bolts and nuts. The specimens were carefully put into a semicontinuous vacuum furnace. Brazing was performed in a vacuum degree of 50 Pa. The temperature profile in brazing is shown in Fig. 3.2.2. The specimens were preheated at 873 K for 30 minutes at the heating rate of 20 K/min.

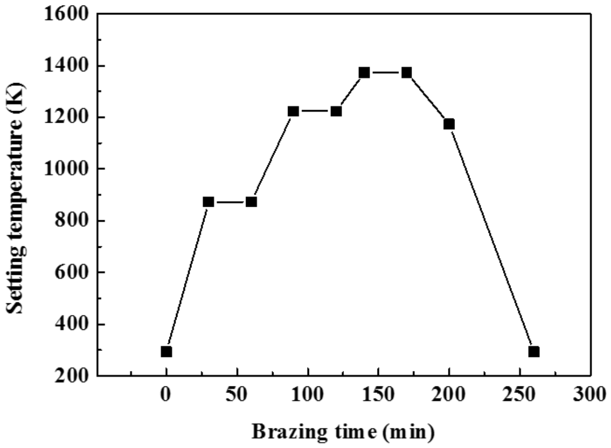

Fig. 3.2.2 Temperature profile in brazing.

Subsequently, the specimens were heated till 1223 K at the heating rate of approximately 12 K/min and held for 30 minutes, and then heated till the brazing temperature of 1373 K at the rate of 7.5 K /min. The specimens were brazed at brazing temperature of 1373 K for 30 minutes, and then slowly cooled to 1173 K at a cooling rate of approximately 7 K/min, followed by quenching to room temperature at a cooling rate of approximately 15 K/min in a nitrogen atmosphere (5 L /min).

### 3.2.4 Shear strength testing

Shear strength measurements were performed by a universal testing machine (Instron) to evaluate tensile properties at room temperature. The cross-head speed was 1 mm/min. The shear strength was determined as the average taken from five brazed samples. The fracture surfaces were analyzed by an electron probe X-ray micro analyzer (EPMA). Furthermore, the two sides fracture surfaces after the shear test were bonded with adhesive (Aron Alpha) and embedded in epoxy resin. The cross-sections of fractured surfaces of brazed joints were observed by a charge-coupled device (CCD) scope.

### 3.2.5 Microstructure analysis

The brazed samples were prepared for microstructural examinations according to the standard metallographic techniques. The specimens were abraded in, #100, #400, #800, #1200, #2400 and #4000 grit emery papers and then polished by 1.0 µm aluminum suspension. The microstructure analysis of cross-sections was carried out by an EPMA.

### 3.2.6 Vickers hardness test

Vickers hardness was obtained using a Vickers diamond indentator at a 100 gf load for 15 seconds. Vickers hardness test was performed for five times on every analyses area, and then the average was taken.

## 3.3 Results and discussion

### 3.3.1 Microstructures of brazed joints

#### 3.3.1.1 Microstructures of joints brazed with Fe-20Cr-43Ni-10P

Since the joint microstructure is an indicator of the strength of the specimen, it is important to examine the joint microstructure for evaluation of mechanical properties. Brazing of SUS304 stainless steel was performed with Fe-20Cr-43Ni-10P in the clearance of 10, 50, 100, 200 and 300 μm. Back-scattered electron images of the joints are shown in Fig. 3.3.1. The back-scattered electron images does not provide topographic contrast but primarily show the element distribution in the joint. Consequently, the area of the specimen containing high-atomic number elements appears light, while the area with low-atomic number elements appears dark. In the clearance of 10 μm, only a dark gray phase is observed in the brazed layer of the joint. It is apparent that the distribution of elements in the brazed joint is uniform, and there is only a phase in the brazed joint. When the clearance is more than 50 μm, there are a meshed dark phase and light gray phase in the center of the joints. Additionally, a serrated light gray phase is presented between these regions and the base metal as well. It is apparent that the distribution of elements in the brazed joint is not uniform, and there are at least three phases in the brazed joint.

Fig. 3.3.2 shows mapping analysis results for cross sections of the joints brazed with Fe-20Cr-43Ni-10P at various clearances. As shown in Fig. 3.3.2 (a), in the clearance of 10 μm, each element is present uniformly in the brazed layer. Ni is observed to be remarkably present in a light gray layer. Table 3.3.1 shows chemical compositions of the phase in the joint brazed with Fe-20Cr-43Ni-10P in the clearance of 10 μm. The ratio of Fe: Cr: Ni: P in the light gray layer is 58.0: 17.3: 23.9: 0.8 (mass%), and in comparison with the base material (Fe: Cr: Ni: P = 70.98: 18.5: 8.17: 0.035 in mass%, shown in Table 3.2.1), the Ni content is significantly increased, and the Fe content is found to decrease. Therefore, the light gray phase is confirmed to be diffusion layer by Ni mainly diffusing from the brazing filler metal to the base material. On the other hand, the ratio of Fe: Cr: Ni: P of the dark gray phase in the brazed layer is 35.2: 38.1: 10.5: 16.2 (mass%), compared with the brazing filler metal, the rise of Fe, Cr and P is recognized. It is inferred to be a Cr-P-Fe-Ni-based compounds according to the quantitative analysis results.

As shown in Fig. 3.3.2 (b), (c), (d) and (e), when the clearance is more than 50 μm, each element is unevenly distributed in the light gray or dark gray phase, in particular, it was

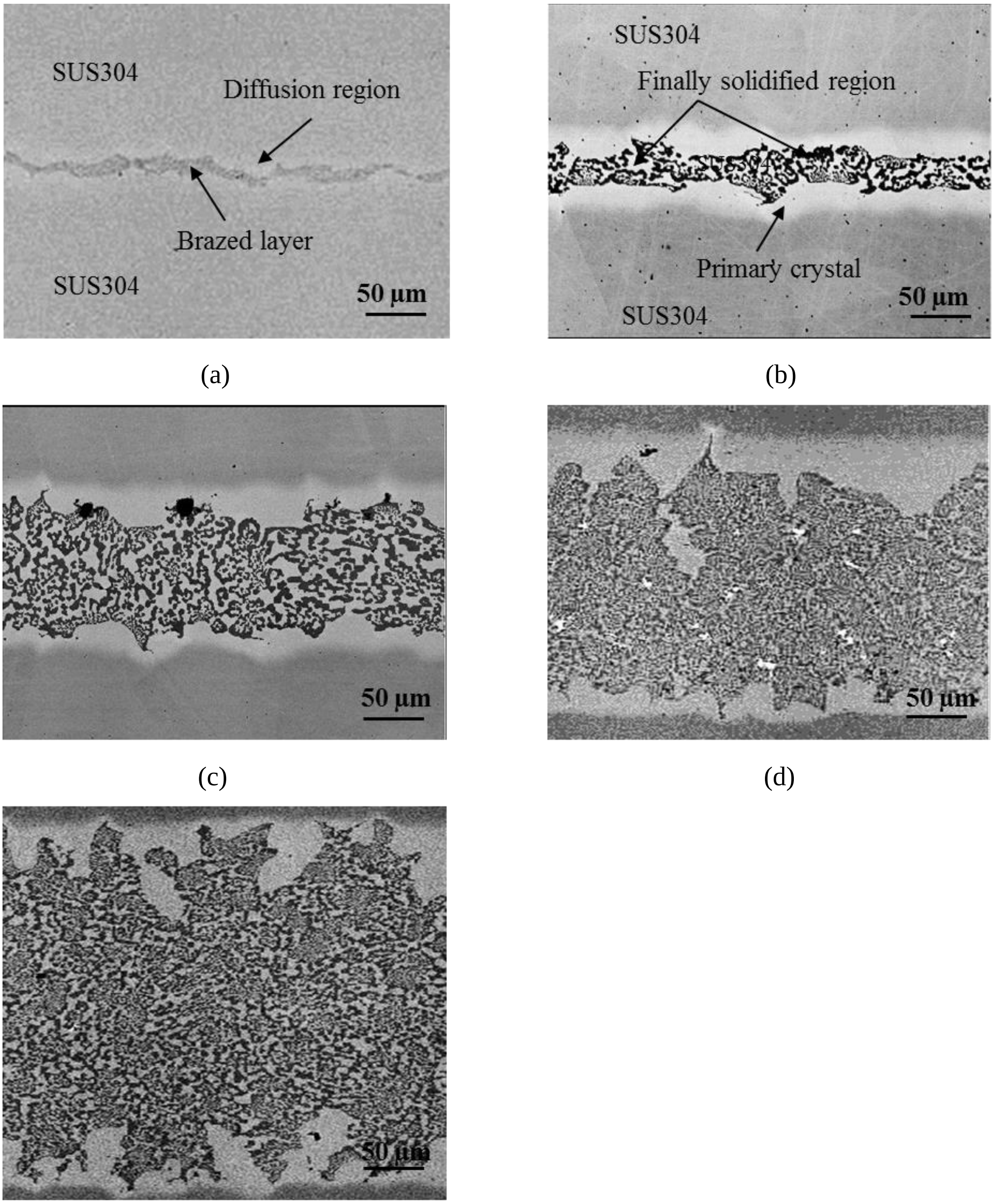

Fig. 3.3.1 Microstructures of SUS304 joints brazed with Fe-20Cr-43Ni-10P filler metal in clearances of (a) 10 µm, (b) 50 µm, (c) 100 µm, (d) 200 µm, (d) 300 µm (back-scattered electron images).

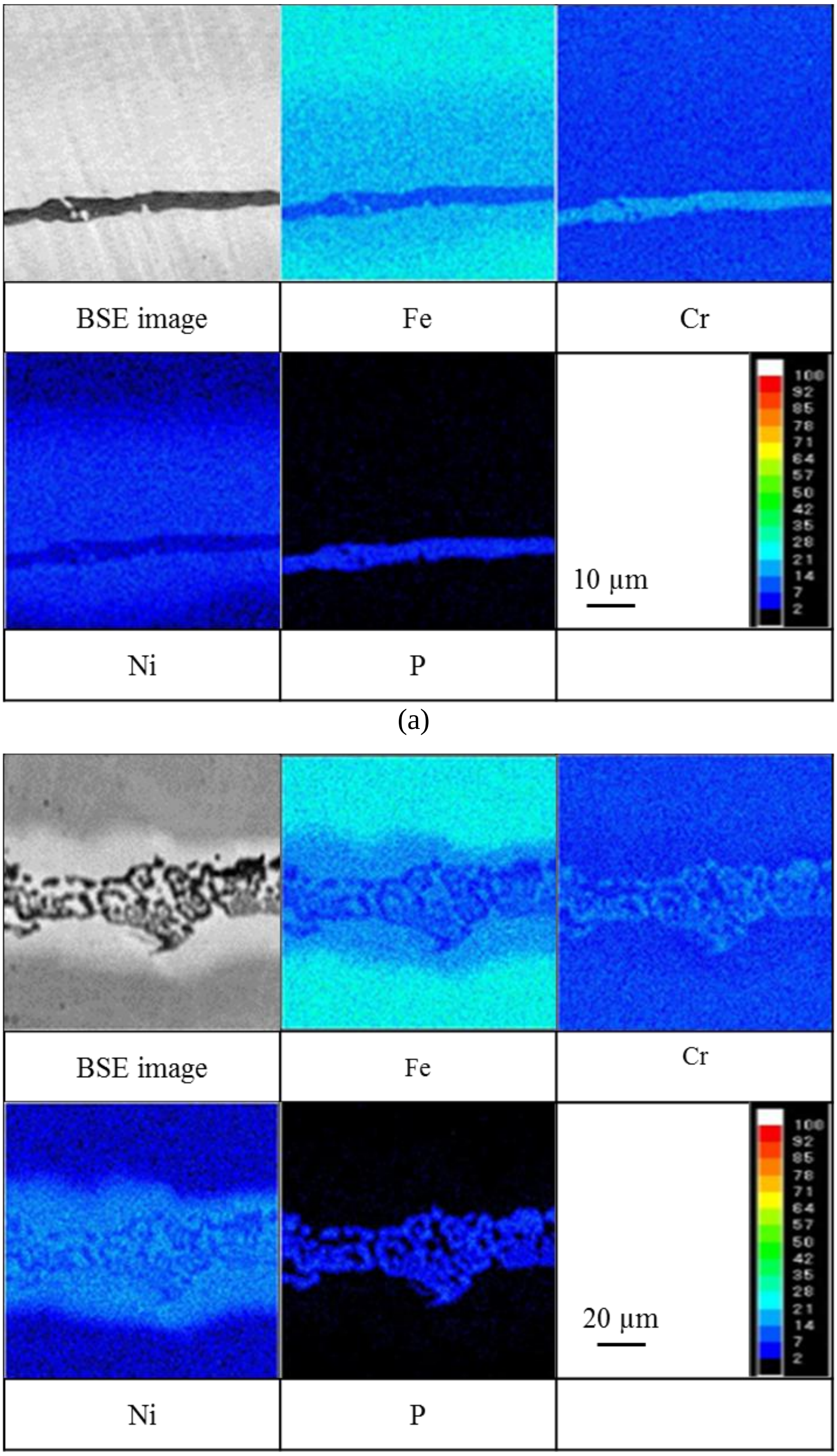

(a)

(b)

Fig. 3.3.2 Mapping analysis results for cross sections of brazed joints with Fe-20Cr-43Ni-10P filler metal in clearances of (a) 10 μm, (b) 50 μm.

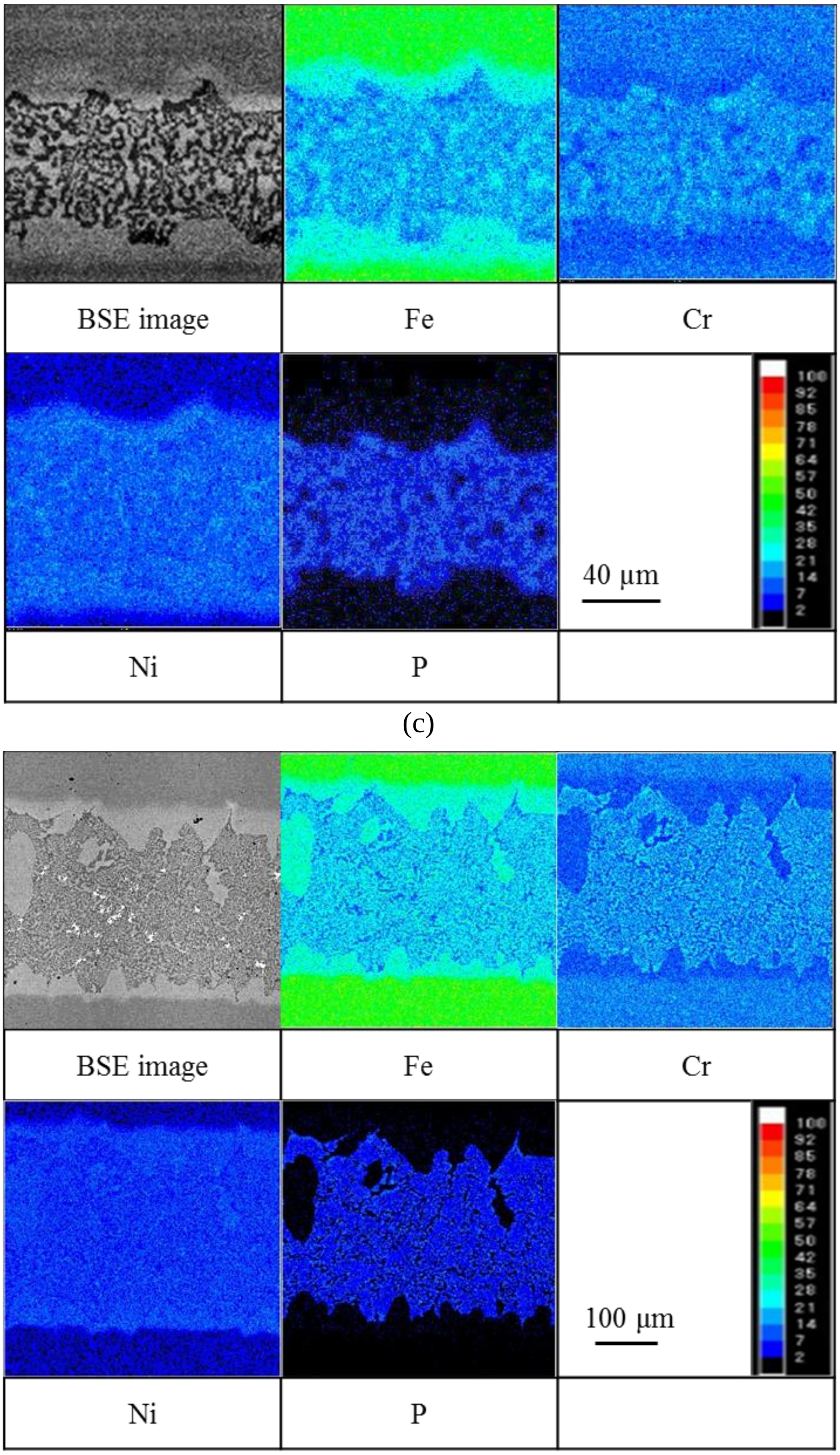

(c)

(d)

Fig. 3.3.2 Mapping analysis results for cross sections of brazed joints with Fe-20Cr-43Ni-10P filler metal in clearances of (c) 100 µm, (d) 200 µm.

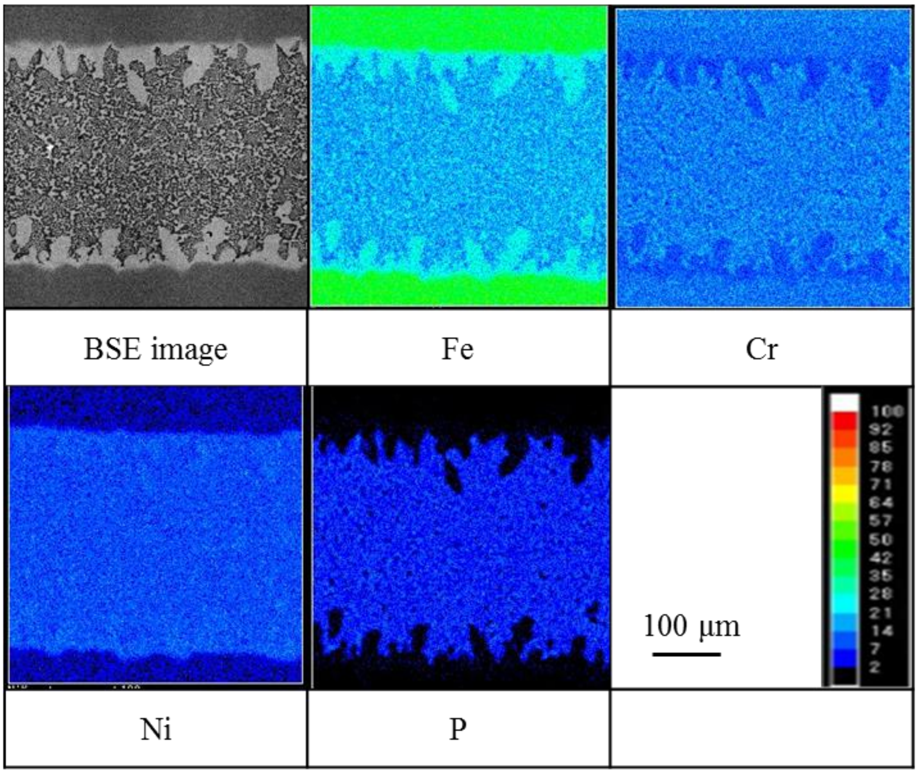

(e)

Fig. 3.3.2 Mapping analysis results for cross sections of brazed joints with Fe-20Cr-43Ni-10P filler metal in clearances of (a) 10 μm, (b) 50 μm, (c) 100 μm, (d) 200 μm, (e) 300 μm.

Table 3.3.1 Chemical compositions of phases in joint brazed with Fe-20Cr-43Ni-10P filler metal in clearance of 10 μm.

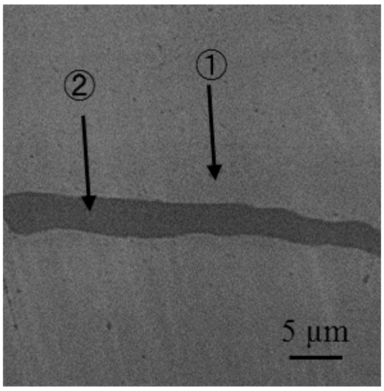

| Analysis | Chemical composition (mol% / mass%) | | | |
|---|---|---|---|---|
| area | Fe | Cr | Ni | P |
| ① | 57.5/58.0 | 18.3/17.3 | 22.6/23.9 | 1.6/0.8 |
| ② | 30.5/35.2 | 35.5/38.1 | 8.7/10.5 | 25.3/16.2 |

Table 3.3.2 Chemical compositions of phases in joint brazed with Fe-20Cr-43Ni-10P filler metal in clearance of 50 μm.

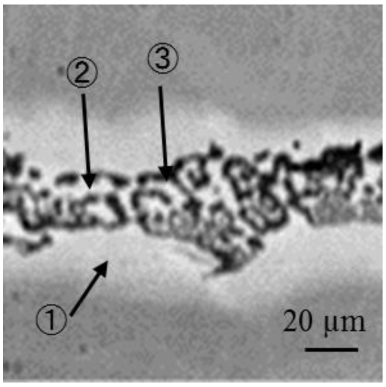

| Analysis | Chemical compositions (mol% / mass%) | | | |
|---|---|---|---|---|
| area | Fe | Cr | Ni | P |
| ① | 42.8/42.7 | 18.2/17.0 | 37.7/39.6 | 1.3/0.7 |
| ② | 43.4/45.8 | 15.8/15.5 | 34.4/38.1 | 1.1/0.6 |
| ③ | 15.2/18.0 | 34.0/37.4 | 19.4/24.0 | 31.4/20.6 |

Table 3.3.3 Chemical compositions of phases in joint brazed with Fe-20Cr-43Ni-10P filler metal in clearance of 200 μm.

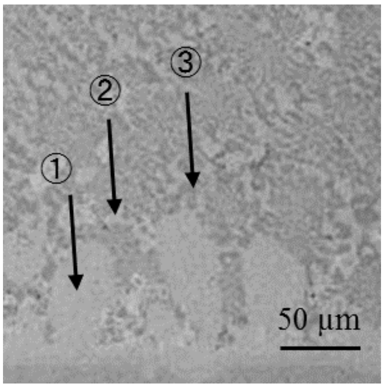

| Analysis | Chemical compositions (mol% / mass%) | | | |
|---|---|---|---|---|
| area | Fe | Cr | Ni | P |
| ① | 47.0/46.9 | 17.9/16.7 | 33.9/35.7 | 1.2/0.7 |
| ② | 46.0/45.7 | 13.8/12.8 | 39.2/40.9 | 1.0/0.6 |
| ③ | 17.9/21.4 | 32.0/35.7 | 16.2/20.4 | 33.9/22.5 |

observed that P is segregated only into the dark gray phase. Table 3.3.2 shows chemical compositions of the phases in the joint brazed with Fe-20Cr-43Ni-10P in the clearance of 50 μm. In the serrated light gray phase in contact with the base metal, Fe: Cr: Ni: P is 42.7: 17.0: 39.6: 0.7 (mass%), as compared with the light gray phase in the clearance of 10 μm, Fe content is reduced. On the other hand, the Ni content is found to increase. In addition, the P content in the phase decreases significantly in comparison with the brazing filler metal component, the Ni content is close to the brazing filler metal component. In the meshed light gray phase, Fe: Cr: Ni: P is 45.8: 15.5: 38.1: 0.6 (mass%), it is of almost same components as the serrated light gray phase in contact with the base material. Hence, it is evident that the light gray phase is different from the light gray phase shown in Fig. 3.3.1 (a). On the other hand, in the dark gray phase, Fe: Cr: Ni: P is 18.0: 37.4: 24.0: 20.6 (mass%), and it is confirmed that P is enriched. From the quantitative analysis result, the light gray phase is a Fe-Cr-Ni solid-solution phase and the dark gray phase is Cr-P-Fe-Ni-based compounds.

Table 3.3.3 shows chemical compositions in the clearance of 200 μm. The almost same results as the joint brazed in the clearance of 50 μm are obtained.

The microstructure of a joint is determined not only by the brazing filler constituents, but also by isothermal transformation and solidification [18]. The isothermal transformation is made up of three stages: the isothermal dissolution of the matrix metal, isothermal solidification in the matrix metal/molten brazing interface and solid state diffusion homogenization [19]. In the case of the conventional Ni-based brazing filler metal, after the brazing filler metal melts, the isothermal dissolution of the matrix steel begins to occur, and the steel begins to dissolve into the molten feller metal. Continued dissolution occurs supersaturation of Fe in the liquid, resulting in increasing of the melting point of the molten filler metal. The “isothermal solidification” happens when the melting point of the brazing filler exceeds the brazing temperature, leading to epitaxial nucleation of solid $\gamma$ -Ni (Fe, Si) islands [18]. These reactions rapidly proceed until the islands coalesce, separating the matrix metal from the liquid. Isothermal solidification inform a scalloped region combined to the matrix steel. The resulting structure of the region is composed of $\gamma$ -Ni (Fe, Si) cells with a distinct orientation relationship to the matrix steel [18]. And then solid state diffusion homogenization occurs. Fe, Ni and Si diffuse though the $\gamma$-Ni (Fe, Si)/steel interface, leading to the growing $\gamma$ -Ni (Fe, Si) cells, and the primary crystal of $\gamma$ -Ni (Fe, Si) solid-solution is formed in the interface [20]. During the followed solidification, $\gamma$-Ni (Fe, Si) and phosphide eutectic structure are produced in the center of the joint. In this study, as shown in Fig. 3.3.1, the microstructures are similar to that with Ni-based filler metals when the clearance is not less than 50 μm although the chemical compositions of Fe and Ni are different. Therefore, it is implied that the mechanism of the joint brazed with Fe-20Cr-43Ni-10P is similar to that of the joint with the conventional Ni-based brazing. Thus, in Fig. 3.3.1(b), the serrated bright gray phases in contact with the matrix steel are present as primary crystals, and it is determined that the mesh region is the final solidified region. In addition, there is a somewhat dark gray region of approximately 10 μm thickness exhibited between the primary crystal and the matrix steel, it is considered that the region is a diffusion layer formed by the diffusion of Ni according to Fig. 3.3.2 (b). In the clearance of 100 μm, 200 μm and 300 μm, the mechanism of microstructure formation can be interpreted in the same way as the clearance of 50 μm.

### 3.3.1.2 Microstructures of joints brazed with Fe-20Cr-20Ni-8P-5Si-2Mo

Back-scattered electron images of the joints brazed with Fe-20Cr-20Ni-8P-5Si-2Mo in the clearance of 10 μm, 50 μm, 100 μm, 200 μm and 300 μm are shown in Fig. 3.3.3. Similar microstructures to Fe-20Cr-43Ni-10P are observed. However, the microstructures of the final solidification regions are finer because of Mo addition [21-23].

Fig. 3.3.4 shows mapping analysis results for cross sections of the joints brazed with Fe-20Cr-20Ni-8P-5Si-2Mo in various clearances. As shown in Fig. 3.3.4 (a), each element is uniformly present in the brazed layer in the clearance of 10 μm. It is observed that Ni and Si remarkably diffused from the joints to the base metal. On the other hand, when the clearance is more than 50 μm, almost the same results as Fe-20Cr-43Ni-10P are obtained.

Table 3.3.4 shows chemical compositions of the phases in the joint brazed with Fe-20Cr-20Ni-8P-5Si-2Mo in the clearance of 10 μm, Ni and Si diffused from the brazing layer to the matrix steel. The ratio of Fe: Cr: Ni: P: Si in the brazing layer is 37.0: 43.3: 3.2: 16.4: 0.1 (mass%), and it is confirmed that the phase is enriched in Cr and P. In the clearance of 50 μm, the ratio of Fe: Cr: Ni: P: Si in the primary crystal is 64.4: 19.7: 11.8: 0.4: 3.7 (mass%). In comparison with Fe-20Cr-20Ni-8P-5Si-2Mo, the P content is significantly reduced. The ratio of Fe: Cr: Ni: P: Si in the bright gray phase of the final solidified region is 62.4: 19.5: 13.9: 0.2: 4.0 (mass%). It is distinct that the phase is of almost the same components as the primary crystal. The bright gray phase is considered to be a Fe-Cr-Ni-Si-based solid-solution phase. In contrast, the ratio of Fe: Cr: Ni: P: Si in the dark gray phase in the final solidified region is 30.0: 39.1: 7.8: 22.0: 1.1 (mass%), and the dark gray phase is confirmed to be P-rich phase. This phase is inferred to be a Cr-P-Fe-Ni-based compound phase according to the quantitative analysis results. In the clearance of 200 μm, the constituent of every phase has not changed much as shown in Table 3.3.6, compared with the constituent in the clearance of 50 μm.

As shown in Fig. 3.3.1 (d), Fig. 3.3.3 (d) and Fig. 3.3.3 (e), there are some very bright particles in the brazing layers. The results of the qualitative analysis by EPMA are shown in Table 3.3.7. The amount of W in the light particle is approximately 17-50 mass%. W with high atomic number results in high brightness of the BSE image in EPMA observations. As shown in Fig. 3.3.5, sandwiched W wire is disconnected. These bright particles are located because the disconnected W are blended into microstructure.

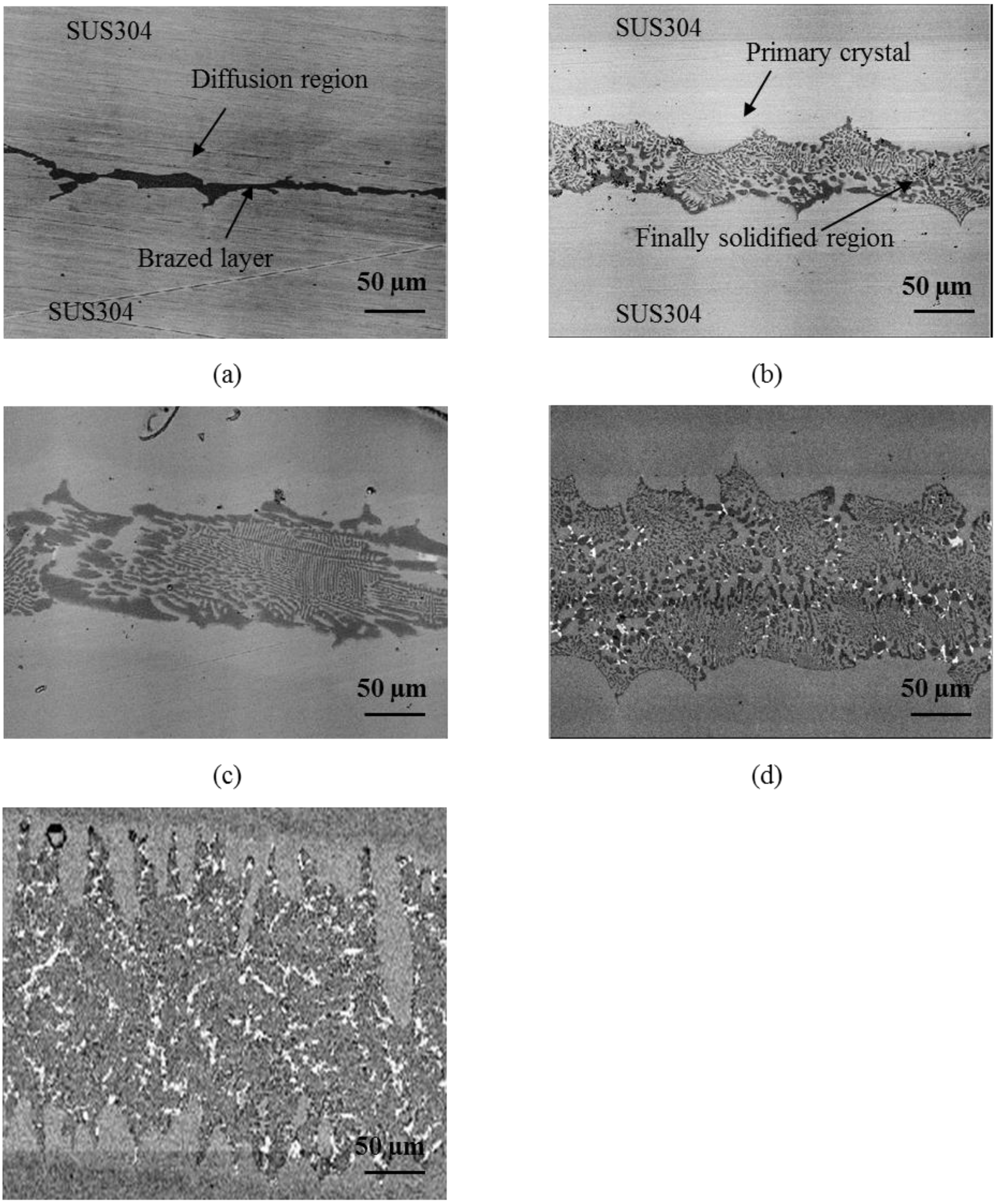

(a)

(b)

(c)

(d)

(e)

Fig. 3.3.3 Microstructures of SUS304 joints brazed with Fe-20Cr-20Ni-8P-5Si-2Mo filler metal in clearances of (a) 10 μm, (b) 50 μm, (c) 100 μm, (d) 200 μm, (e) 300 μm (back-scattered electron images).

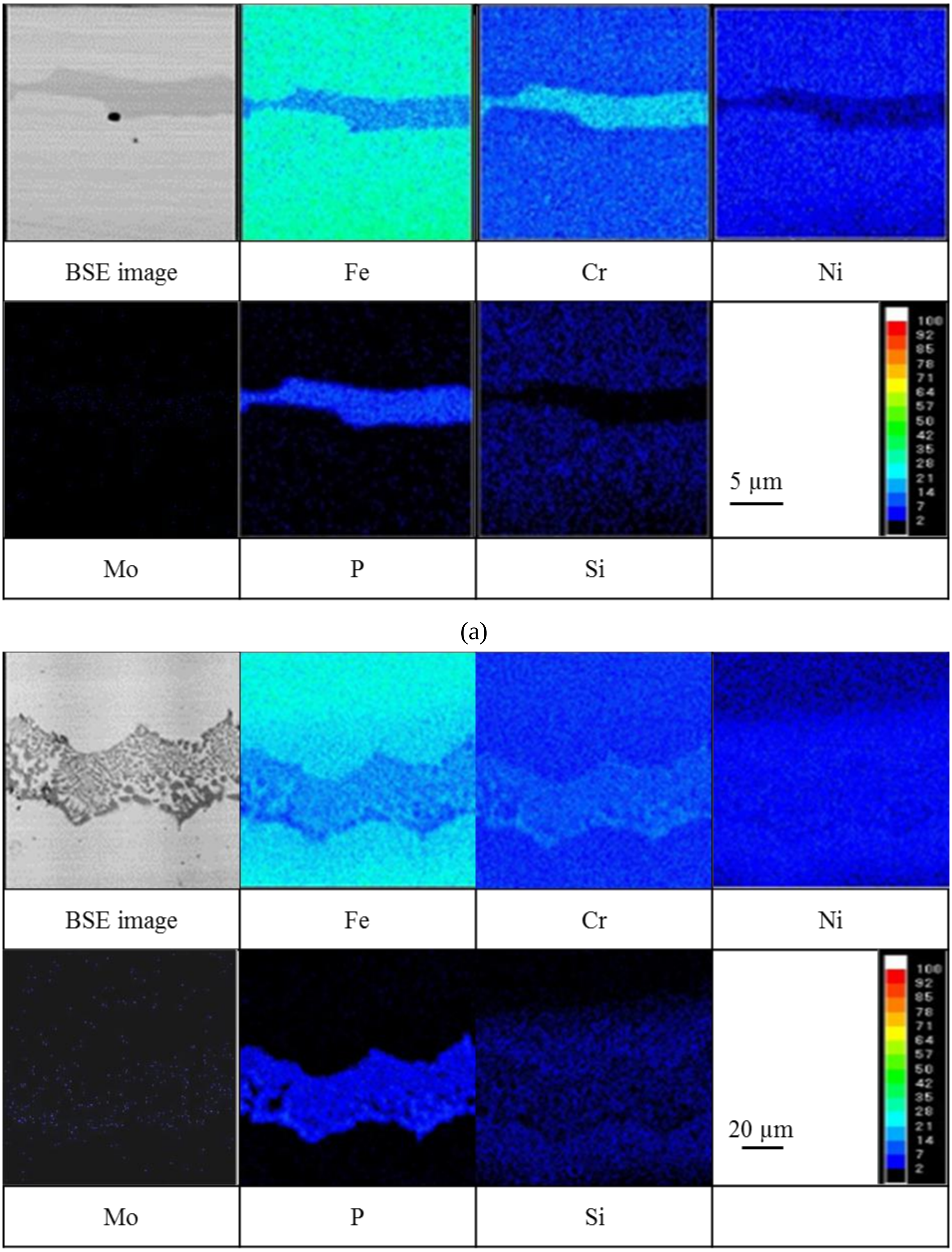

(a)

(b)

Fig. 3.3.4 Mapping analysis results for cross sections of brazed joints with Fe-20Cr-20Ni-8P-5Si-2Mo filler metal in clearances of (a) 10 μm, (b) 50 μm.

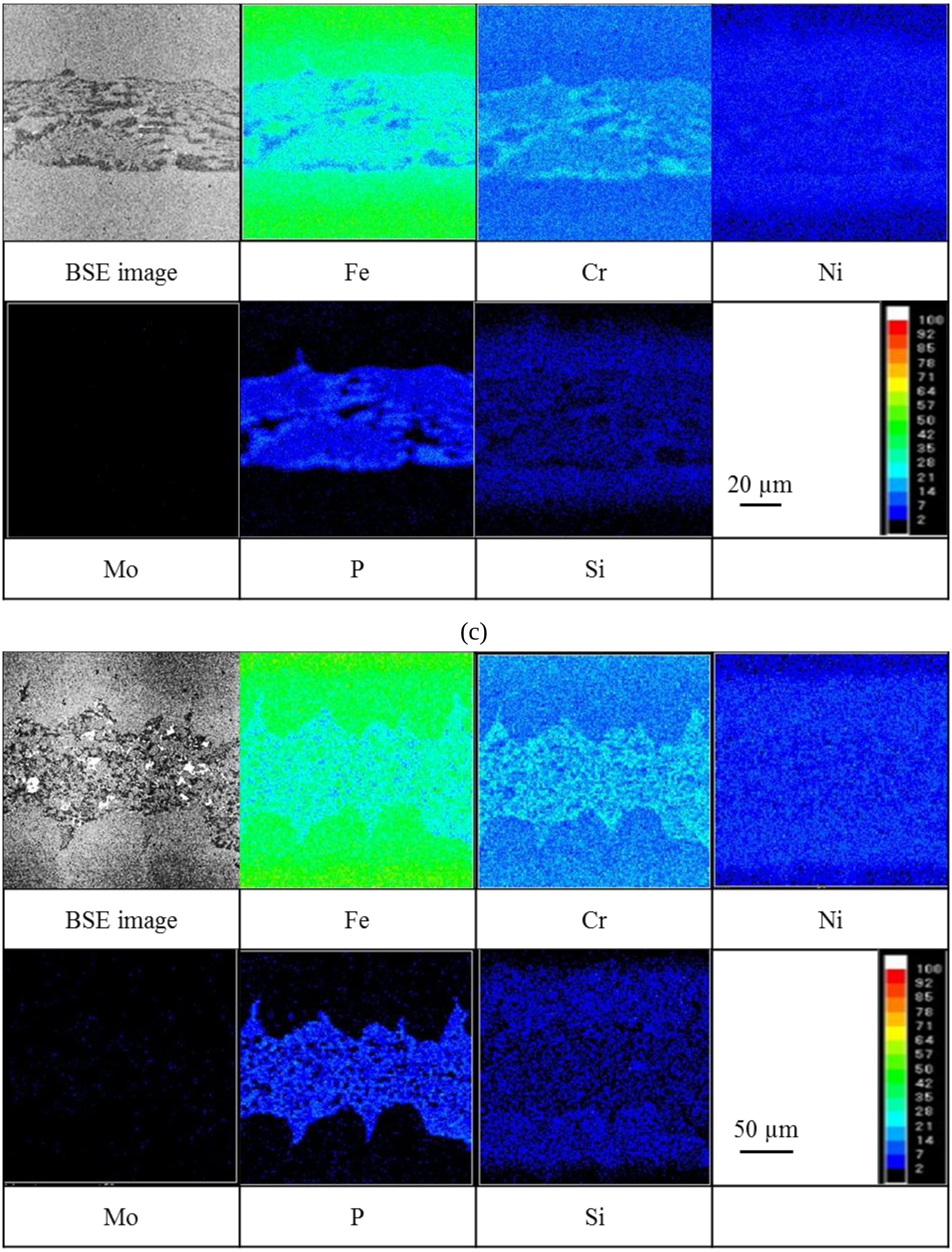

(c)

(d)

Fig. 3.3.4 Mapping analysis results for cross sections of brazed joints with Fe-20Cr-20Ni-8P-5Si-2Mo filler metal in clearances of (c) 100 µm, (d) 200 µm.

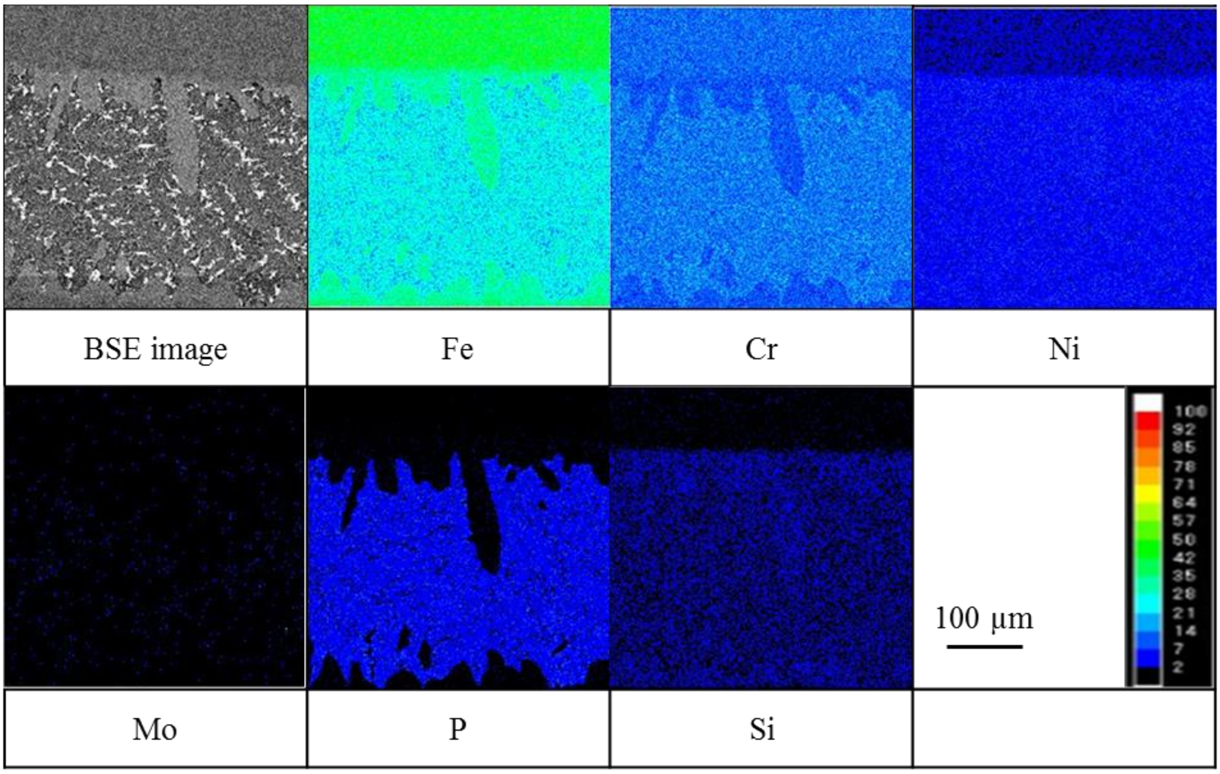

(e)

Fig. 3.3.4 Mapping analysis results for cross sections of brazed joints with Fe-20Cr-20Ni-8P-5Si-2Mo filler metal in clearances of (a) 10 µm, (b) 50 µm, (c) 100 µm, (d) 200 µm, (e) 300 µm.

Table 3.3.4 Chemical compositions of phases in joint brazed with Fe-20Cr-20Ni-8P-5Si-2Mo filler metal in clearance of 10 µm.

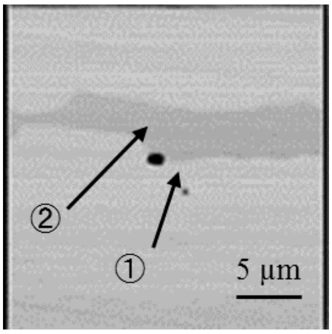

| Analysis area | Chemical composition (mol%/mass%) Fe | Cr | Ni | P | Si |
|---|---|---|---|---|---|
| ① | 63.8/65.2 | 20.5/19.5 | 12.7/13.6 | 0.7/0.4 | 2.3/1.3 |
| ② | 31.8/37.0 | 39.5/43.3 | 2.6/3.2 | 25.6/16.4 | 0.1/0.1 |

Table 3.3.5 Chemical compositions of phases in joint brazed with Fe-20Cr-20Ni-8P-5Si-2Mo filler metal in clearance of 50 µm.

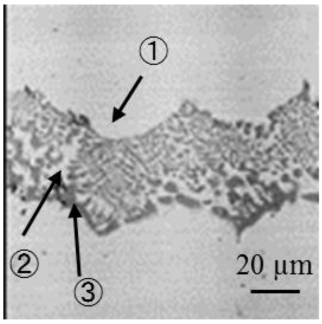

| Analysis area | Chemical composition (mol%/mass%) Fe | Cr | Ni | P | Si |
|---|---|---|---|---|---|
| ① | 61.4/64.4 | 20.2/19.7 | 10.7/11.8 | 0.6/0.4 | 7.0/3.7 |
| ② | 59.4/62.4 | 20.0/19.5 | 12.6/13.9 | 0.4/0.2 | 7.6/4.0 |
| ③ | 24.6/30.0 | 34.6/39.1 | 6.2/7.8 | 32.7/22.0 | 1.9/1.1 |

Table 3.3.6 Chemical compositions of phases in joint brazed with Fe-20Cr-20Ni-8P-5Si-2Mo filler metal in clearance of 200 µm.

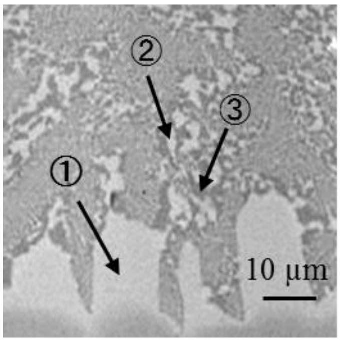

| Analysis area | Chemical composition (mol%/mass%) Fe | Cr | Ni | P | Si |
|---|---|---|---|---|---|
| ① | 64.5/67.2 | 19.7/19.1 | 9.4/10.2 | 0.8/0.5 | 5.6/3.0 |
| ② | 61.5/65.4 | 20.8/20.6 | 7.5/8.5 | 0.8/0.5 | 9.4/5.0 |
| ③ | 25.9/31.4 | 33.3/37.7 | 5.8/7.4 | 33.6/22.6 | 1.4/0.9 |

Table 3.3.7 Results of qualitative analysis for bright particles in brazing layers by EPMA.

| Analysis area | Chemical compositions (mol%/mass%) | | | | | | |
|---|---|---|---|---|---|---|---|
| | W | Fe | Cr | Ni | P | Si | Te |
| Fig. 3.3.1 (d) | 22.9/50.3 | 21.8/14.5 | 29.2/18.1 | 22.6/15.8 | 3.5/1.3 | 0 | 0 |
| Fig. 3.3.3 (d) | 23.7/51.9 | 39.9/26.6 | 17.9/11.1 | 9.8/6.9 | 0 | 8.2/2.7 | 0.5/0.8 |
| Fig. 3.3.3 (e) | 5.1/15.9 | 40.9/38.7 | 25.9/22.8 | 17.5/17.4 | 2.4/1.3 | 8.2/3.9 | 0 |

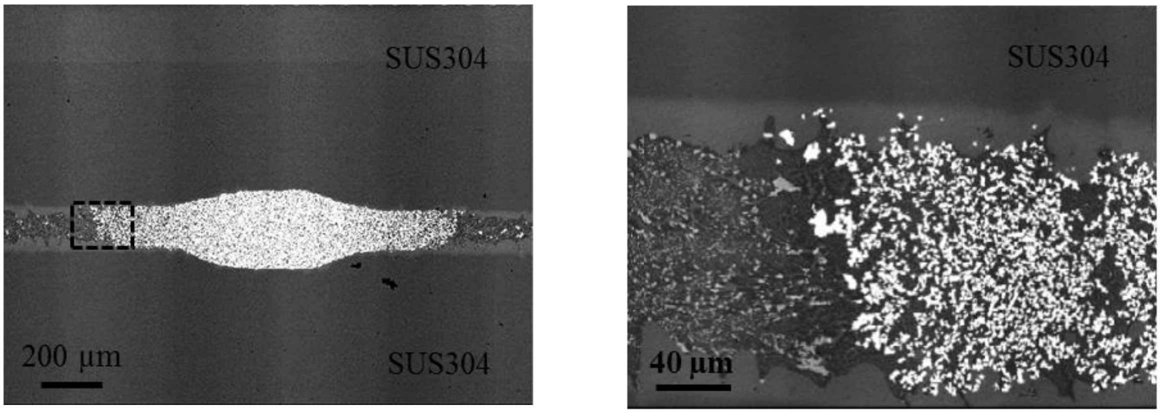

(a) (b)

Fig.3.3.5 Disconnection of sandwiched W wire in joint brazed with Fe-20Cr-20Ni-8P-5Si-2Mo filler metal in clearance of 300 µm (back-scattered electron images).

(a) general view of brazing layer,

(b) magnified image of dotted area shown in (a).

### 3.3.2 Shear strength

Fig. 3.3.6 shows the results of the shear strength test. For every brazing filler metal, the shear strength reaches a maximum value in the clearance of 10 μm and then decreases. In the clearance of 10 μm, shear strength is up to 124 MPa, 137 MPa and 174 MPa for Fe-20Cr-43Ni-10P, Fe-20Cr-20Ni-8P-5Si-2Mo and Ni-29Cr-6P-4Si, respectively.

When the clearance is more than 50 μm, the shear strength is found to fluctuate in a tight range of approximately 10 MPa. Compared with the Ni-base brazing filler metal, the joint brazed with Fe-20Cr-43Ni-10P exhibits a strength of about 100 MPa although the shear strength is inferior to that with the Ni-base brazing filler metal. On the other hand, the joint brazed with Fe-20Cr-20Ni-8P-5Si-2Mo exhibits a comparable shear strength with that brazed with the Ni-base brazing filler metal when the clearance is less than 200 μm.

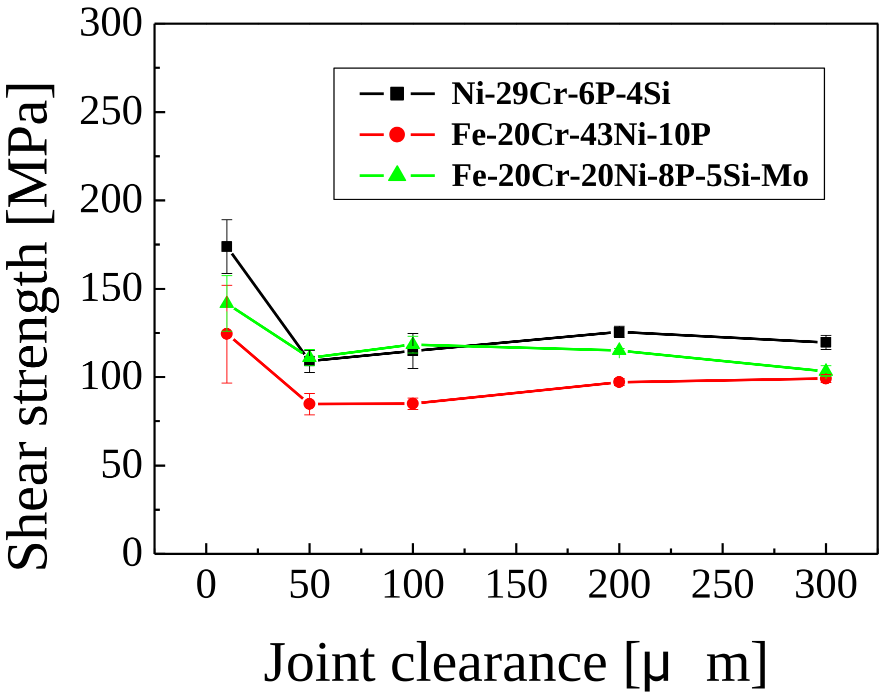

Fig. 3.3.6 Effect of joint clearance on shear strength.

### 3.3.3 Fracture mechanism

Fig. 3.3.7 and Fig. 3.3.8 show the CCD images of cross-sections of the fracture surfaces of the brazed joints with Fe-20Cr-43Ni-10P and Fe-20Cr-20Ni-8P-5Si-2Mo after the shear strength test, respectively. In the clearance of 50 μm, 100 μm, 200 μm and 300 μm, all the joints failed near the interface of the primary crystal and the finally solidified region, not in the central line of the brazed layer. However, in the clearance of 10 μm, fracture location cannot be decided according to Fig. 3.3.7 and Fig. 3.3.8.

Mapping analysis for both fracture surfaces after the shear strength test were performed in the case of the clearance of 10 μm, 50 μm and 200 μm. Fig. 3.3.9-Fig. 3.3.14 present EPMA mapping analysis results for both fracture surfaces of the joints.

In the clearance of 10 μm, as shown in Fig. 3.3.9 and Fig. 3.3.12, the areas, which are poor in Cr and rich in Fe and Ni, are observed on both fracture surfaces. These areas show the characteristic of the diffusion region according to Table 3.3.1 and Table 3.3.4. At the same time, P is detected on the pair of the fracture surfaces. It is noticeable that P exists almost completely in the brazed layer as shown in Fig. 3.3.2 (a) and Fig. 3.3.4 (a). The fracture surfaces show the characteristics of both the diffusion region and the brazed layer. Therefore, it is conformed that the joints failed in the interface of the diffusion region and the brazed layer in the clearance of 10 μm.

In the clearance of 50 μm and 200 μm, as shown in Fig. 3.3.10, 3.3.11, 3.3.13 and 3.3.14, P is distributed throughout on the pair of the fracture surfaces. Different from the clearance of 10 μm, the characteristic of the primary crystal, which has a larger grain size, is not distinctly shown on the fracture surfaces. This fact implies that the finally solidified region has a weaker strength than the primary crystal and provided a low resistance to crack initiation and propagation. The joints failed in the finally solidified region.

Fig. 3.3.15 shows the microstructure of the cross-section of the finally solidified region of the joint brazed with Fe-20Cr-43Ni-10P in the clearance of 300 μm after shear strength test. Fig. 3.3.16 shows the microstructure of the cross-section of the finally solidified region of the joint brazed with Fe-20Cr-20Ni-8P-5Si-2Mo in the clearance of 100 μm after shear strength test. It is found that cracks progressed along the interfaces of the solid-solution phases and phosphide phases in the finally solidified regions of both joints.

Fig. 3.3.17 and Fig. 3.3.18 show the fractograph of the joints with Fe-20Cr-43Ni-10P and Fe-20Cr-20Ni-8P-5Si-2Mo after the shear strength test, respectively. All the joints exhibit brittle fracture mode. The brittleness reduces the shear strength of all the brazed joints.

Table 3.3.8 and Table 3.3.9 show Vickers hardness of the phases in the joints with Fe-20Cr-43Ni-10P and Fe-20Cr-20Ni-8P-5Si-2Mo, respectively. In the clearance of 10 μm, the diffusion region has much lower hardness than the brazed layer, but a little higher than the based metal of SUS304 because of Ni diffusion from the brazing filler in both of the brazing filler metals. In the clearance of more than 50 μm, the hardness of the final solidified region is approximately twice as high as that of the primary crystal in both of the brazing filler metals.

Therefore, in the clearance of 10 μm, large hardness difference results in difference of plastic deformation rate in the interface of the diffusion region and the brazed layer. It is much more difficult for the brazed layer that plastic deformation occurs in comparison with the diffusion region. Under the action of force, there is a large shear stress in the interface of the diffusion region and the brazed layer, stimulating cracks and leading to fracture.

When the clearance is more than 50 μm, the final solidified region emerged in the brazed layer. As shown in Table 3.3.8 and Table 3.3.9, the final solidified region has approximately twice as high hardness as the primary crystal. There is a large shear stress near the interface of the final solidified region and the primary crystal under the action of shear force so that cracks occur. At the same time, the phosphide phase with high hardness causes uneven distribution of hardness in the final solidified region. The cracks process along the interface of the solid-solution phase and phosphide phase in the finally solidified region.

Both P concentration in the clearance of 10 μm and the generation of the phosphide phase in the clearance of more than 50 μm, are the important factors that the shear strength of the joint decrease.

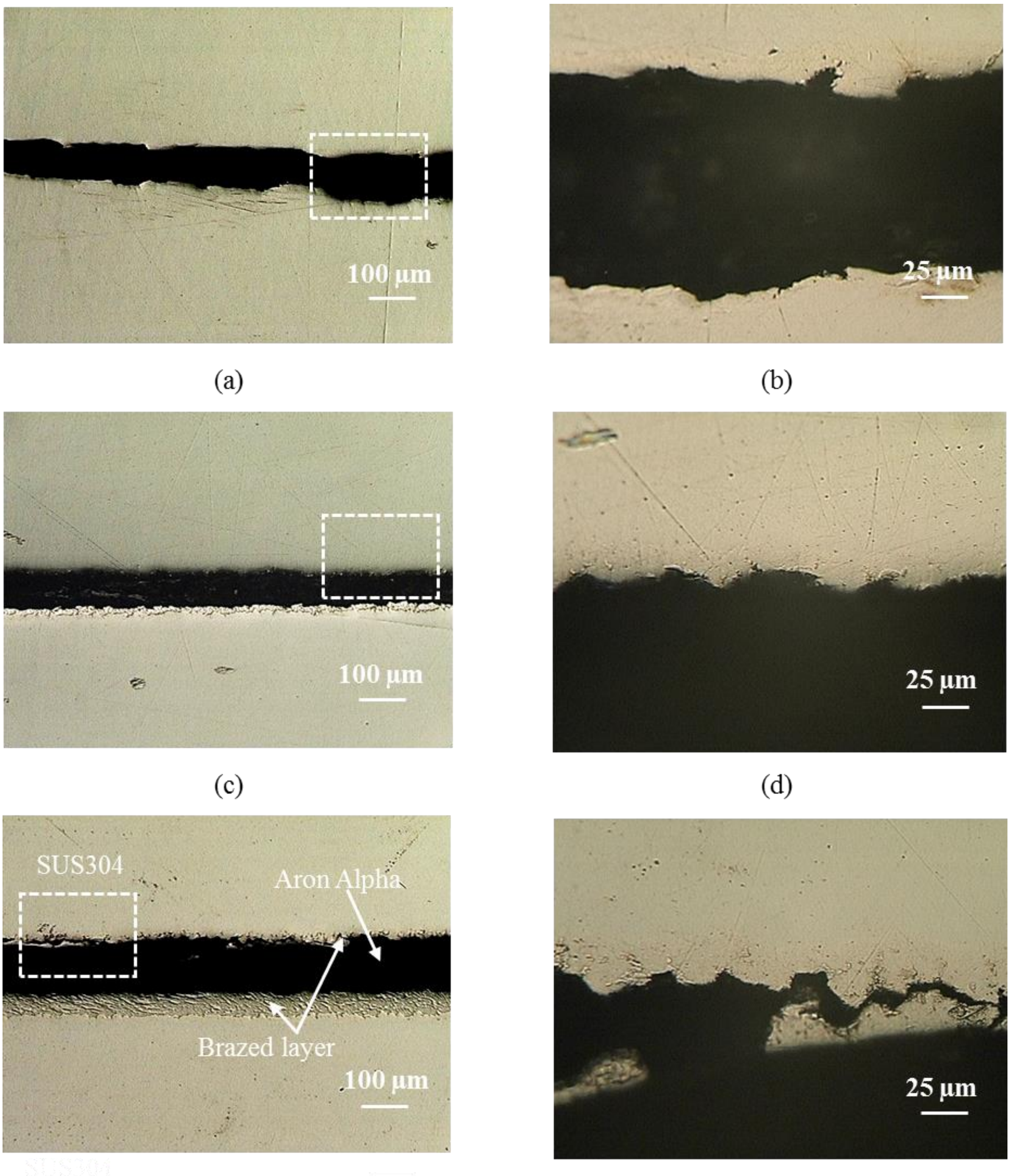

(a) (b)

(c) (d)

(e) (f)

Fig. 3.3.7 CCD images of cross-sections of fractured surfaces of joints brazed with Fe-20Cr-43Ni-10P filler metal in different clearances.

(a) clearance: 10 µm, (b) magnified image of dotted area shown in (a),

(c) clearance: 50 µm, (d) magnified image of dotted area shown in (c),

(e) clearance: 100 µm, (f) magnified image of dotted area shown in (e).

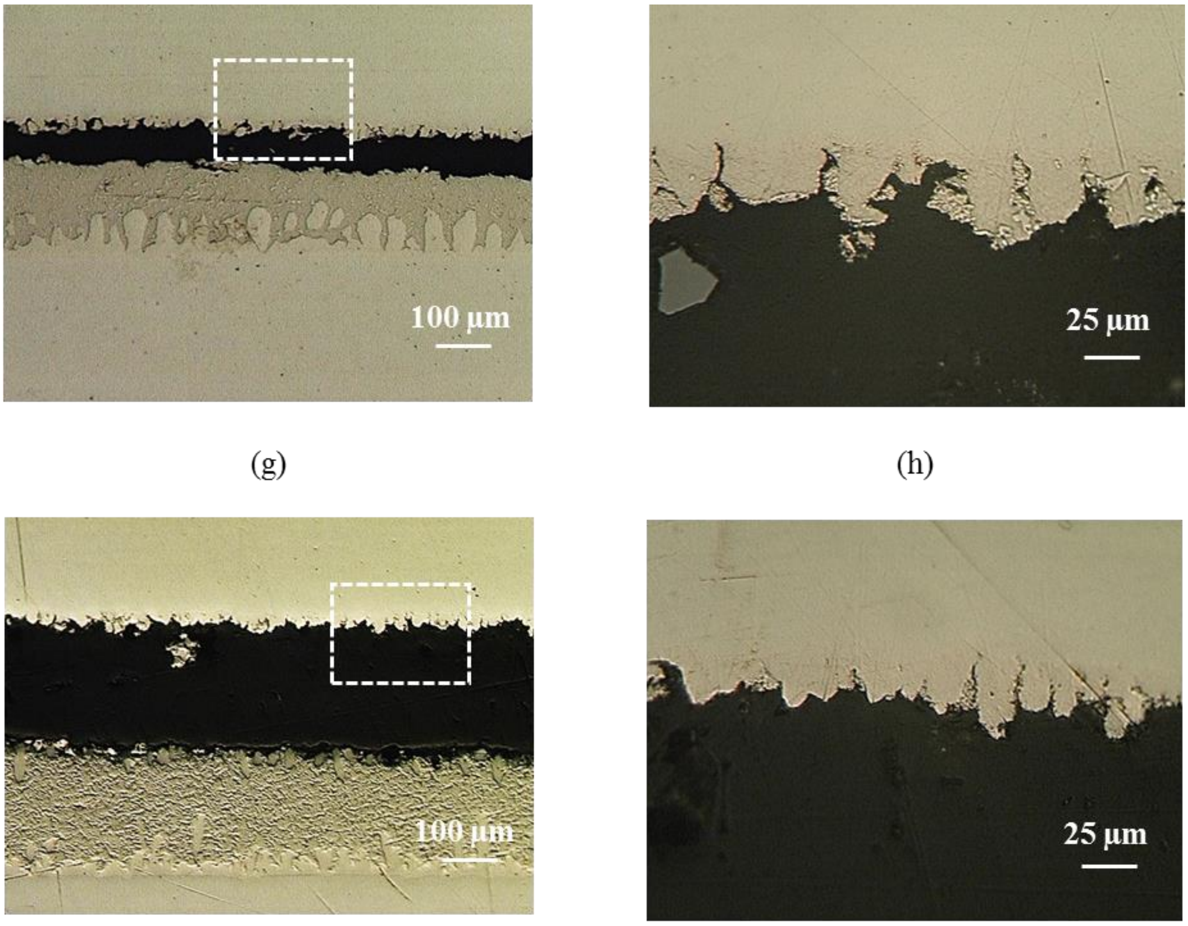

(g) (h)

(i) (j)

Fig. 3.3.7 CCD images of cross-sections of fractured surfaces of joints brazed with Fe-20Cr-43Ni-10P filler metal in different clearances.

(a) clearance: 10 µm, (b) magnified image of dotted area shown in (a),

(c) clearance: 50 µm, (d) magnified image of dotted area shown in (c),

(e) clearance: 100 µm, (f) magnified image of dotted area shown in (e),

(g) clearance: 200 µm, (h) magnified image of dotted area shown in (g),

(i) clearance: 300 µm, (j) magnified image of dotted area shown in (i).

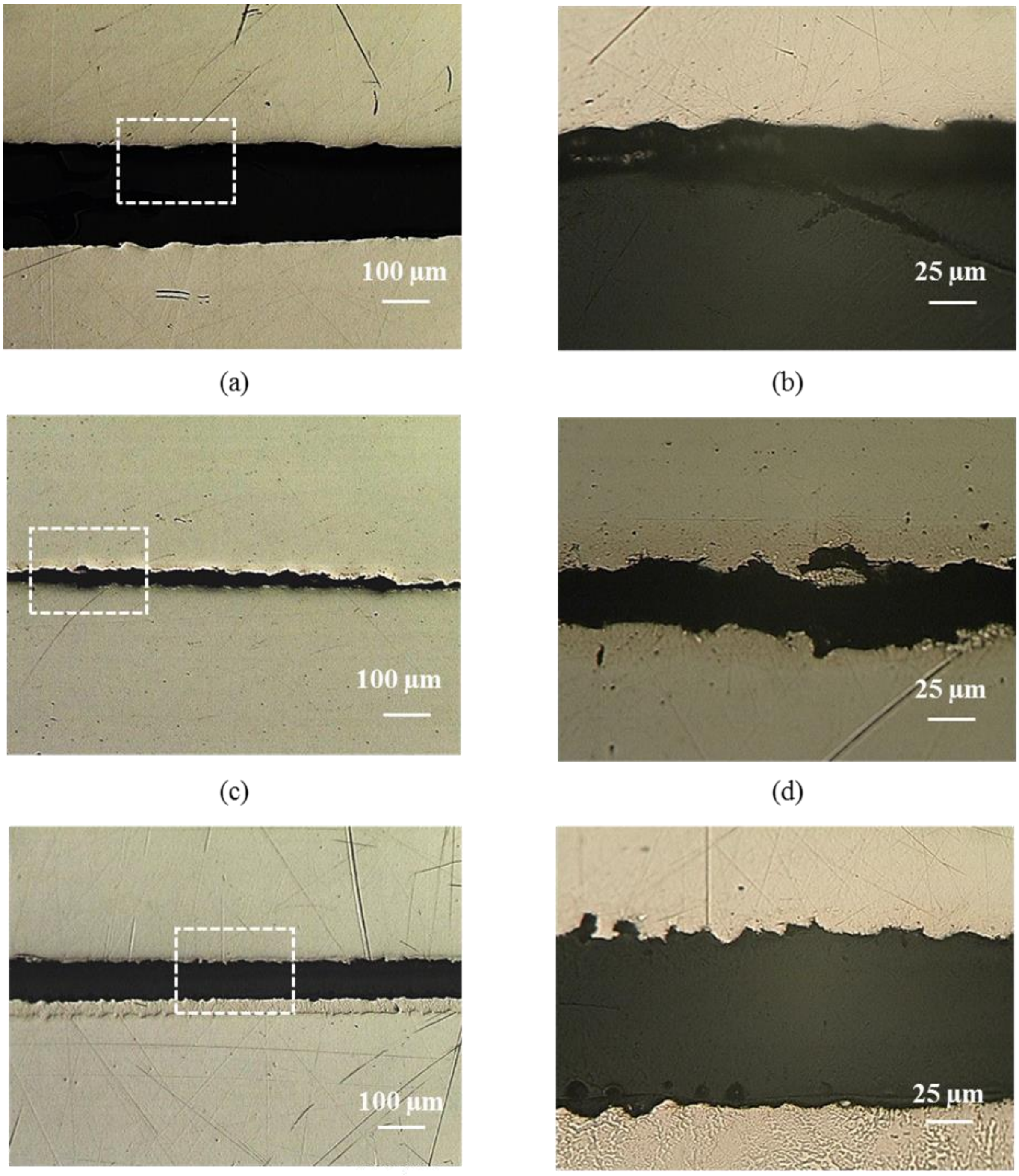

(a) (b)

(c) (d)

(e) (f)

Fig. 3.3.8 CCD images of cross-sections of fractured surfaces of joints brazed with Fe-20Cr-20Ni-8P-5Si-2Mo filler metal in different clearances.

(a) clearance: 10 µm, (b) magnified image of dotted area shown in (a),

(c) clearance: 50 µthat of m, (d) magnified image of dotted area shown in (c),

(e) clearance: 100 µm, (f) magnified image of dotted area shown in (e).

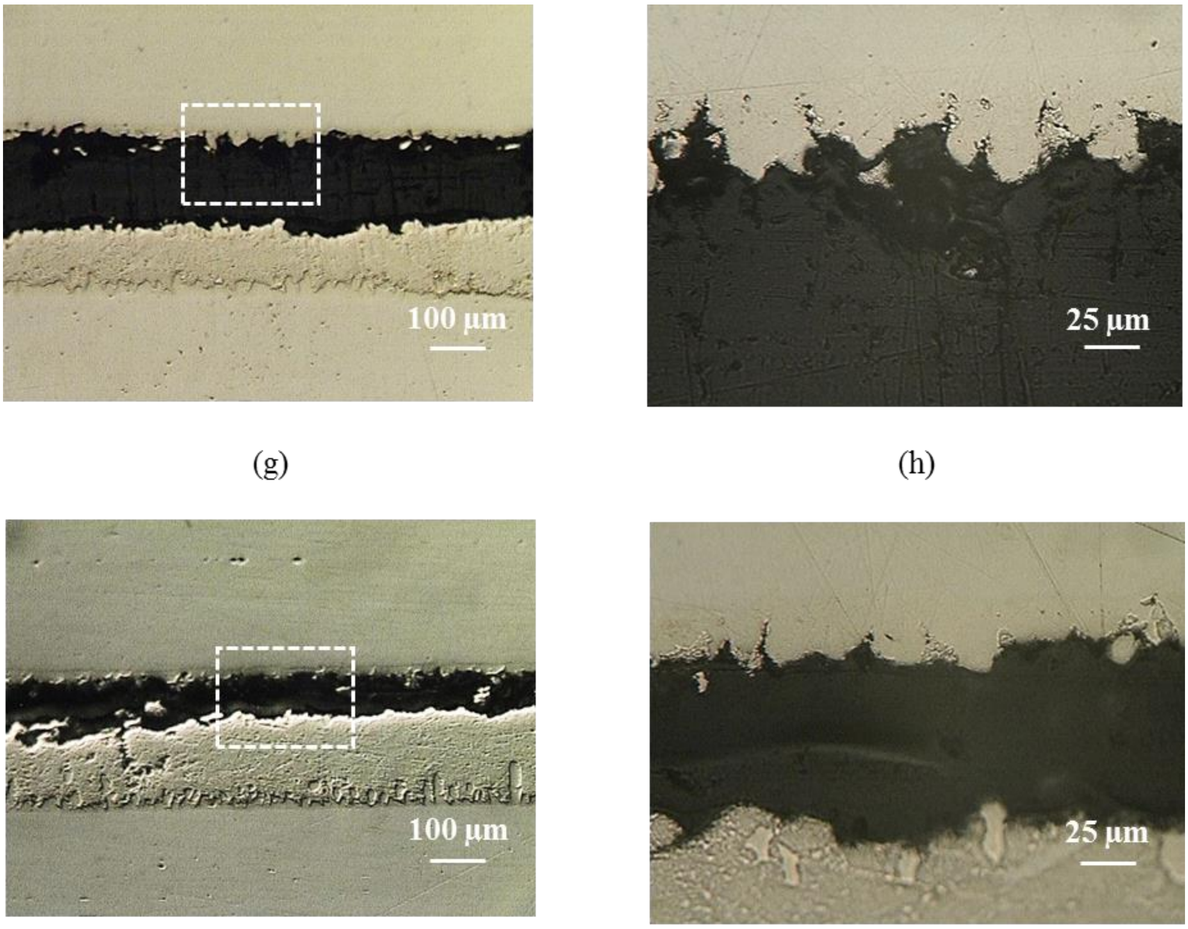

(g) (h)

(i) (j)

Fig. 3.3.8 CCD images of cross-sections of fractured surfaces of joints brazed with Fe-20Cr-20Ni-8P-5Si-2Mo filler metal in different clearances.

(a) clearance: 10 µm, (b) magnified image of dotted area shown in (a),

(c) clearance: 50 µm, (d) magnified image of dotted area shown in (c),

(e) clearance: 100 µm, (f) magnified image of dotted area shown in (e),

(g) clearance: 200 µm, (h) magnified image of dotted area shown in (g),

(i) clearance: 300 µm, (j) magnified image of dotted area shown in (i).

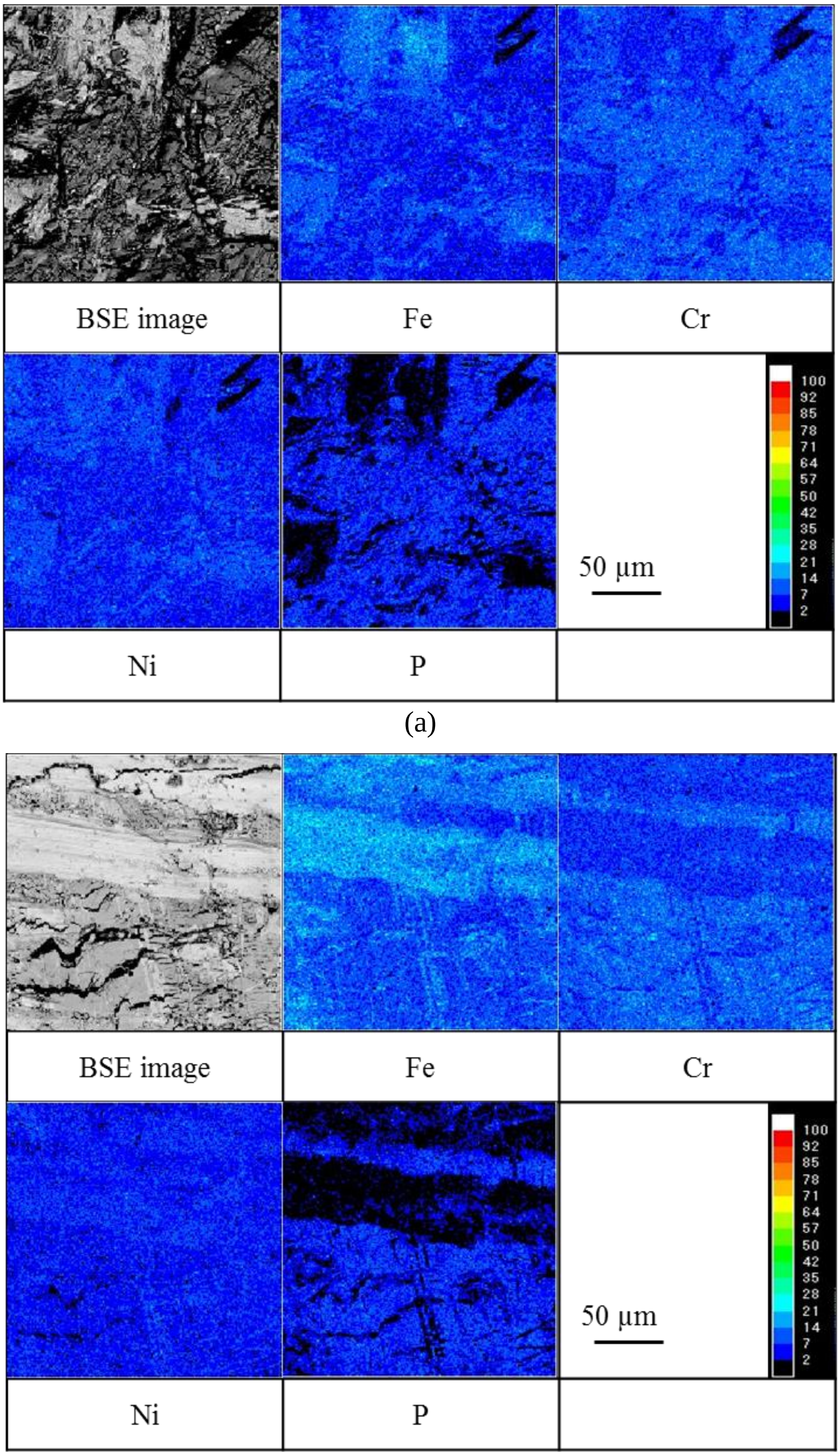

(a)

(b)

Fig. 3.3.9 EPMA mapping analysis results for both fracture surfaces of joint brazed with Fe-20Cr-43Ni-10P filler metal after shear strength test in clearance of 10 μm.

(a) one side, (b) other side.

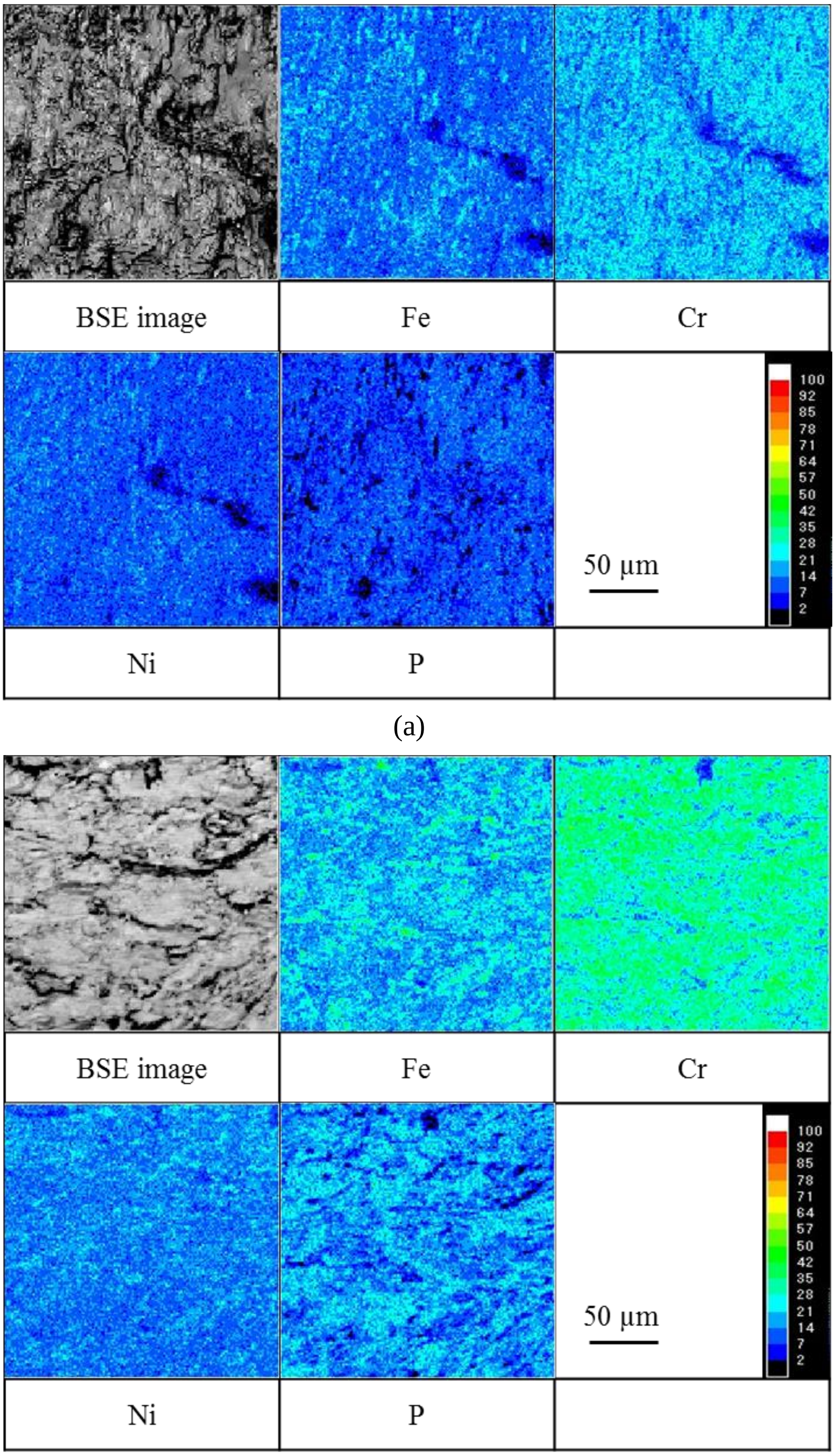

(a)

(b)

Fig. 3.3.10 EPMA mapping analysis results for both fracture surfaces of joint brazed with Fe-20Cr-43Ni-10P filler metal after shear strength test in clearance of 50 μm.
(a) one side, (b) other side

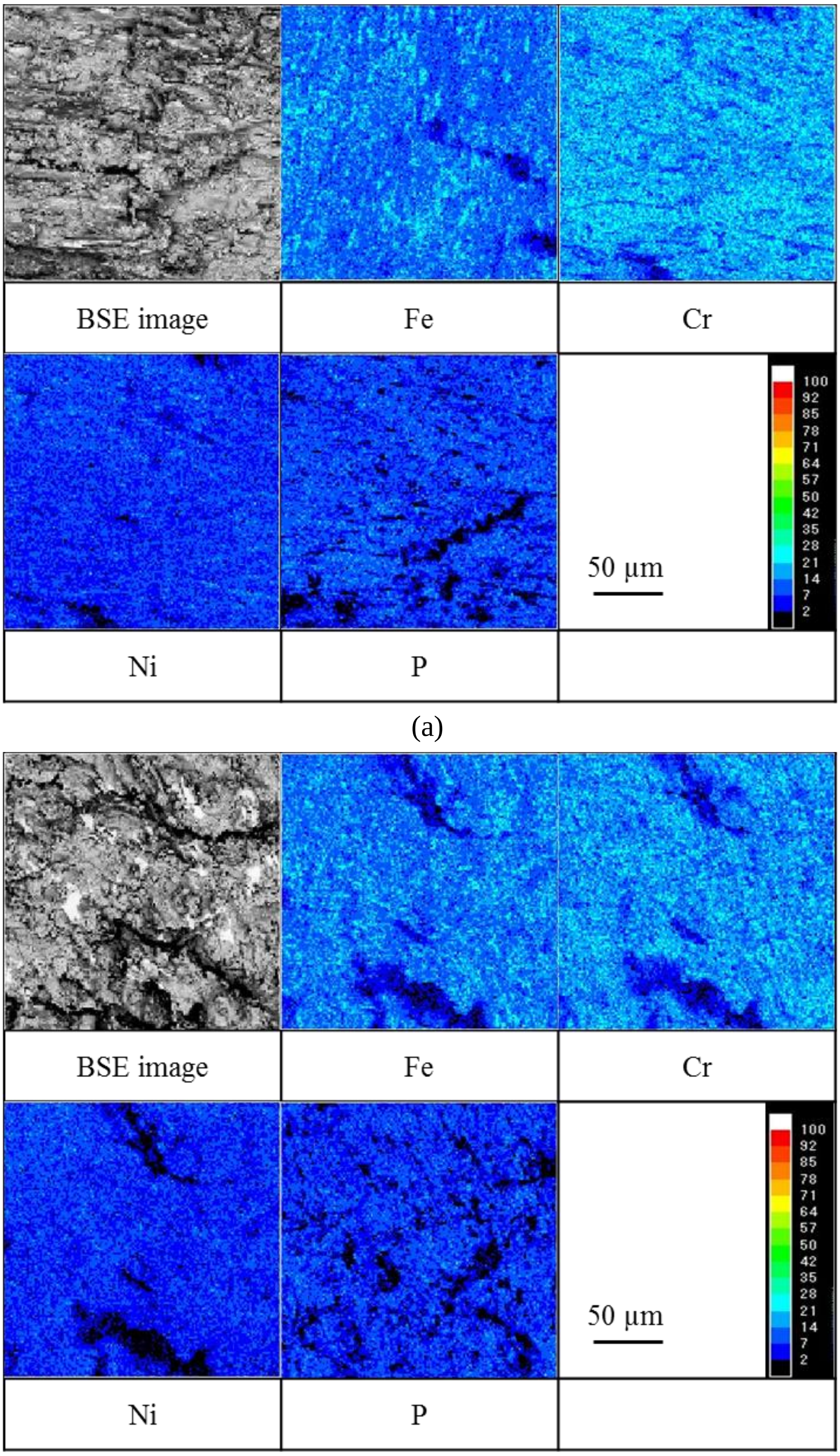

(a)

(b)

Fig. 3.3.11 EPMA mapping analysis results for both fracture surfaces of joint brazed with Fe-20Cr-43Ni-10P filler metal after shear strength test in clearance of 200 μm. (a) one side, (b) other side.

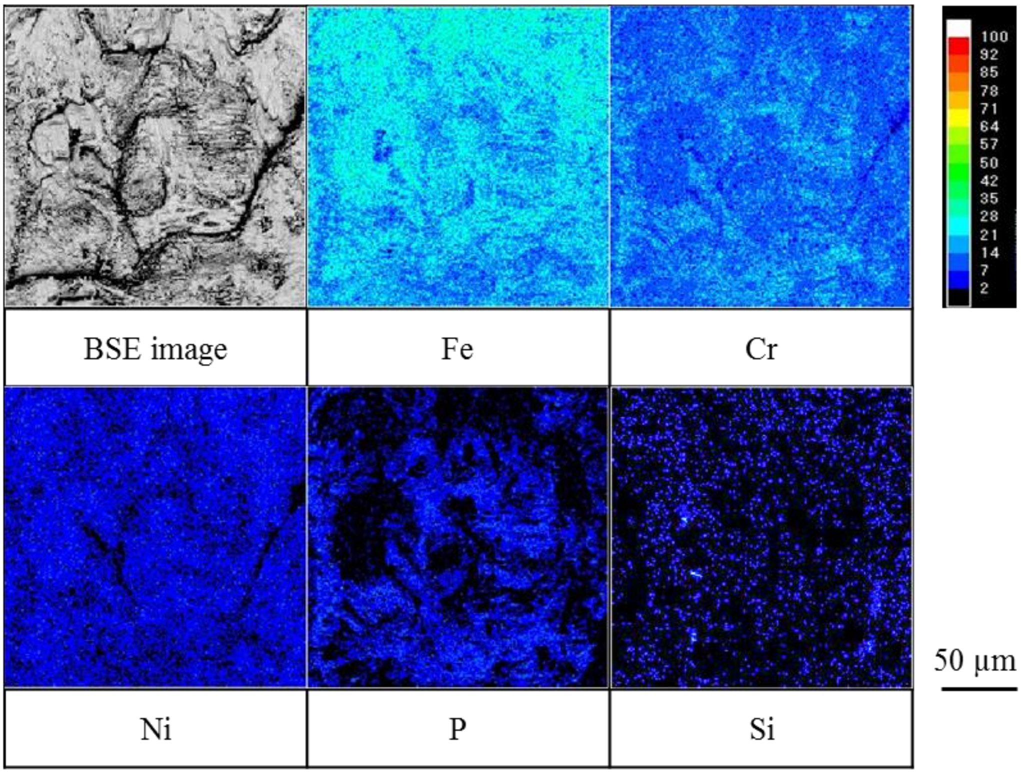

(a)

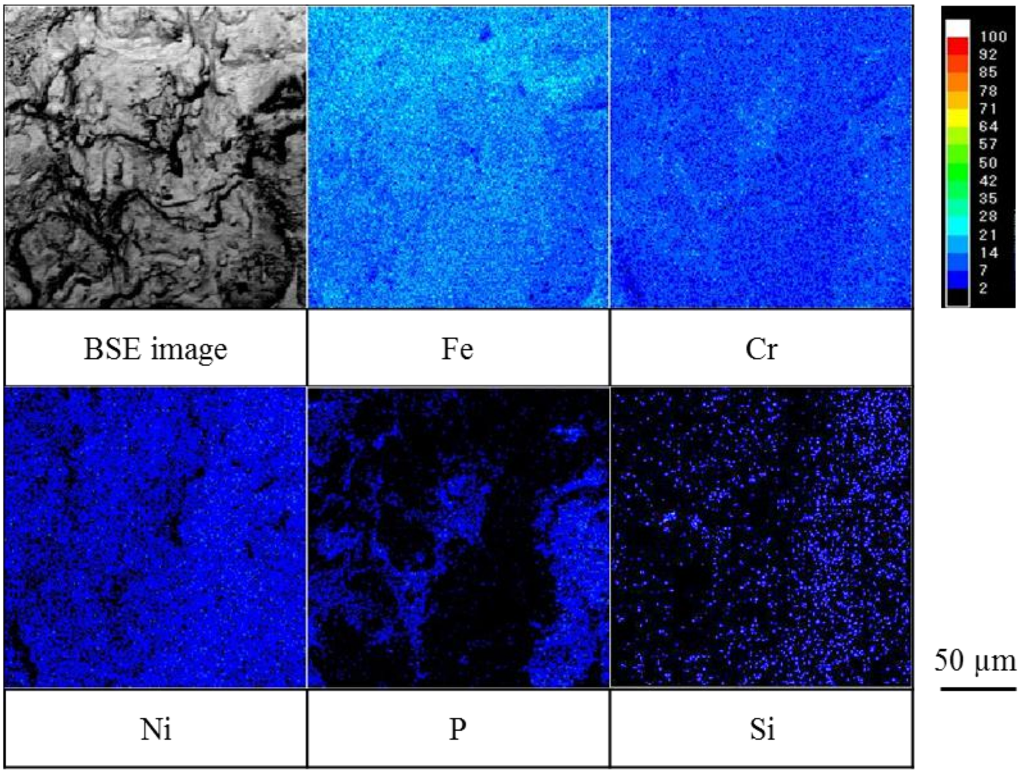

(b)

Fig. 3.3.12 EPMA mapping analysis results for both fracture surfaces of joint brazed with Fe-20Cr-20Ni-8P-5Si-2Mo filler metal after shear strength test in clearance of 10 μm. (a) one side, (b) other side.

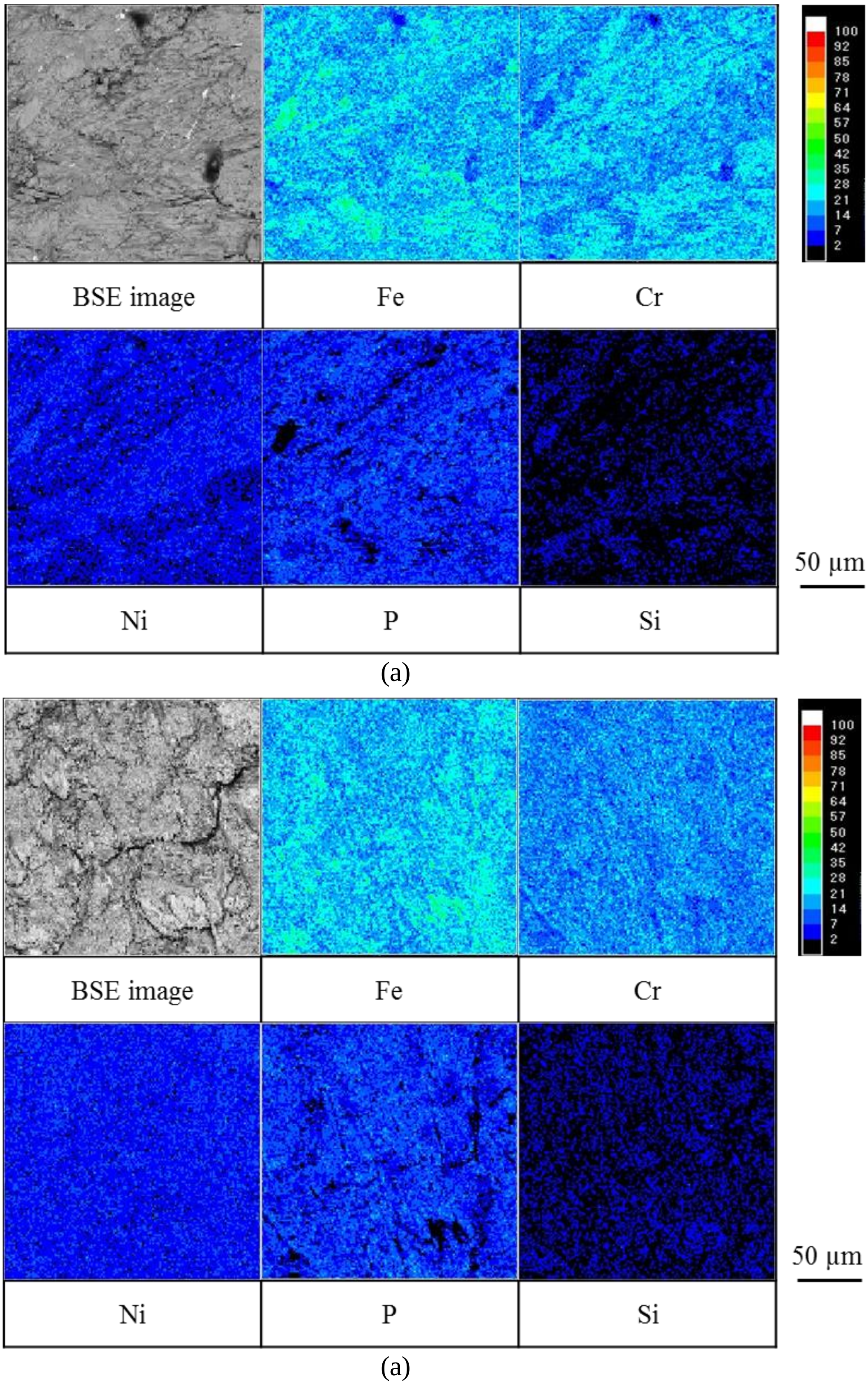

Fig. 3.3.13 EPMA mapping analysis results for both fracture surfaces of joint brazed with Fe-20Cr-20Ni-8P-5Si-2Mo filler metal after shear strength test in clearance of 50 µm. (a) one side, (b) other side.

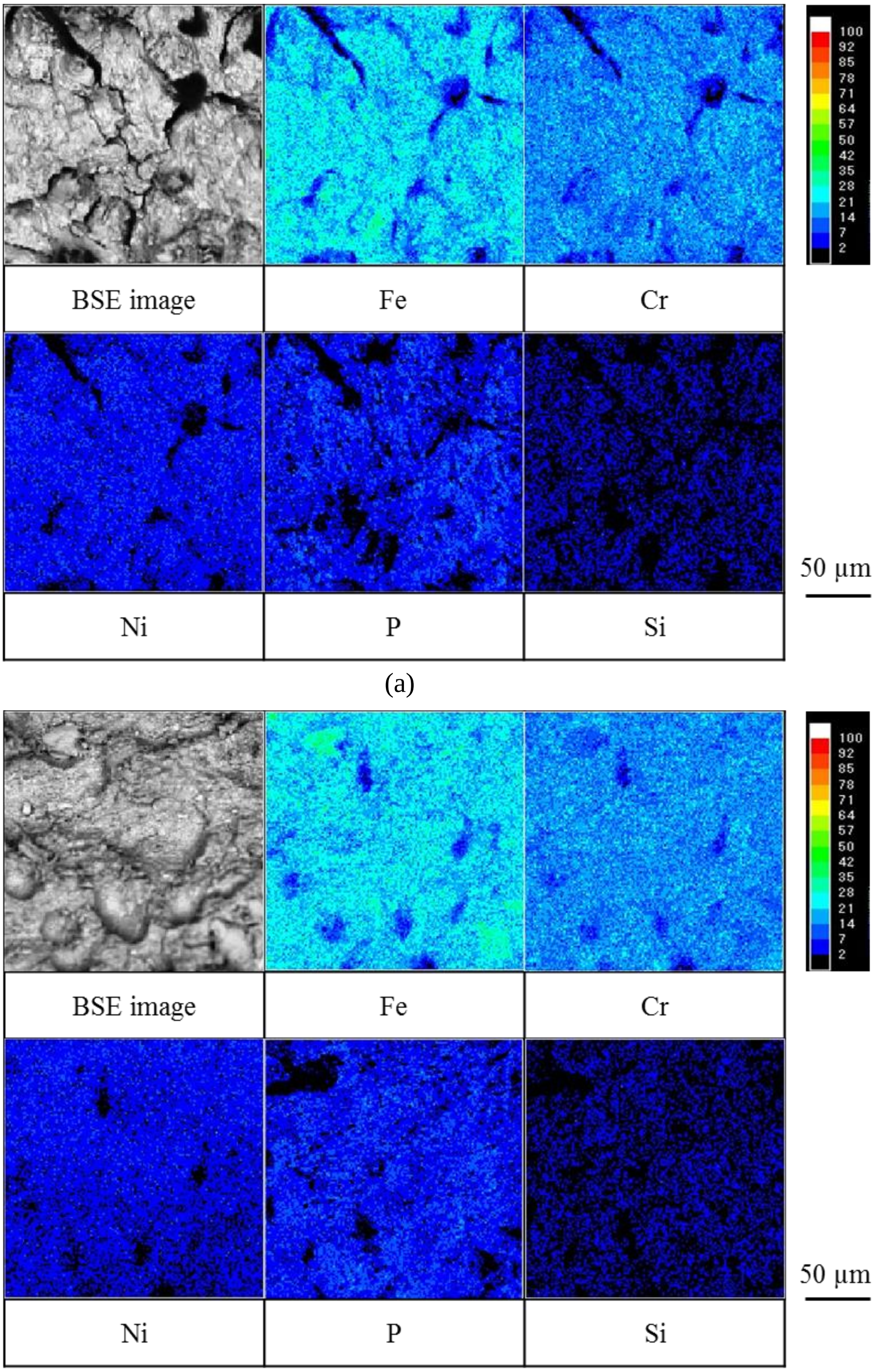

(a)

(a)

Fig. 3.3.14 EPMA mapping analysis results for both fracture surfaces of joint brazed with Fe-20Cr-20Ni-8P-5Si-2Mo filler metal after shear strength test in clearance of 200 μm. (a) one side, (b) other side.

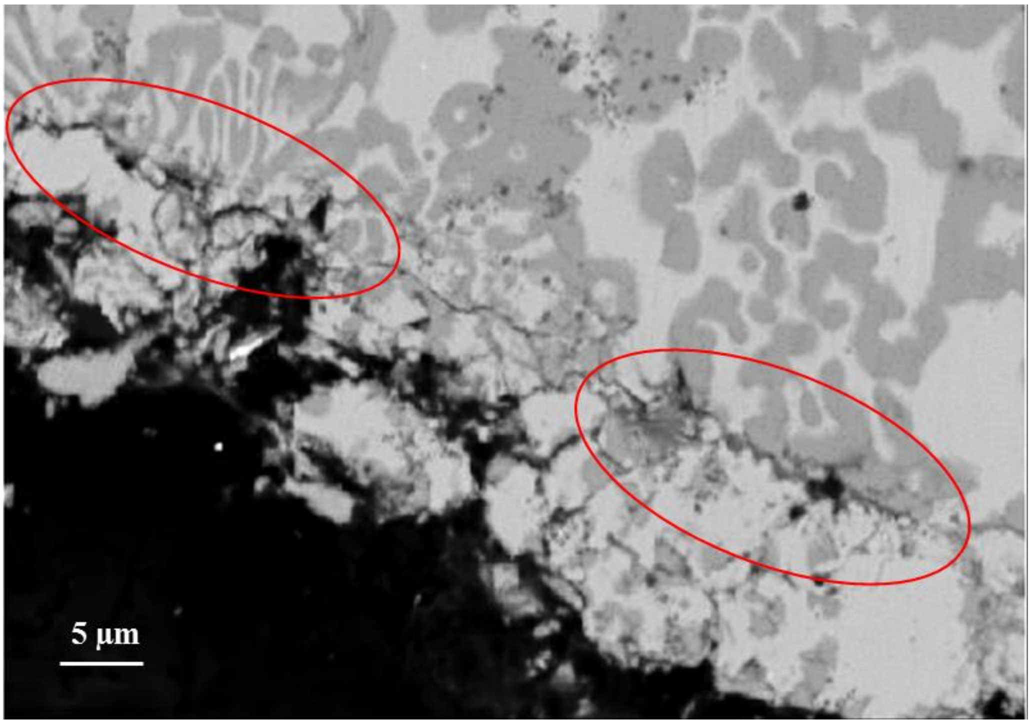

Fig. 3.3.15 Microstructure of cross-section of finally solidified region of joint brazed with Fe-20Cr-43Ni-10P filler metal in the clearance of 300 μm after shear strength test (back-scattered electron image).

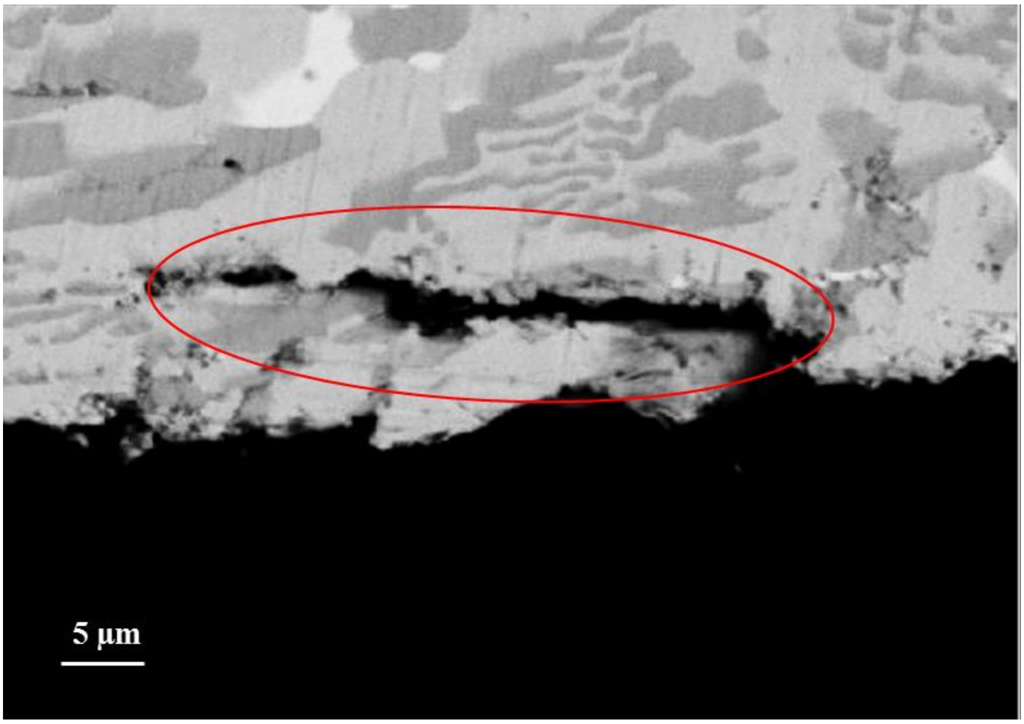

Fig. 3.3.16 Microstructure of cross-section of finally solidified region of joint brazed with Fe-20Cr-20Ni-8P-5Si-2Mo filler metal in the clearance of 100 μm after shear strength test (back-scattered electron image).

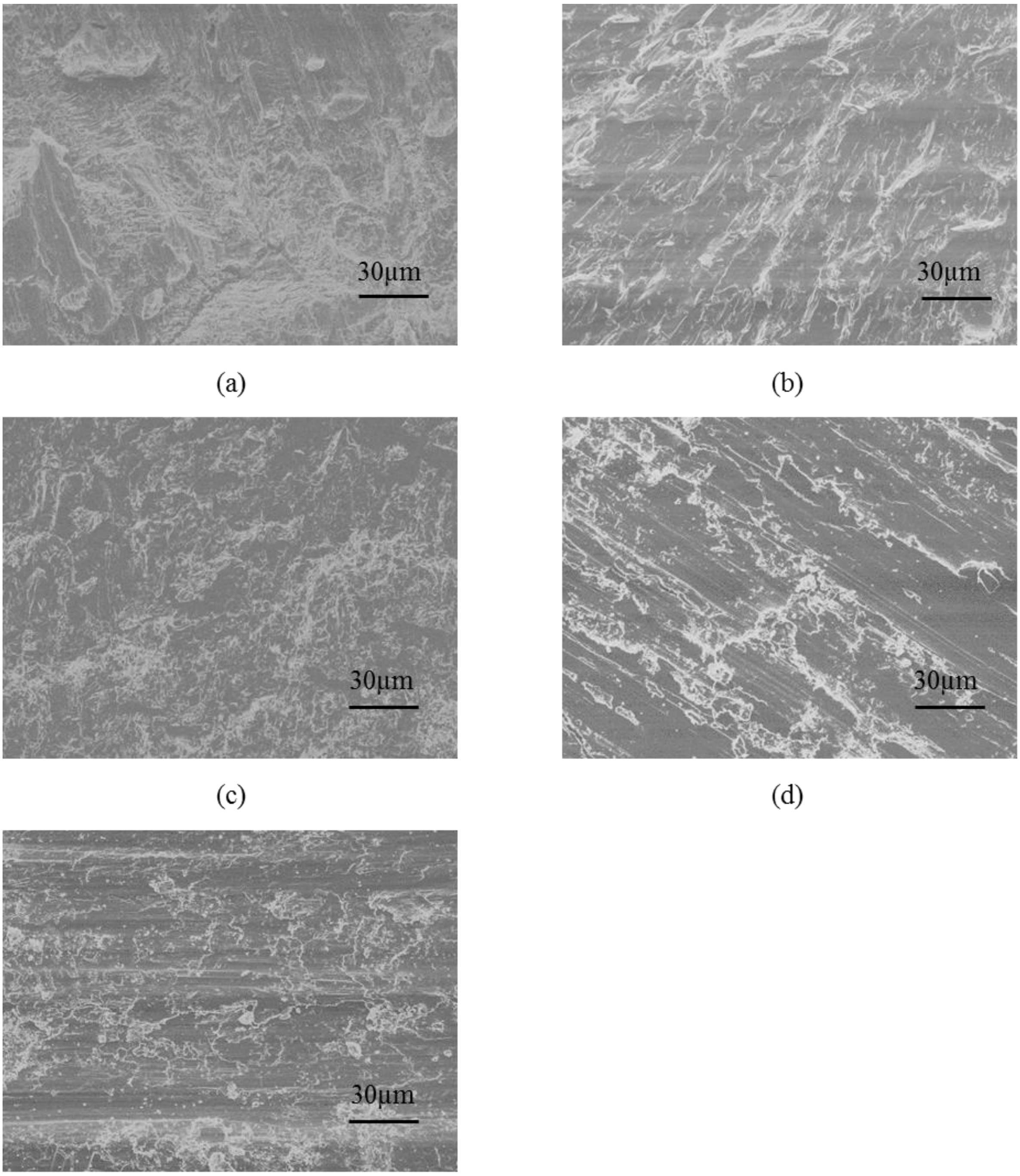

(a) (b) (c) (d) (e)

Fig. 3.3.17 Fractographs of joints brazed with Fe-20Cr-43Ni-10P filler metal after shear strength test in clearances of (a) 10 μm, (b) 50 μm, (c) 100 μm, (d) 200 μm and (d) 300 μm.

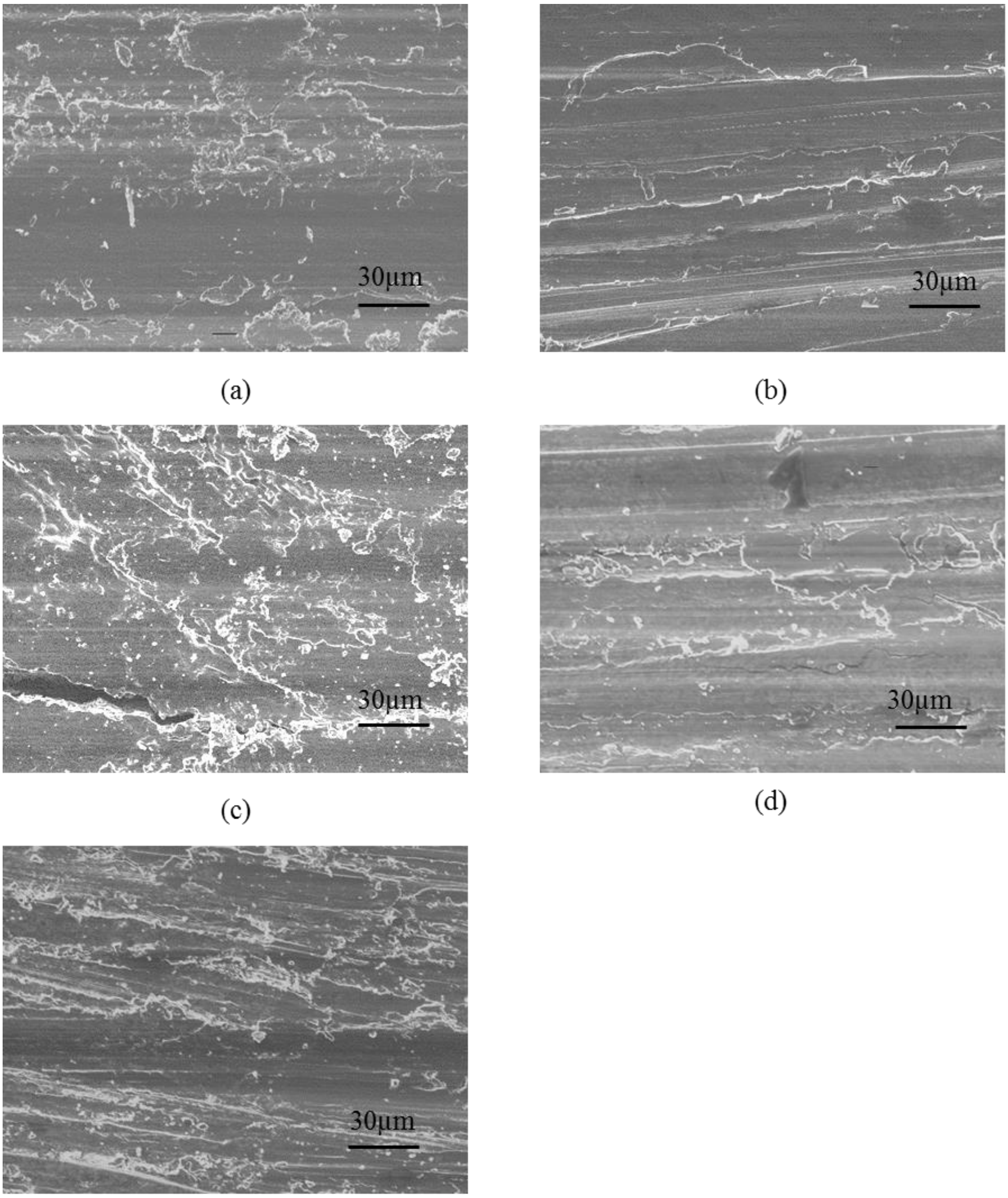

(a) (b) (c) (d) (e)

Fig. 3.3.18 Fractographs of joints brazed with Fe-20Cr-20Ni-8P-5Si-2Mo filler metal after shear strength test in clearances of (a) 10 μm, (b) 50 μm, (c) 100 μm, (d) 200 μm and (d) 300 μm.

Table 3.3.8 Vickers hardness of phases in joints with Fe-20Cr-43Ni-10P.

| Analysis area | Vickers hardness (HV) | | | |
|---|---|---|---|---|
| | Clearance 10 µm | Clearance 50 µm | Clearance 100 µm | Clearance 200 µm |
| SUS304 | 150.2 | - | - | - |
| Diffusion region | 185.3 | - | - | - |
| Brazed layer | 308.2 | - | - | - |
| Primary crystal | - | 170.1 | 199.1 | 171.5 |
| Final solidified region | - | 403.1 | 388.8 | 357.6 |

Table 3.3.9 Vickers hardness of phases in joints with Fe-20Cr-20Ni-8P-5Si-2Mo.

| Analysis area | Vickers hardness (HV) | | | |
|---|---|---|---|---|
| | Clearance 10 µm | Clearance 50 µm | Clearance 100 µm | Clearance 200 µm |
| SUS304 | 151.3 | - | - | - |
| Diffusion region | 190.8 | - | - | - |
| Brazed layer | 266.1 | - | - | - |
| Primary crystal | - | 167.4 | 182.8 | 176.5 |
| Final solidified region | - | 404.1 | 364.9 | 402.2 |

### 3.3.4 Effect of joint clearance on shear strength

As shown in Fig. 3.3.2 (a) and Fig. 3.3.4 (a), when the clearance is 10 μm, P added in the brazing filler metal is concentrated in the whole brazed layer so that the brazed layer has much higher hardness than the adjacent diffusion region. On the other hand, when the joint clearance is more than 50 μm, the final solidified region appeared in the brazed layer. The added P is segregated and enriched in the final solidified region so that a phosphide phase generates with the higher P content. The phosphide phase aroused large hardness of the final solidified region, resulting in crack initiation and propagation in the final solidified region adjacent to the primary crystal [24, 25].

As shown in Table 3.3.3 and 3.3.6, compared with Table 3.3.2 and 3.3.5 respectively, the P content in the phosphide phase does not continue to increase significantly with the clearance in the clearance of 200 μm, and the component of the phosphide phase is almost to be constant. Back-scattered electron images of the finally solidified regions of Fe-Cr-based filler metals in the clearances of 50 μm, 100 μm and 200 μm are shown in Fig. 3.3.19 and 3.3.20. Based on the images, the area ratios occupied by the phosphide phases in various clearances were calculated with an image analysis software (Image-Pro Insight). The results are shown in Table 3.3.10 and Table 3.3.11. The corresponding hardness value shown in Table 3.3.8 and Table 3.3.9 are also presented in Table 3.3.10 and Table 3.3.11, respectively.

For Fe-20Cr-43Ni-10P, the area ratio occupied by the phosphide phase drops with the increase of the clearance. Corresponded with the decrease of the phosphide phases, a gradual improvement is observed in the shear strength shown in Fig. 3.3.6. It is believed that reduction of the brittle phosphide phases will leads to an increase in the strength of the joint.

In the case of Fe-20Cr-20Ni-8P-5Si-2Mo, the area ratio occupied by the phosphide phase is the lowest in the clearance of 100 μm. Compared with the shear strength, the smaller the phosphide phase area ratio, the higher the shear strength tends to be.

Therefore, the variation of the joint strength with the brazing clearance is well correlated with the microstructural evolution of the joints, especially the quantity of the phosphide phases. As shown in Table 3.3.10 and Table 3.3.11, along with this decrease of the phosphide phases, Vickers hardness of the finally solidified regions decreases, and the shear strengths shown in Fig. 3.3.6 increased. To improve the strength of the joint, it is effective to suppress the generation of the brittle phosphide phase.

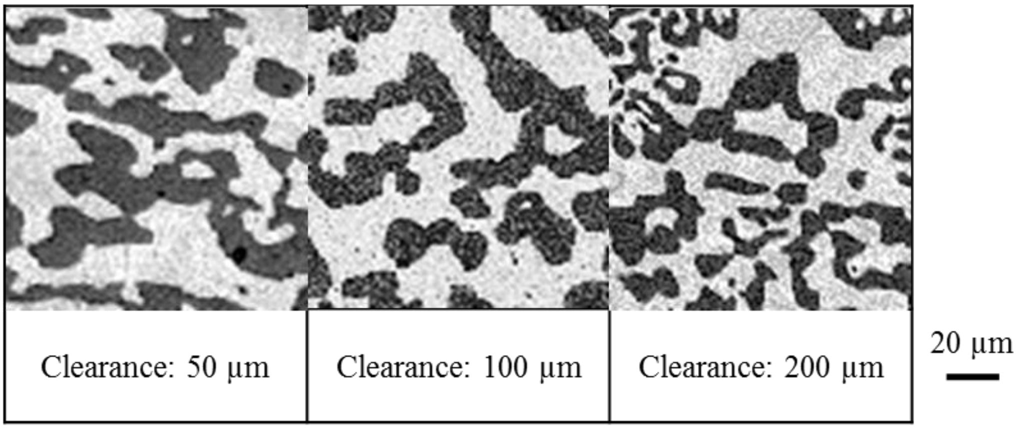

Clearance: 50 µm | Clearance: 100 µm | Clearance: 200 µm

Fig. 3.3.19 Microstructures of finally solidified regions of Fe-20Cr-43Ni-10P filler metal with various clearances (back-scattered electron images).

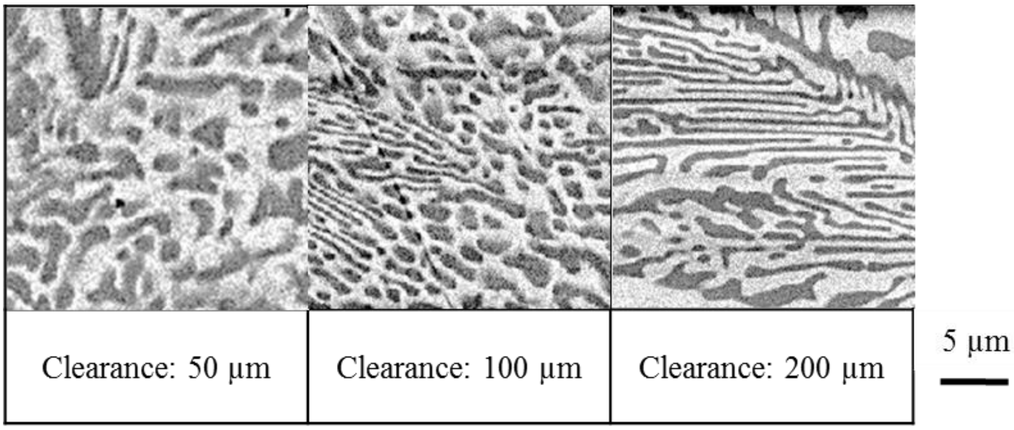

Clearance: 50 µm | Clearance: 100 µm | Clearance: 200 µm

Fig. 3.3.20 Microstructures of finally solidified regions of Fe-20Cr-20Ni-8P-5Si-2Mo filler metal with various clearances (back-scattered electron images).

Table 3.3.10 Volume fractions of phosphide phases and Vickers hardness in finally solidified regions of Fe-20Cr-43Ni-10P filler metal in various clearances.

| Clearance (μm) | 50 | 100 | 200 |
|---|---|---|---|
| Volume fraction of phosphide phase (%) | 55.3 | 51.5 | 48.9 |
| Vickers hardness (HV) | 403.1 | 388.8 | 357.6 |

Table 3.3.11 Volume fractions of phosphide phases and Vickers hardness in finally solidified regions of Fe-20Cr-20Ni-8P-5Si-2Mo filler metal in various clearances.

| Clearance (μm) | 50 | 100 | 200 |
|---|---|---|---|
| Volume fraction of phosphide phase (%) | 55.3 | 47.1 | 49.6 |
| Vickers hardness (HV) | 404.1 | 364.9 | 402.2 |

## 3.4 Conclusions

SUS304 joints brazed with the Fe-Cr-based brazing filler metals in various clearances were prepared, and shear strength and microstructures of them were investigated at room temperature. For comparison, similar experiments were carried out for the existing Ni-based brazing filler metal as well, the results are summarized as follows.

1) In the clearance of 10 μm, owing to the diffusion of Ni or Ni and Si from the brazed layer to the base material for the joints brazed with Fe-20Cr-43Ni-10P and Fe-20Cr-20Ni-8P-5Si-2Mo, respectively, the diffusion region occurred. At the same time, P and Cr added in the brazing filler metal were concentrated in the whole brazed layer so that the brazed layer has a larger hardness than the adjacent diffusion region. Fracture occurred in the interface of the diffusion region and the brazed layer.

2) In the clearance of more than 50 μm, the primary crystal and final solidified region emerged in the brazed layers for the joints with Fe-20Cr-43Ni-10P and Fe-20Cr-20Ni-8P-5Si-2Mo. P and Cr added in the brazing filler metal were segregated and enriched in the final solidified region so that the phosphide phase with high hardness generated. The primary phase is a solid solution phase and the final solidification region consists of a solid solution phase and phosphide phase. The phosphide phase arouses much larger hardness of the final solidified region than the primary crystal so that cracks occur. At the same time, the phosphide phase results in uneven distribution of hardness in the final solidified region. The cracks process along the interface of the solid-solution phase and phosphide phase in the finally solidified region. The fracture occured in the interface of the solid-solution phase and phosphide phase of the final solidified region adjacent to the primary crystal.

3) For every brazing filler metals, the shear strength reaches a maximum value in the clearance of 10 μm. Shear strength is up to 124 MPa, 137 MPa and 174 MPa for Fe-20Cr-43Ni-10P, Fe-20Cr-20Ni-8P-5Si-2Mo and Ni-29Cr-6P-4Si, respectively. When the clearance is more than 50 μm, compared with the clearance of 10 μm, the shear strength decreases and fluctuates in a tight range of approximately 10 MPa. Joints brazed with Fe-20Cr-43Ni-10P has a strength of approximately 100 MPa although the shear strength is slightly inferior to that of the joint with Ni-based filler metal in every clearance. On the other hand, the joint brazed with the Fe-

20Cr-20Ni-8P-5Si-2Mo exhibits comparable shear strength with that brazed with Ni-base brazing filler metal when the clearance is less than 200 μm.

4) Along with the increase of the clearance, the change in the chemical compositions of the phosphide phase is negligible. In contrast, the volume ratio of the phosphide phase is changed with the clearance. A tendency is confirmed that shear strength increases with the decrease of volume fraction of the phosphide phase. The generation of the phosphide phase is the important factor that the shear strength of the joint decreases.

References

[1] T. Watanabe, K. Wakatsuki, A. Yanagisawa and T. Sasaki: Quarterly Journal of the Japan Welding Society, **29** (2011) 241-247.

[2] X.W. Wu, R.S. Chandel, H.P. Seow and H. Li: Journal of Materals Processing Technology, **113** (2001) 215-221.

[3] Y.N. Lia, M.I. Osendi and P. Miranzo: Journal of the American Ceramic Society, **86** (2003) 1226–1229.

[4] G. Dehm, B. Medres, L. Shepeleva, C. Scheu, M. Bamberger, B.L. Mordike, S. Mordike, G. Ryk, G. Halperin and I. Etsion: Wear, **18** (1999) 225–229.

[5] C.Y. Su, C.P. Chou, W.J. Chang and M.H. Liu: Journal of Materials Engineering and Performance, **9** (2000) 663-668.

[6] I.W. Donald and H.A. Davies: Journal of Materials Science, **15** (1980) 2754-2760.

[7] F. Fernandes, B. Lopes, A. Cavaleiro, A. Ramalho and A. Loureiro: Surface and Coatings Technology, **205** (2011) 4094–4106.

[8] G.Q. Xie, D.V. Louzguine-Luzgina, H. Kimura and A. Inoue: Intermetallics, **18** (2010) 851-858.

[9] A. Rabinkin, E. Wenski and A. Ribaudo: Welding Research Supplement, **2** (1998) 66-75.

[10] W.S. Chen and R.K.Shiue: ISIJ International, **52** (2012) 939–941.

[11] R.K. Roya, A.K. Panda, S.K. Das, Govind and A. Mitra: Materials Science and Engineering A, **523** (2009) 312-315.

[12] X.W. Wu, R.S. Chandel, H. Li, H.P. Seow and S.C. Wu: Journal of Materials Processing Technology, **104** (2000) 34-43.

[13] N. Wu, Y.J. Li, J. Wang and U.A. Puchkov: Journal of Materials Processing Technology, **212** (2012) 794-800.

[14] Y. Hisamori: Quarterly Journal of the Japan Welding Society, **10** (1992) 211-216.

[15] C.L. Ou, D.W. Liaw, Y.C. Du and R.K. Shiue: Journal of Materials Science, **41** (2006) 6353–6361.

[16] C.L. Ou and R.K. Shiue: Journal of Materials Science, **38** (2003) 2337-2346.

[17] K. Matsu: Proceedings of International Symposium on Interfacial Joining and Surface Technology Solid State Joining, Brazing and Soldering, Surface Treatment, Advanced Packaging, (2013) 17-18.

[18] N.R. Philips, C.G. Levi and A.G. Evans: Metallurgical and Materials Transactions, **39**A

(2008) 142-149.

[19] F.Z. Wang, Q.Z. Wang, B.H. Yu, B.L. Xiao and Z.Y. Ma: Journal of Materials Processing Technology **211** (2011) 1804-1809.

[20] X.J. Yuan, C.Y. Kang and M.B. Kim: Materials Characterization, **60** (2009) 923-931.

[21] T. Fujita, T. Yamada and N. Takahashi: Tetsu to Hagane, **61** (1975) 357-370.

[22] K. Hosomi, H. Morimoto and Y. Ashida: Tetsu to Hagane, **74** (1988) 2025-2032.

[23] T. Nakazawa, S. Date, M. Tendo and M. Yamazaki: Tetsu to Hagane, **91** (2005) 670-675.

[24] S. Saito, T. Kayamoto and T. Onzawa: Quarterly Journal of the Japan Welding Society, **17** (1999) 35-40.

[25] S. Saito and T. Onzawa: Quarterly Journal of the Japan Welding Society, **19** (2001) 688-692.

# Chapter 4 Corrosion resistance of SUS304 stainless steel joints brazed with Fe-Cr-based brazing filler metals

## 4.1 Introduction

The main function of an exhaust gas recirculation (EGR) cooler is to transfer heat from engine exhaust to the coolant loop that serves the radiator and the charger air cooler. There are two critical factors related to the reliability and durability of an EGR system: the first one is the process of particulate matter (PM) contained in the exhaust gases. PM are mainly composed of soot and hydrocarbons [1]. Soot and hydrocarbon deposition in the EGR cooler reduces heat transfer efficiency of the cooler and increases emissions and pressure drop across the cooler [2-11]. Fouling caused by soot and hydrocarbon deposition has been always treated as an approximate factor in heat exchanger designs [2].The second one is the presence of water and acid vapors and their condensation on the inside the wall of the EGR tubes and the intake manifold of the engine [1]. The corrosive condensate forms a thin film on the wall of the tubes of the EGR cooler, and will attack the inside of the EGR tubes. Thus, the EGR system is subject to corrosion. This corrosive condensate can cause EGR cooler failure and consequentially result in severe damage to the engine. Therefore, the EGR cooler must be made of corrosion resistant materials.

Corrosion is primarily related to oxides of sulfur and nitrogen in a gas stream, especially problematic when condensation occurs. Exhaust gases consists mainly of $CO_2$, NOx, $SO_2$ and $H_2O$ [12]. As the temperature decreases, these gases form a corrosive condensate comprised of nitric acid, sulphuric acid and organic acids. Nitric and sulphuric acid are highly corrosive, while the organic acids are less corrosive [12].

The sulfuric acid in an exhaust gas is primarily formed by a process describes as follows: oxidation of fuel sulfur during combustion (equation 4.1.1). Gaseous $SO_2$ reacts with oxygen and $SO_3$ forms (equation 4.1.2). $SO_3$ reacts with moisture or water vapor present in the exhaust stream and thus $H_2SO_4$ forms (equation 4.1.3).

$$S + O_2 \rightarrow SO_2 \qquad (4.1.1)$$

$$2SO_2 + O_2 \rightarrow 2SO_3 \qquad (4.1.2)$$

$SO_3 + H_2O \rightarrow H_2SO_4$ (4.1.3)

The nitric acid in the exhaust gas is primarily formed as follows: reacting with atmospheric nitrogen and oxygen forms nitrogen oxides (equation 4.1.4). Nitrogen dioxides may then later react with water and form nitric acid (equation 4.1.5) [9].

$N_2 + O_2 \rightarrow 2\ NO$ (4.1.4)

$4NO + 2H_2O + 3O_2 \rightarrow 4HNO_3$ (4.1.5)

The corrosiveness of the condensate is therefore mainly defined by the type and quality of the fuel used. In the fuel, allowed sulfur levels can vary significantly between certain countries, from 10 ppm up to 2000 ppm [10]. The limit for sulfur was set to 10 ppm for the EU, and 15 ppm for the US regulations [12]. Since 2003, almost all diesel fuels have been the ultra-low sulfur diesel (ULSD) fuel which contains substantially low sulfur content in Europe, and since 2007 ULSD fuel has been avertable in USA. Due to the low sulfur content in ultra-low-sulfur fuels, the exhaust gas and their extracted condensate are the less aggressive in comparison with high sulfur diesel fuels.

The scope of this chapter is to investigate the corrosion properties of SUS304 stainless steel joints brazed with Fe-Cr-based brazing filler metals in high nitrogen exhaust gas condensate. To evaluate the corrosion behavior of the joints, immersion tests in artificial compound solution were performed. The corrosion resistance of the joints was analyzed and compared by means of morphology of corrosion attack, quantitative analysis and penetration depth of corrosion. The mechanism for the change in corrosion resistance was also explored.

## 4.2 Experimental procedure

### 4.2.1 Specimen preparation

Plates of commercial SUS304 stainless steel (thickness: 2 mm) were cut into 50 mm×40 mm chips and subsequently cleaned ultrasonically in acetone before brazing. Chemical compositions and melting properties of the brazing filler metals are the same as that shown in Table 3.2.2. For comparison, the conventional Ni-29Cr-6P-4Si filler metal (mass%) was also prepared. T-specimens shown in Fig. 4.2.1 (a) were fixed with a steel clamp with the clearance of approximately 50 μm and then carefully placed into a semicontinuous vacuum furnace. Brazing was performed at brazing temperature of 1373 K for 30 minutes in a vacuum degree of 50 Pa. The temperature profile of brazing is the same as that shown in Fig. 3.2.2. In this chapter, the fillet area was defined as a region where the fillet was formed, and the brazed layer was defined as the junction region between both of SUS304 stainless steel in the T-specimen.

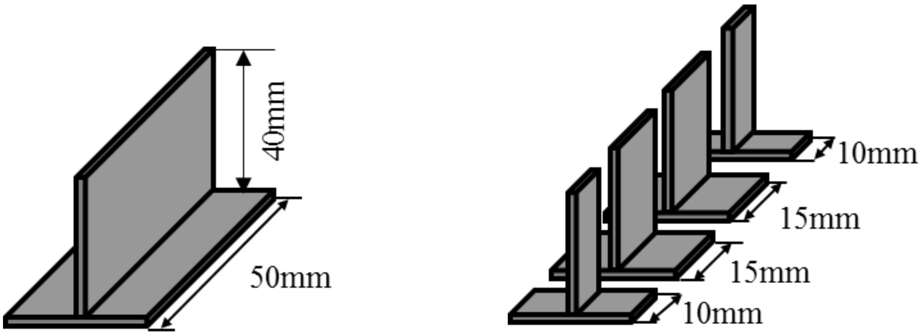

(a) (b)

Fig. 4.2.1 Schematic diagram of specimen.

(a) T-specimens for immersion test,

(b) cut T-specimens shown in (a) for microstructure analyses.

### 4.2.2 Immersion test

The immersion test of brazed joints was conducted at the room temperature in a compound aqueous solution shown in 2.2.1. The compound aqueous solution was made as follows: 1650 mg NaCl, 3.4 ml nitric acid (60%) and 1.4 ml sulphuric acid (98.08%) were added into 500 ml $H_2O$, and then $H_2O$ was added to form 1000 ml aqueous solution. The pH value of the solution is 1.0 by pH test paper (accuracy class 0.3). Before immersion, the specimens were cleaned ultrasonically in acetone for 10 min, washed using distilled water, dried in hot air and then entirely exposed in 350 ml test solutions for 50 h, 100 h, 200 h and 300 h respectively. During the test, the solutions were changed every 36 h, and the pH value of the solution was measured and documented before and after the change of the solution. After the immersion test, the corroded specimens were removed from the solutions, cleaned with distilled water, dried with hot air and then cut off according to Fig. 4.2.1 (b). The morphology after corrosion was observed. The maximum penetration depth was measured with a software accompanied by an electron probe X-ray microanalyzer (EPMA).

In addition, a SUS304 stainless steel chip shown in 4.2.1 was abraded in a #800 grit emery paper and immersed continuously for 500 h at the room temperature in the above compound aqueous solution to observe surface morphology.

### 4.2.3 Microstructure analysis

The specimens after the immersion test were cut out according to Fig. 4.2.1 (b) and central two parts were used for microstructure analyses. The specimens used for microstructure analyses before and after the immersion test were abraded with #100, #400, #800, #1200, #2400 and #4000 grit emery papers and then polished by 1.0 μm aluminum suspension. The microstructures of cross-sections of fillet areas before and after the immersion test were analyzed using an EPMA. The microstructures of the surfaces of stainless steels after the immersion test were analyzed using a charge-coupled device (CCD) scope.

## 4.3 Results and discussion

### 4.3.1 Self-passivation characteristic of SUS304 stainless steel

When two or more metals or dissimilar alloys come into contact and exposed to a conducting corrosive environment, the potential difference leads to a flow of electric current between them and the corrosion is stimulated for the active metal acting as an anode. The corrosion phenomenon is called the galvanic corrosion [13-17]. In a joint, a brazing filler metal and matrix metal having different corrosion potentials are brazed in contact, causing possibly the galvanic corrosion.

SUS304 stainless steel is widely used due to a combination of good mechanical properties and excellent corrosion resistance over a large temperature range [18]. Stainless steel is superior in corrosion resistance because it has a passivation film on the surface of steel. The passivation film is usually duplex, which is composed of an outer iron and chromium oxy-hydroxide layer and an inner compact layer formed by chromium oxide [19]. Although this passivation film is susceptible to localized pitting corrosion caused by aggressive anions such as chloride ion, which can rapidly lead to the damage or failure of structural components [19-27], this passivation film is self-repaired soon in oxidation atmosphere when it has some damage. This is a superior structure in corrosion resistance. As shown in Fig. 2.3.7, self-passivation characteristic is particularly apparent for SUS304 stainless steel in the case of the experimental electrolyte. In this section, it will be conformed whether or not SUS304 stainless steel has self-passivation characteristic in the electrolyte in this study by surface morphology analyses.

A commercial SUS304 stainless steel chip was abraded with a #800 grit emery paper and the surface morphology is shown in Fig. 4.3.1(a). The surface morphology of SUS304 after the potentiodynamic potential polarization test (shown in 2.3.4) and immersion test for 500 h at the room temperature are shown in Fig. 4.3.1(c) and Fig. 4.3.1(e), respectively. Compared with the commercial SUS304 stainless steel, pits are observed in both polarized SUS304 and immersed SUS304. As shown in Fig. 4.3.1(c), it is clear for the polarized SUS304 stainless steel that the pits are the result of the pitting corrosion during the anodic polarization test. To determine the formation mechanism of the pits in the immersed SUS304 stainless steel, mapping analysis was performed and the results are shown in Fig. 4.3.2. Fe, Cr and Ni were corroded in the pits in both specimens. It is confirmed the pits occurred as the result of pitting corrosion as well in the immersed SUS304. It is well-known for stainless steels that pitting corrosion is connected with the formation of a passivation film. Occurrence of pitting corrosion implies that a passivation film has formed on the surface of the immersed SUS304. In others words, SUS304 forms a passivation film in the experimental electrolyte. The surface morphology analysis result corresponds with the result of the electrochemical measurement (shown in Fig. 2.3.7). Therefore, the galvanic corrosion doesn’t occur between SUS304 stainless steels and the Fe-Cr-based filler metals in SUS304 stainless steel joints due to the presence of the passivation film in this study. However, the pitting corrosion of SUS304 stainless steels should be payed close attention to.

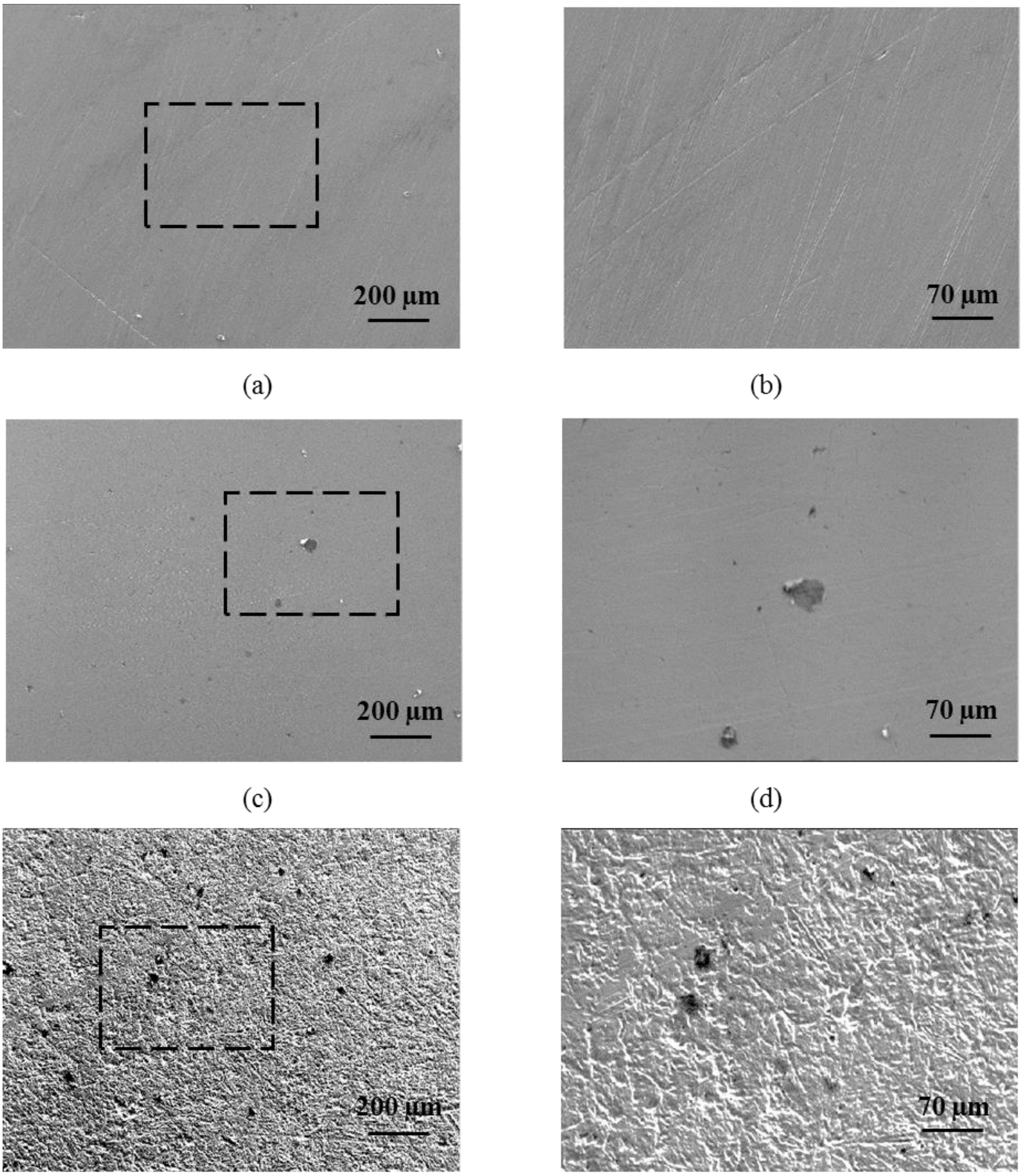

(a) (b)

(c) (d)

(e) (f)

Fig. 4.3.1 Morphologies of surfaces of SUS304 stainless steel chips (secondary electron images).

(a) before immersion test, (b) magnified image of dotted area shown in (a),

(c) after polarization test shown in 2.3.4, (d) magnified image of dotted area shown in (c),

(e) after immersion test for 500 h, (f) magnified image of dotted area shown in (e).

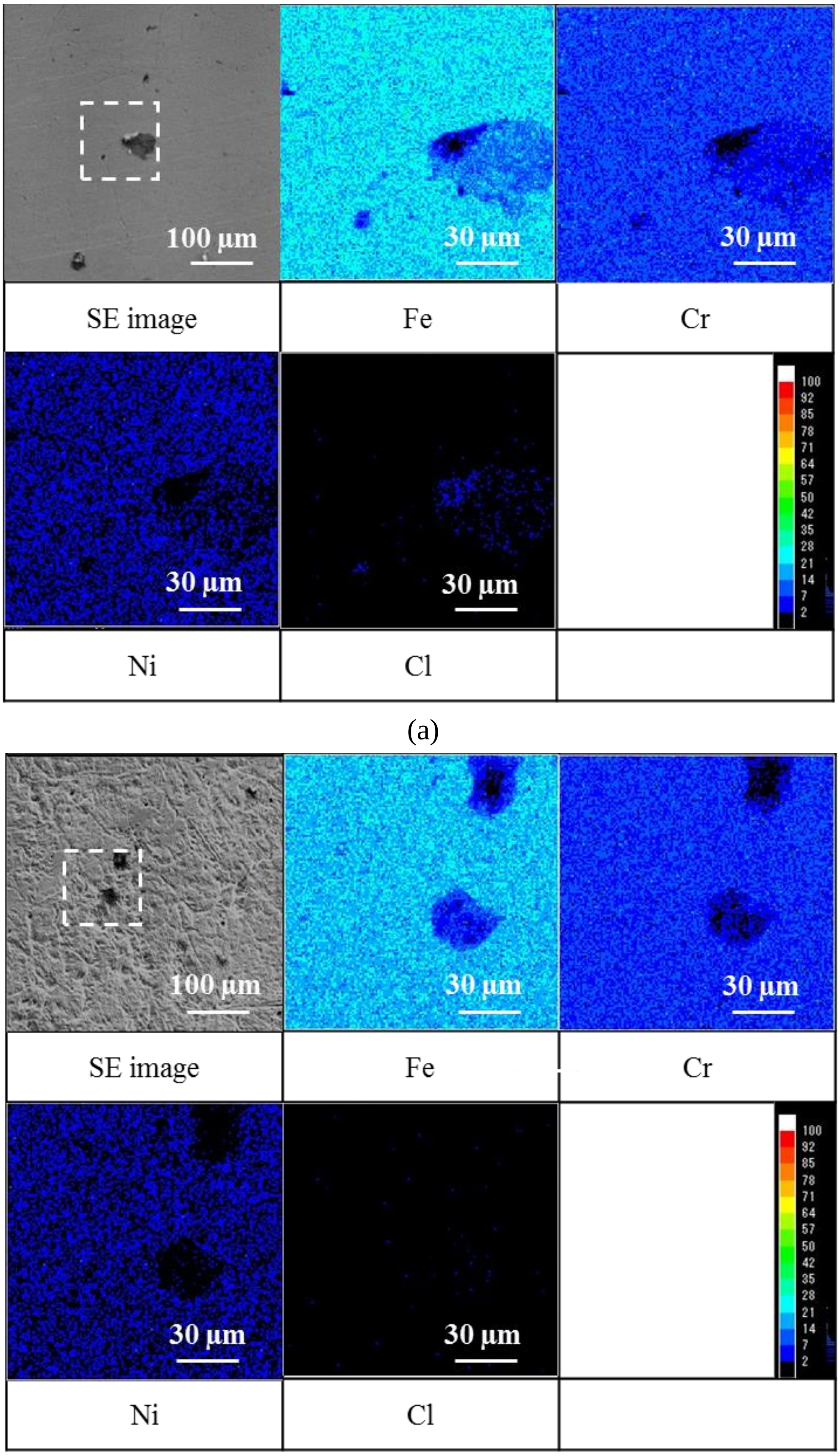

(a)

(b)

Fig. 4.3.2 Mapping analysis results for surfaces of SUS304 stainless steel. (a) after polarization test shown in 2.3.4, (b) after immersion test for 500 h.

### 4.3.2 Microstructure characterization of fillet area before immersion test

The microstructure of the fillet area of a joint brazed with Fe-20Cr-43Ni-10P is shown in Fig. 4.3.3 (a). A primary crystal and the final solidified region are observed. The final solidified region is composed of a dark gray phase and bright gray phase. The mapping analysis results for the joint with Fe-20Cr-43Ni-10P are shown in Fig. 4.3.4 (a). Each element is unevenly distributed in the primary crystal or the final solidified region, and P is to be segregated in the dark gray part of the final solidified region. From the quantitative analysis results (shown in Table 4.3.1) of the formation phases, the ratio of Fe: Cr: Ni: P in the primary crystal is 42.7: 17.8: 38.9: 0.6 (mass%), the content of P is significantly reduced in comparison with Fe-20Cr-43Ni-10P. The ratio of Fe: Cr: Ni: P in the bright gray phase in the final solidified region is 40.3: 12.7: 46.4: 0.6 (mass%). The content of Cr is much lower than that of the filler metal and the primary crystal. It is confirmed that a Cr-poor phase formed. In the brazed layer (shown in Table 3.3.2), the ratio of Fe: Cr: Ni: P in the primary crystal and the bright gray phase of the final solidified region is 42.7: 17.0: 39.6: 0.7 (mass%) and 45.8: 15.5: 38.1: 0.6 (mass%), respectively. Chemical compositions of the primary crystal in the fillet area are almost the same as those in the brazed layer, but the content of Fe and Cr are lower, and the content of Ni is higher in the bright gray phase of the final solidified region in the fillet area than those in the brazed layer. On the other hand, the ratio of Fe: Cr: Ni: P in the dark gray phase in the final solidification region of the fillet area is 18.4: 37.2: 28.6: 15.8 (mass%), a phosphide phase is formed because of high concentration of P. This will be bound to enhance the brittleness of the joints. In contrast, the ratio of Fe: Cr: Ni: P in the phosphide phase of the brazed layer (shown in Table 3.3.2) is 18.0: 37.4: 24.0: 20.6 (mass%). The P content is lower and the Ni content is higher in the phosphide phase of the fillet area than those of the brazed layer. Those differences are connected with the larger size of the fillet area in comparison with the brazed layer. The larger size of the fillet area makes it difficult for the elements to diffuse towards the interface of SUS304 in the central region of the fillet area and Fe and Ni diffusion between the SUS304 and the brazing filler metal has a small effect on the compositions in the final solidified region. Based on the quantitative analysis results, the primary crystal and the bright gray phase in the final solidified region are Fe-Cr-Ni-based solid-solution phase and the dark gray phase in the final solidified region is a Cr-P-Fe-Ni-based phosphide phase.

The microstructure of the fillet area of a joint brazed with Fe-20Cr-20Ni-8P-5Si-2Mo is shown in Fig. 4.3.3 (b). The microstructure is similar to that brazed with Fe-20Cr-43Ni-10P.

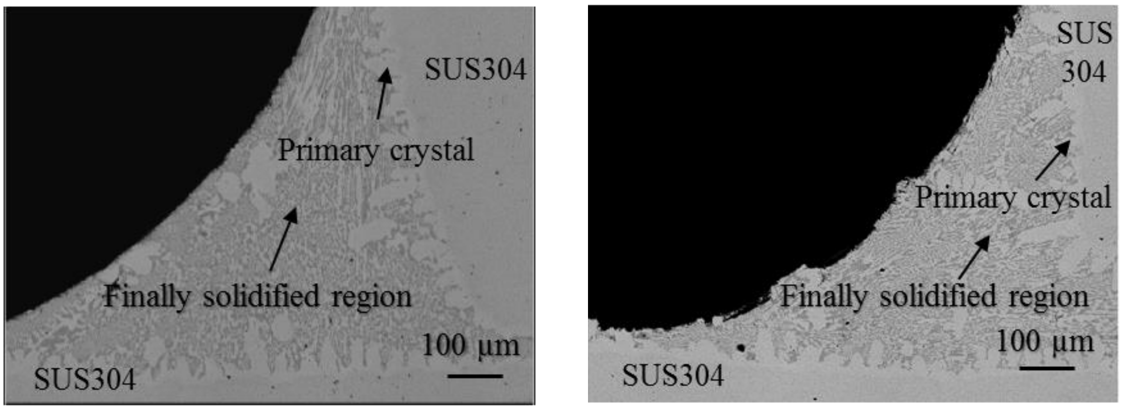

(a) (b)

Fig. 4.3.3 Microstructures of cross sections of fillet areas of joints (back-scattered electron images).
(a) brazed with Fe-20Cr-43Ni-10P filler metal,
(b) brazed with Fe-20Cr-20Ni-8P-5Si-2Mo filler metal.

However, the microstructure of the final solidification region has become finer due to Mo addition [28-30]. The mapping analysis results for the joint with Fe-20Cr-20Ni-8P-5Si-2Mo are shown in Fig. 4.3.4 (b). The almost same results as Fe-20Cr-43Ni-10P are obtained. According to the quantitative analysis results (shown in Table 4.3.2), the ratio of Fe: Cr: Ni: P: Si: Mo in the primary crystal is 63.0: 16.4: 16.5: 0.2: 3.7: 0.2 (mass%). The content of P is also significantly reduced in comparison with Fe-20Cr-20Ni-8P-5Si-2Mo. The ratio of Fe: Cr: Ni: P: Si: Mo in the bright gray phase in the final solidified region is 56.1: 20.3: 19.3: 0.3: 3.7: 0.3 (mass%), and close to that of the primary crystal. Compared with the brazed layer (shown in Table 3.3.5), the ratio of Fe: Cr: Ni: P: Si in the primary crystal and the bright gray phase in the final solidified region of the brazed layer is 64.4: 19.7: 11.8: 0.4: 3.7 (mass%) and 62.4: 19.5: 13.9: 0.2: 4.0 (mass%), respectively. The Fe content is lower and the Ni content is higher in the primary crystal phase and the bright gray phase in the final solidified region of the fillet area than those of the brazed layer. On the other hand, the ratio of Fe: Cr: Ni: P: Si: Mo in the dark gray phase in the final solidification region of the fillet area is 32.5: 38.0: 12.1: 14.6: 1.1: 1.7 (mass%). A phosphide phase is formed as well because of high concentration of P. The ratio of Fe: Cr: Ni: P: Si: Mo in the phosphide phase of the brazed layer is 30.0: 39.1: 7.8: 22.0: 1.1 (mass%). The P content is lower and Ni content is higher in the phosphide phase of the fillet area than those of the brazed layer. These differences are also connected with the larger size of the fillet area in comparison with the brazed layer. The larger size of the fillet area makes it difficult for the elements to diffuse towards the interface of SUS304 in the central region of the fillet area and Fe and Ni diffusion between the SUS304 and the brazing filler metal has a small effect on the compositions in the final solidified region. Based on the quantitative analysis results, it is judged that the primary crystal and the bright gray phase in the final solidified region are Fe-Cr-Ni-Si-based solid-solution phases and the dark gray phase in the final solidified region is a Cr-P-Fe-Ni-Si-based phosphide phase.

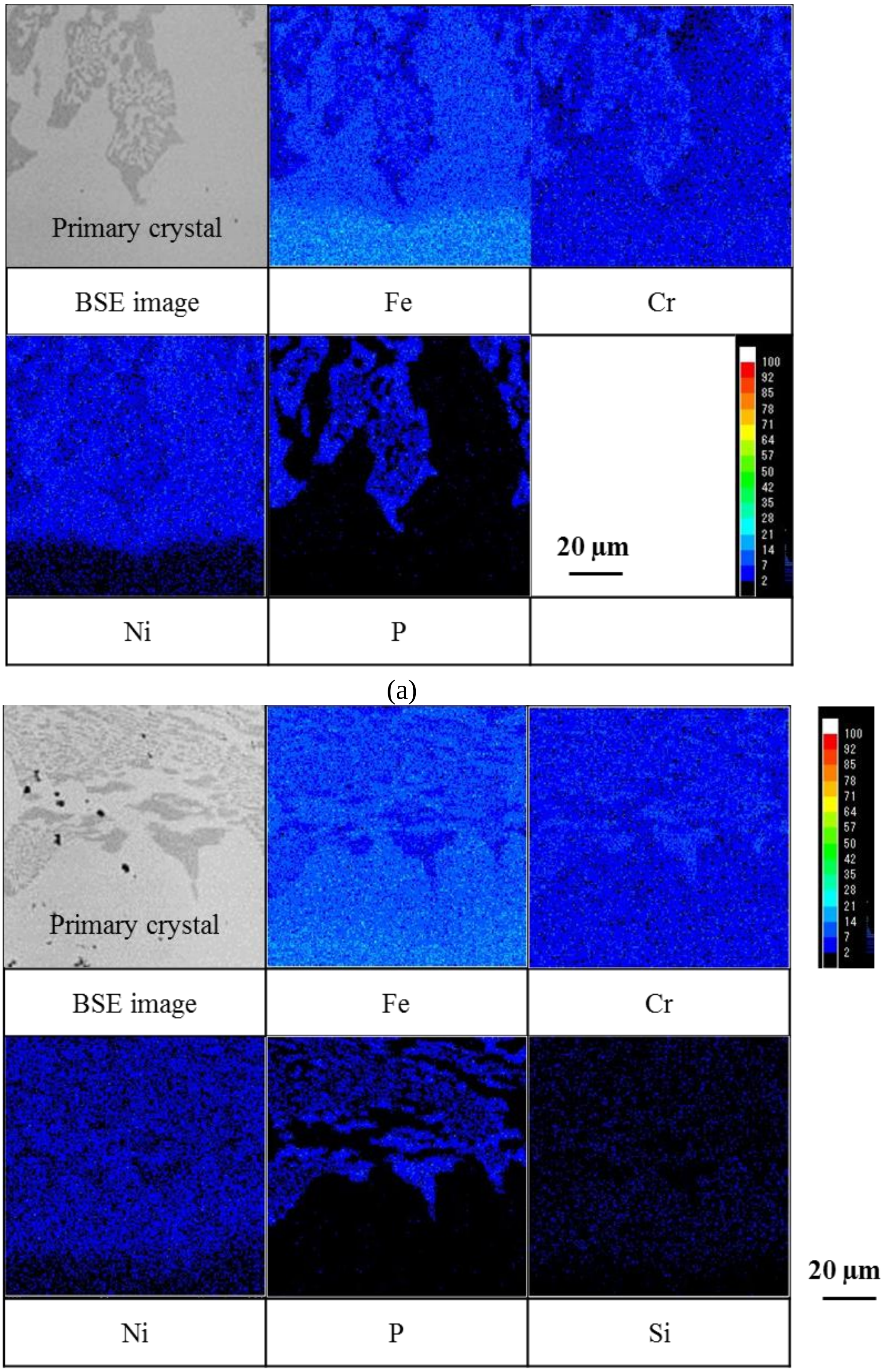

(a)

(b)

Fig. 4.3.4 Mapping analysis results for cross sections of fillet areas of joints.

(a) brazed with Fe-20Cr-43Ni-10P filler metal,

(b) brazed with Fe-20Cr-20Ni-8P-5Si-2Mo filler metal.

Table 4.3.1 Chemical compositions of phases in fillet area of joint brazed with Fe-20Cr-43Ni-10P filler metal.

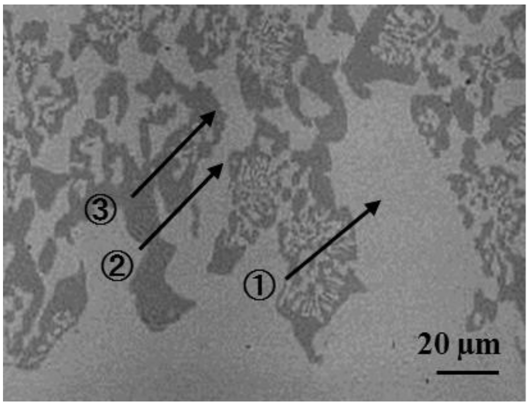

| Analysis | Chemical compositions (mol% / mass%) | | | |
|---|---|---|---|---|
| area | Fe | Cr | Ni | P |
| ① | 42.8/42.7 | 19.2/17.8 | 37.1/38.9 | 0.9/0.6 |
| ② | 40.8/40.3 | 13.8/12.7 | 44.5/46.4 | 0.9/0.6 |
| ③ | 16.2/18.4 | 35.0/37.2 | 23.9/28.6 | 24.9/15.8 |

Table 4.3.2 Chemical compositions of phases in fillet area of joint brazed with Fe-20Cr-20Ni-8P-5Si-2Mo filler metal.

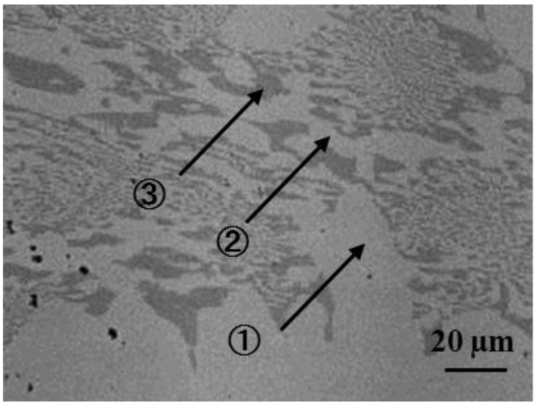

| Analysis | Chemical compositions (mol% / mass%) | | | | | |
|---|---|---|---|---|---|---|
| area | Fe | Cr | Ni | P | Si | Mo |
| ① | 60.5/63.0 | 16.9/16.4 | 15.0/16.5 | 0.4/0.2 | 7.1/3.7 | 0.1/0.2 |
| ② | 53.8/56.1 | 20.8/20.3 | 17.6/19.3 | 0.6/0.3 | 7.1/3.7 | 0.1/0.3 |
| ③ | 28.4/32.5 | 35.7/38.0 | 10.1/12.1 | 23.0/14.6 | 1.9/1.1 | 0.9/1.7 |

### 4.3.3 Corrosion behaviors of SUS304 stainless steel joints

#### 4.3.3.1 Microstructure characterization of fillet area after immersion test

Back-scattered electron images of the cross-sections of the fillet areas after the immersion test are shown in Fig. 4.3.5 and Fig. 4.3.6. It is indicated that corrosion occurred in the final solidified region in the joints brazed with both Fe-20Cr-43Ni-10P and Fe-20Cr-20Ni-8P-5Si-2Mo.

As shown in Fig. 4.3.5 (e), compared with the localized attack of the joints brazed with Fe-20Cr-20Ni-8P-5Si-2Mo, corroded area of Fe-20Cr-43Ni-10P reached the boundary of the primary crystal for immersion time of 300 h. Fig. 4.3.7 shows the morphologies of the cross sections of the primary crystal in the joint brazed with Fe-20Cr-43Ni-10P after the immersion test for 300 h. Fig. 4.3.8 shows mapping analysis results for cross sections of the primary crystal in the joint brazed with Fe-20Cr-43Ni-10 after the immersion test for 300 h. Each element was almost uniformly present in the primary crystal. The quantitative analysis of the primary crystal exposed to solution was performed. As the result, the ratio of Fe: Cr: Ni: P is 42.9: 16.4: 39.9: 0.8 (mass%). Compared with the primary crystal before the immersion test (shown in Table 4.3.1), the components aren’t nearly changed. It is implied that the primary crystal in the joint brazed with Fe-20Cr-43Ni-10P filler is not subject to attacks. The fact is possibly associated with the formation of a passivation film [31].

In the case of Ni-29Cr-6P-4Si, the morphologies of the cross sections of the fillet areas of the joints are shown in Fig. 4.3.9. As shown in Fig. 4.3.9 (a), the microstructure of the fillet area of the joint brazed with Ni-29Cr-6P-4Si is similar to those brazed with Fe-20Cr-43Ni-10P and Fe-20Cr-20Ni-8P-5Si-2Mo. A primary crystal and the final solidified region are observed, and the final solidified region is composed of the dark gray phase and the bright gray phase as well. As same as Fe-20Cr-43Ni-10P and the Fe-20Cr-20Ni-8P-5Si-2Mo, corrosion occurred in the final solidified region of the joints.

In conclusion, for the fillet areas, corrosion occurred only in the final solidified region in the joints brazed with Fe-20Cr-43Ni-10P, Fe-20Cr-20Ni-8P-5Si-2Mo and Ni-29Cr-6P-4Si.

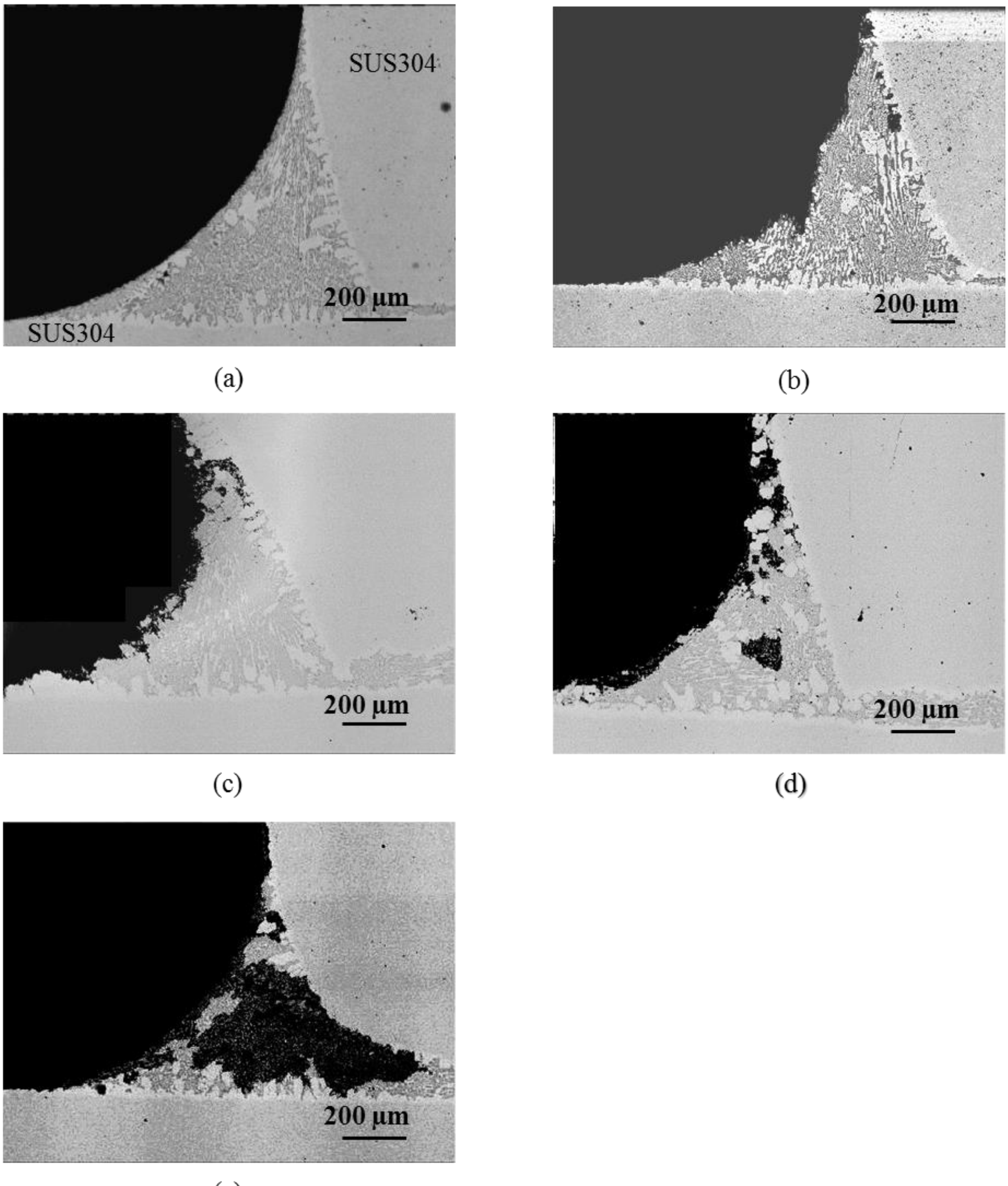

(a) (b) (c) (d) (e)

Fig. 4.3.5 Morphologies of cross sections of fillet areas of joints brazed with Fe-20Cr-43Ni-10P filler metal for different immersion time (back-scattered electron images).
(a) before immersion, (b) 50 h, (c) 100 h, (d) 200 h, (e) 300 h.

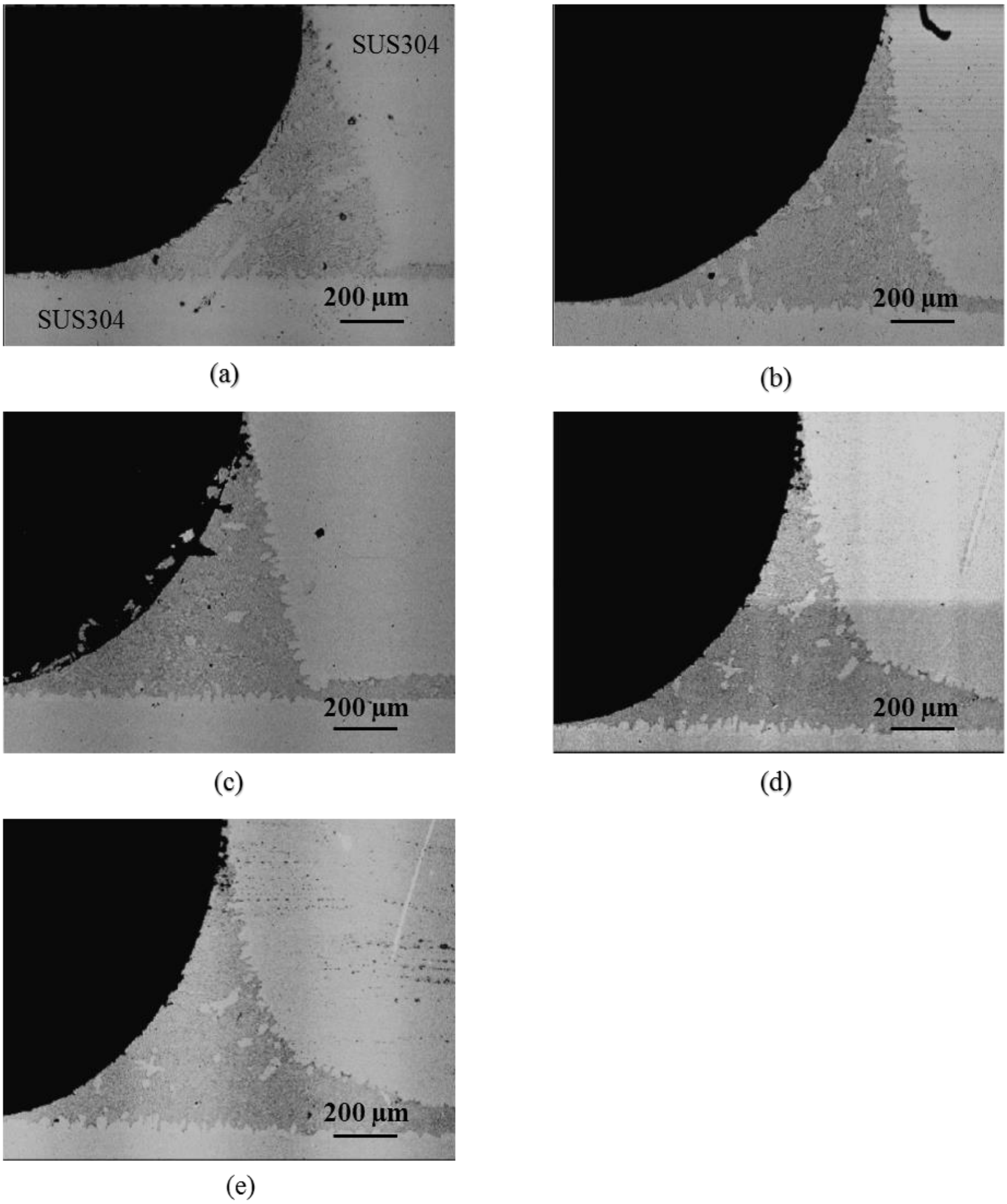

(a) (b) (c) (d) (e)

Fig. 4.3.6 Morphologies of cross sections of fillet areas of joints brazed with Fe-20Cr-20Ni-8P-5Si-2Mo filler metal for different immersion time (back-scattered electron images).
(a) before immersion, (b) 50 h, (c) 100 h, (d) 200 h, (e) 300 h.

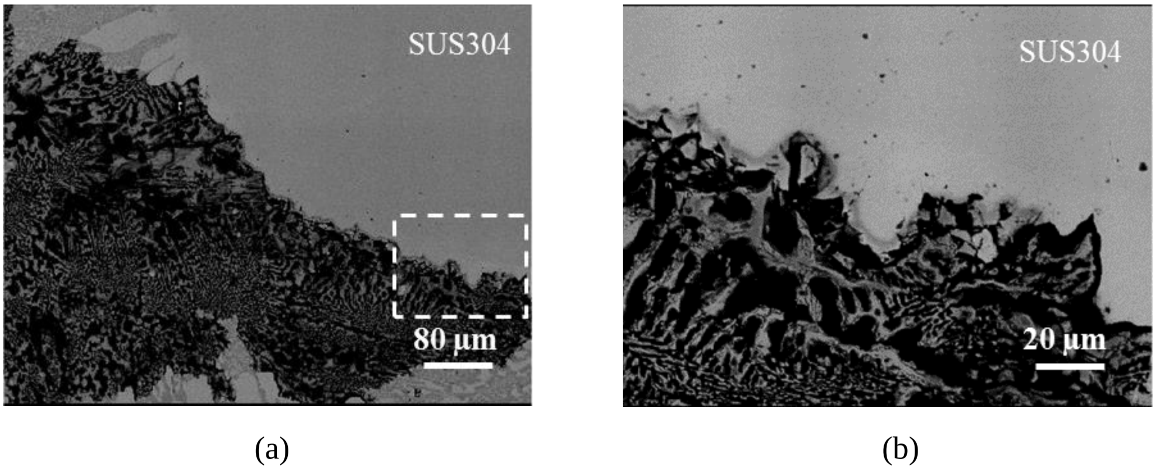

Fig. 4.3.7 Morphologies of cross sections of primary crystal in fillet areas of joint brazed with Fe-20Cr-43Ni-10P filler metal after immersion test for 300 h (back-scattered electron images).
(a) general view of primary crystal in fillet areas,
(b) magnified image of dotted area shown in (a).

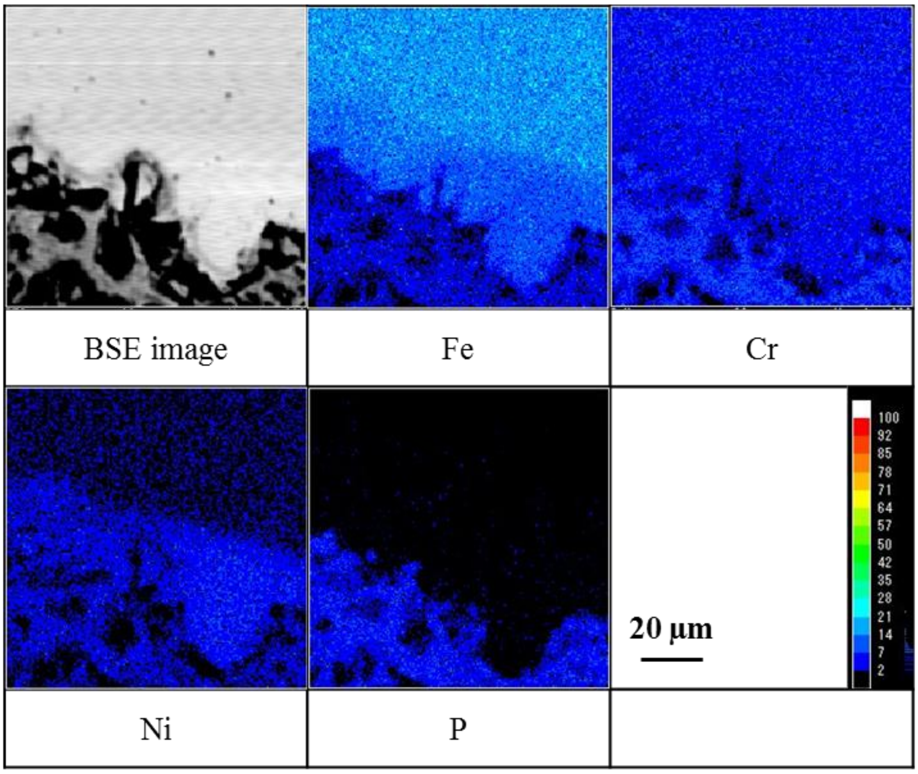

Fig. 4.3.8 Mapping analysis results of cross section of primary crystal in fillet areas of joint brazed with Fe-20Cr-43Ni-10P filler metal after immersion test for 300 h.

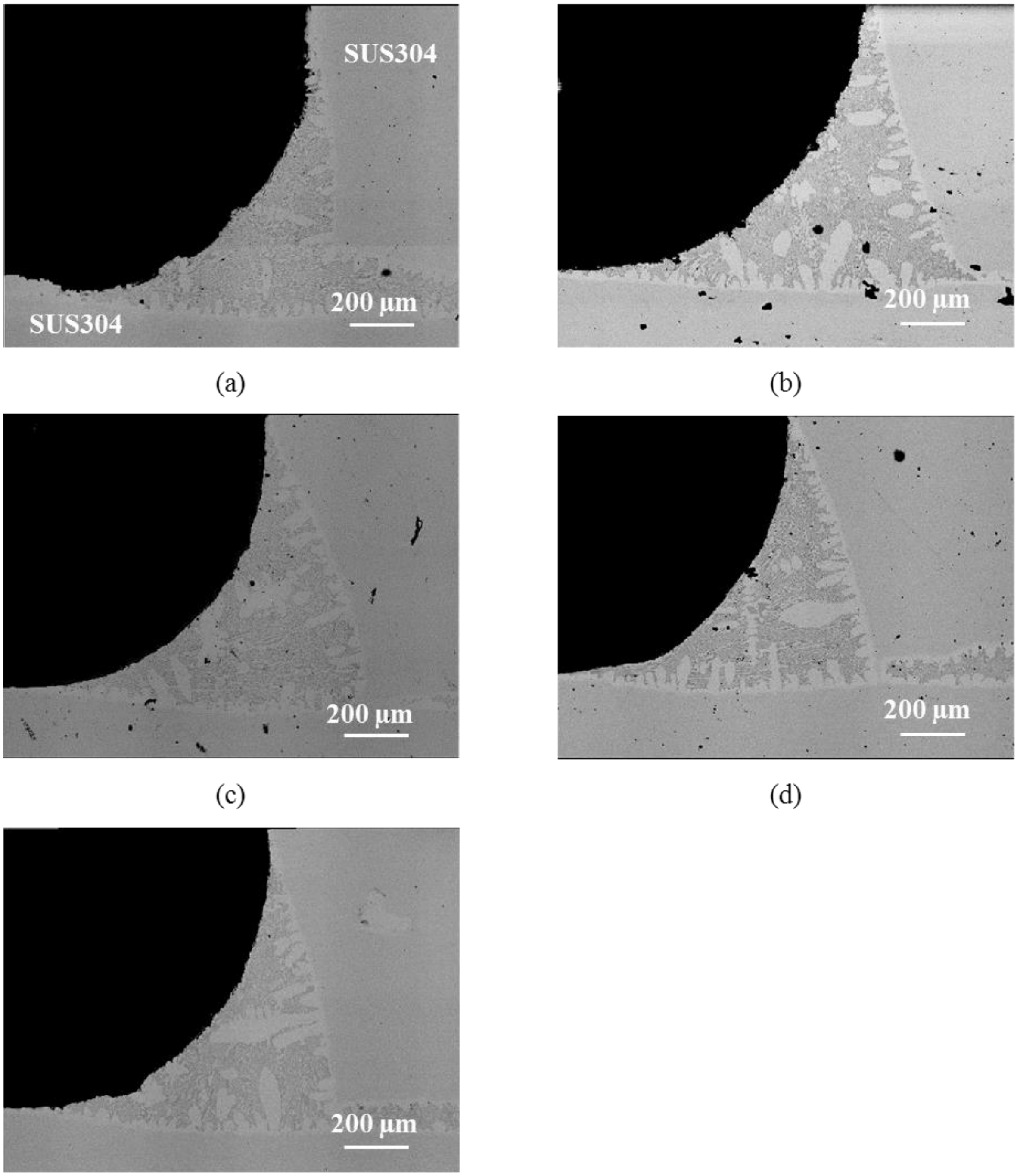

(a) (b) (c) (d) (e)

Fig. 4.3.9 Morphologies of cross sections of fillet areas of joints brazed with Ni-29Cr-6P-4Si filler metal at different immersion time (back-scattered electron images).
(a) before immersion, (b) 50 h, (c) 100 h, (d) 200 h, (e) 300 h.

### 4.3.3.2 Microstructure characterization of interfaces between fillet areas and SUS304 matrix metals after immersion test

Morphologies of the interfaces between the fillet area and SUS304 matrix are shown in Fig. 4.3.10, 4.3.11 and 4.3.12. It is not found that corrosion occurred near the interface in the joints brazed with Fe-20Cr-43Ni-10P, Fe-20Cr-20Ni-8P-5Si-2Mo and Ni-29Cr-6P-4Si filler metals.

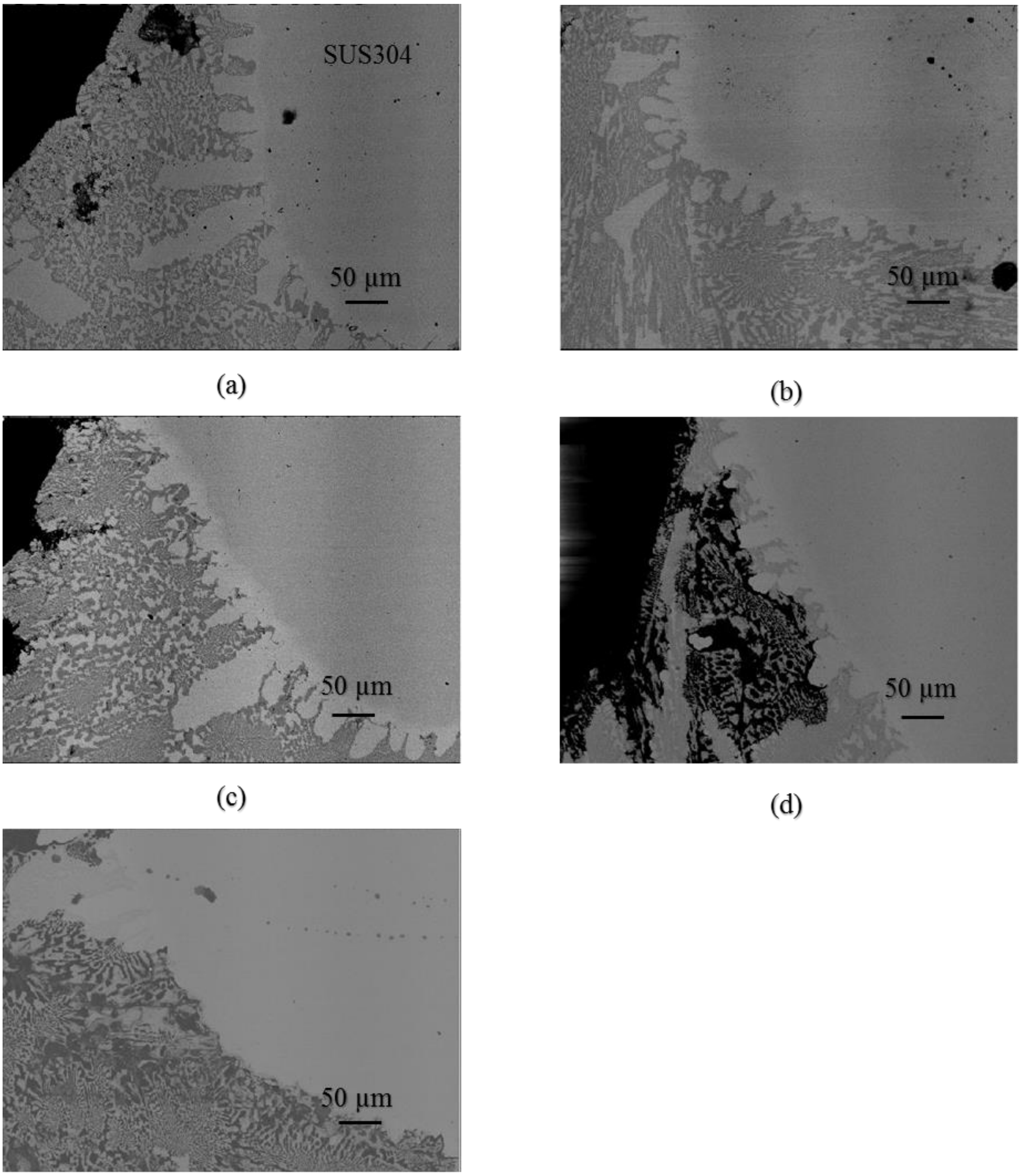

(a) (b) (c) (d) (e)

Fig. 4.3.10 Morphologies of cross sections of interfaces between fillet areas and SUS304 matrix metals in joints brazed with Fe-20Cr-43Ni-10P filler metal (back-scattered electron images).

(a) before immersion, (b) 50 h, (c) 100 h, (d) 200 h, (e) 300 h.

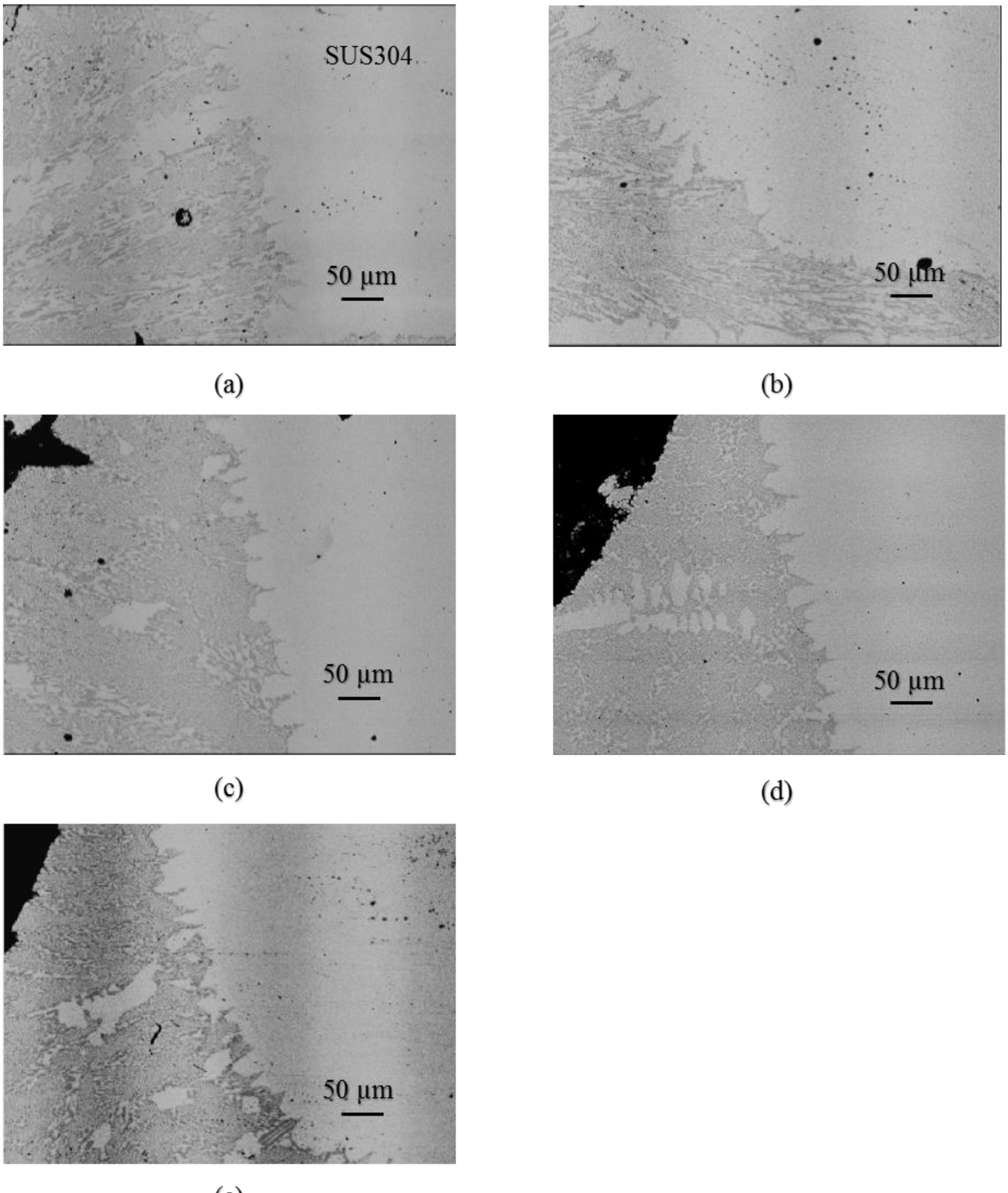

(a) (b)

(c) (d)

(e)

Fig. 4.3.11 Morphologies of cross sections of interfaces between fillet areas and SUS304 matrix metals in joints brazed with Fe-20Cr-20Ni-8P-5Si-2Mo filler metal (back-scattered electron images).

(a) before immersion, (b) 50 h, (c) 100 h, (d) 200 h, (e) 300 h.

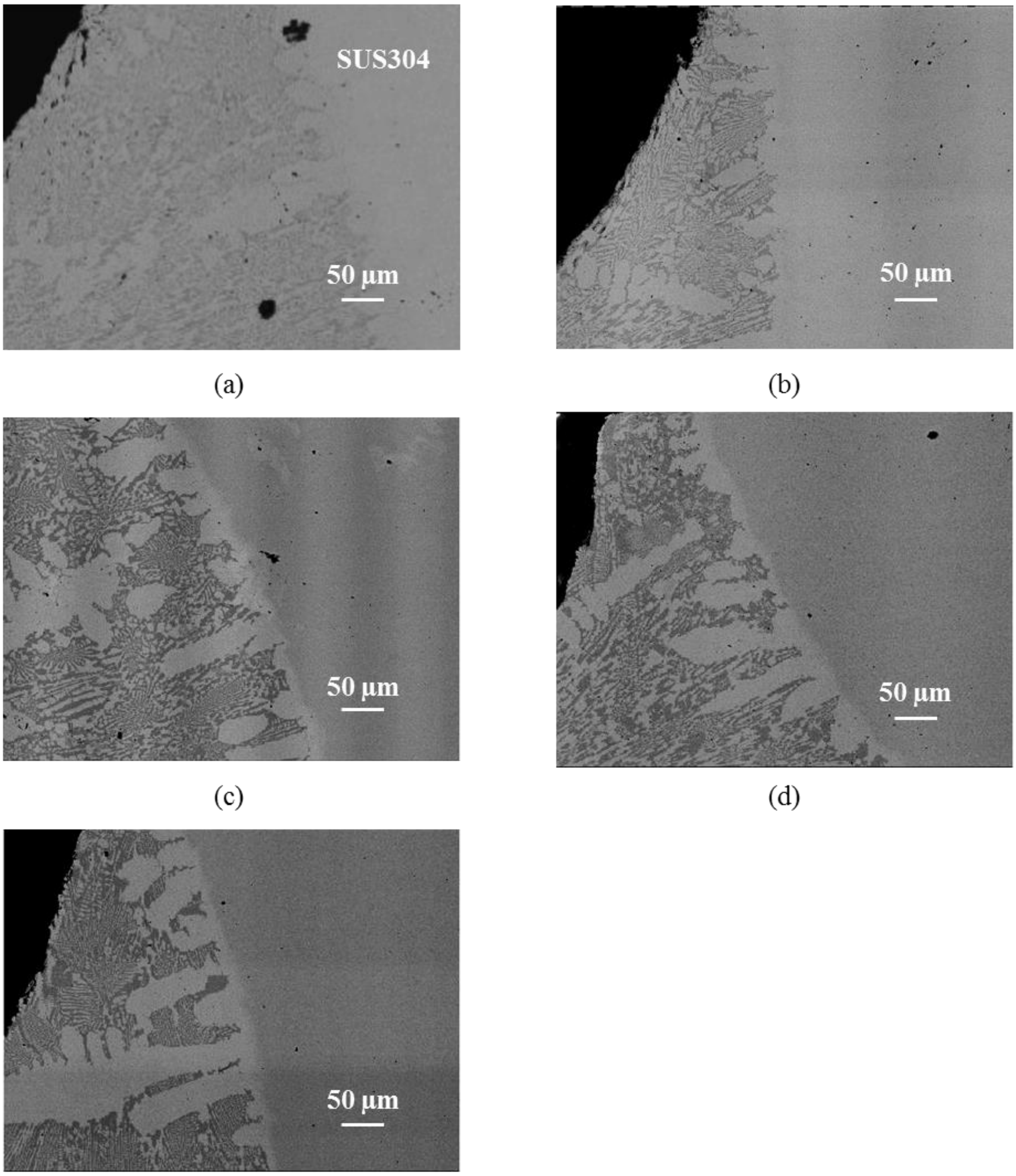

(a) (b) (c) (d) (e)

Fig. 4.3.12 Morphologies of cross sections of interfaces between fillet areas and SUS304 matrix metals in joints brazed with Ni-29Cr-6P-4Si filler metal (back-scattered electron images).

(a) before immersion, (b) 50 h, (c) 100 h, (d) 200 h, (e) 300 h.

#### 4.3.3.3 Microstructure characterization of SUS304 stainless steel matrixes after immersion test

CCD images of the surfaces of the joints after the immersion test are shown in Fig. 4.3.12, 4.3.13 and 4.3.14. It is observed that corrosion attack is not found on the surfaces of SUS304 stainless steels while corrosion occurred in the fillet area. This fact results from the self-passivation characteristic of SUS304 for the experimental electrolyte (shown in 4.3.1). It is confirmed that the galvanic corrosion does not occur between the fillet area and SUS304 matrix metal in the joints brazed with Fe-20Cr-43Ni-10P, Fe-20Cr-20Ni-8P-5Si-2Mo and Ni-29Cr-6P-4Si filler metals.

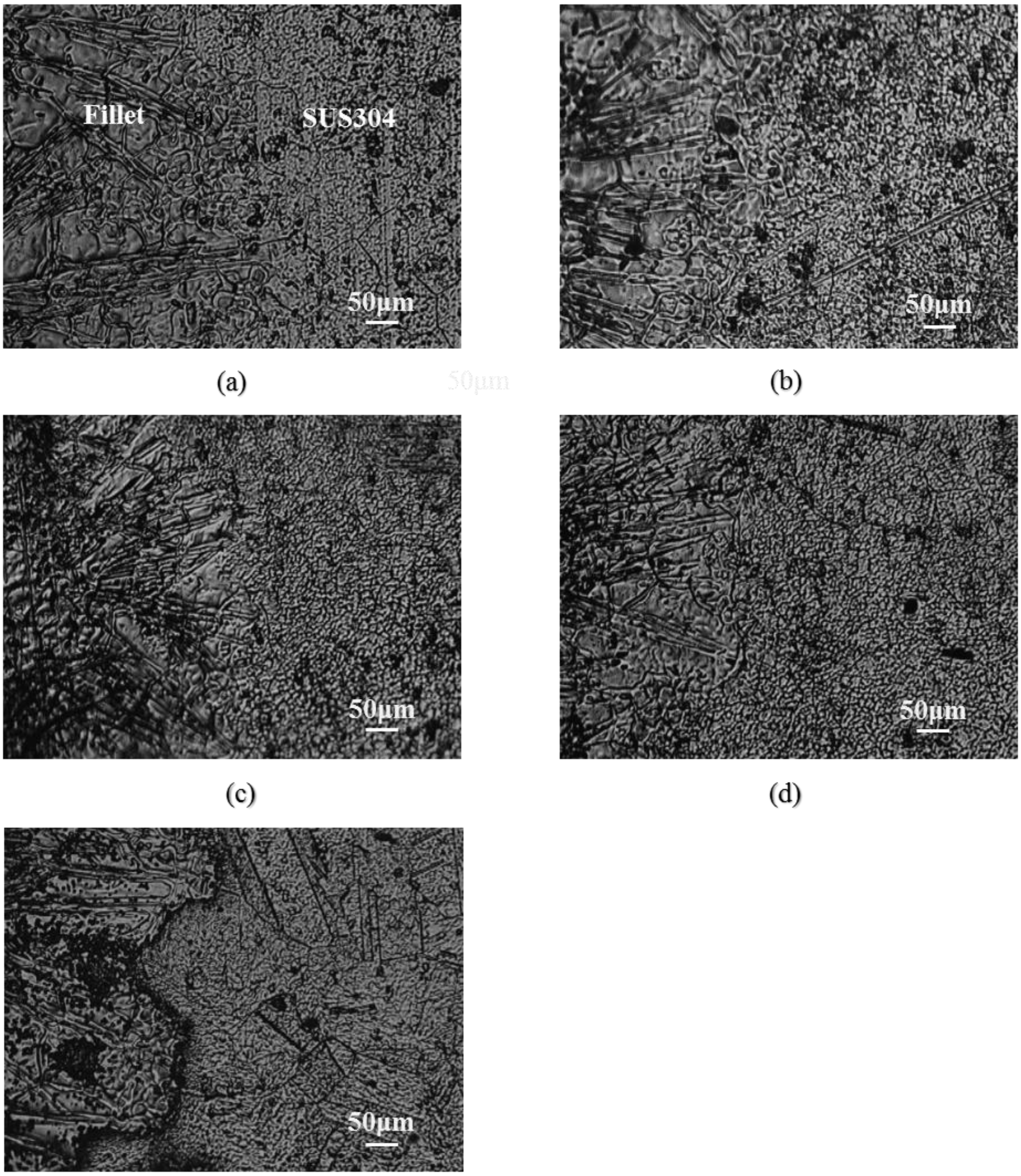

(a) (b)

(c) (d)

(e)

Fig. 4.3.12 CCD images of surfaces of SUS304 stainless steels in joints brazed with Fe-20Cr-43Ni-10P filler metal after immersion test for different time.
(a) before immersion, (b) 50 h, (c) 100 h, (d) 200 h, (e) 300 h.

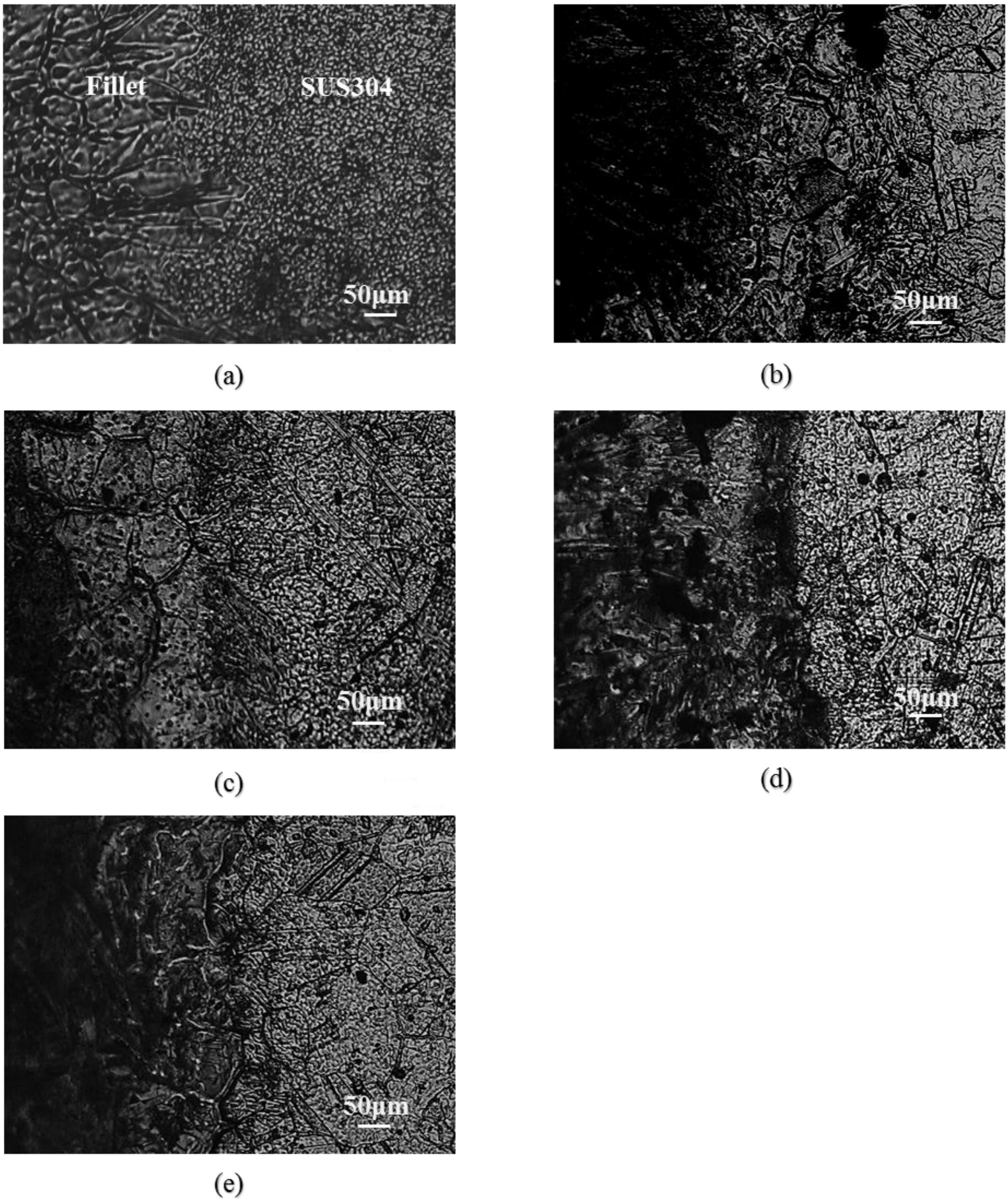

(a) (b) (c) (d) (e)

Fig. 4.3.13 CCD images of surfaces of SUS304 stainless steels in joints brazed with Fe-20Cr-20Ni-8P-5Si-2Mo filler metal after immersion test for different time.
(a) before immersion, (b) 50 h, (c) 100 h, (d) 200 h, (e) 300 h.

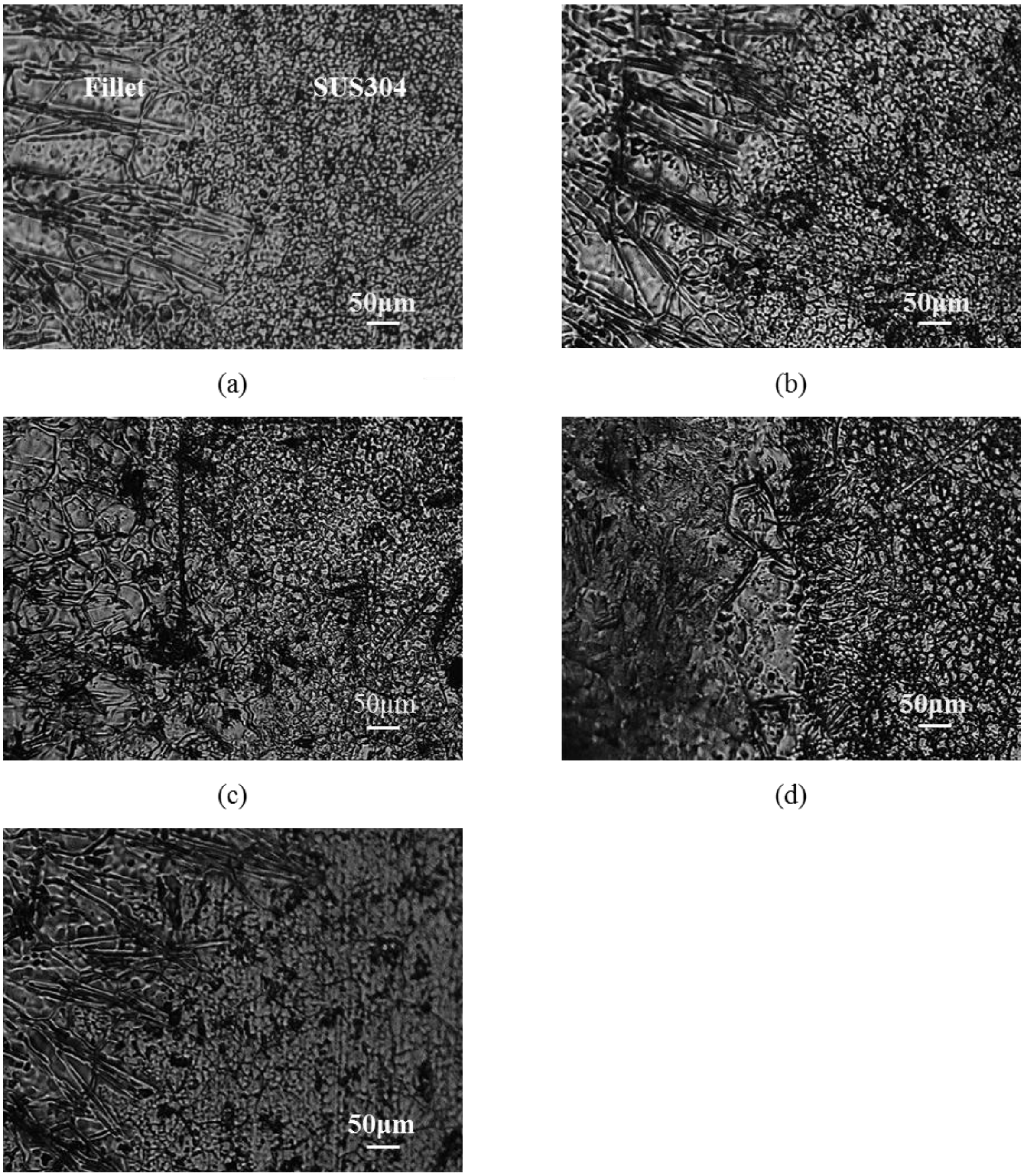

(a) (b) (c) (d) (e)

Fig. 4.3.14 CCD images of surfaces of SUS304 stainless steels in joints brazed with Ni-29Cr-6P-4Si filler metal after immersion test for different time.
(a) before immersion, (b) 50 h, (c) 100 h, (d) 200 h, (e) 300 h.

#### 4.3.3.4 Corrosion behavior of SUS304 stainless steel joints

As discussed in 4.3.3.1, 4.3.3.2 and 4.3.3.3, corrosion doesn’t occur on the surfaces of the primary crystals and SUS304 stainless steel matrix. The interfaces between the fillet areas and SUS304 matrix metals aren’t corroded. Corrosion occurs only in the final solidified region in the fillet areas. In other words, for SUS304 stainless steel joints, corrosion behavior is self-corrosion of the final solidified region in the fillet area in this study.

Therefore, the electrochemical characteristics of Fe-Cr-based brazing filler metals investigated in chapter 2 apply to SUS304 stainless steel joints brazed with Fe-Cr-based brazing filler metals as well. The solid-solution phase and phosphide phase in the final solidified region form a galvanic couple. The solid-solution phase is the anode and the phosphide phase becomes the cathode.

### 4.3.4 Corrosion resistance of SUS304 stainless steel joints

Mass losses measurements can only give a global loss of samples but can’t take into account localized corrosion instead of thickness loss measurements [32]. In this study, the maximum penetration depths were measured. The ratio of the maximum penetration depth to corrosion time is used to express approximate corrosion rate.

As discussed in 4.3.3, in SUS304 stainless steel joints, corrosion behavior is the self-corrosion of the final solidified region in the fillet area. In other words, corrosion resistance of SUS304 stainless steel joints is only concerned with the final solidified region in the fillet area. The morphologies of the cross sections of the final solidified regions in the joints brazed with Fe-20Cr-43Ni-10P, Fe-20Cr-20Ni-8P-5Si-2Mo and Ni-29Cr-6P-4Si after the immersion test for different immersion time are respectively shown in Fig. 4.3.15, 4.3.16 and 4.3.17. The maximum penetration depths in the final solidified regions were measured with a software accompanied by an EPMA. Numerical values of the maximum penetration depths are shown in Table 4.3.3. As a function of time, the maximum penetration depths are plotted in Fig. 4.3.18.

As shown in Fig. 4.3.18, the maximum penetration depth is nearly constant with the immersion time for the joints brazed with Fe-20Cr-20Ni-8P-5Si-2Mo and Ni-29Cr-6P-4Si. For the joints brazed with Fe-20Cr-43Ni-10P, the maximum penetration depth increases almost linearly with the immersion time up to 200 h, followed by increasing in a large slope. It is clear that the corrosion is accelerated with immersion time. The corrosion rate is approximately 1.5-1.8 μm/h at the first 200 h, and come up to 2.99 between 200 h and 300 h for the joints brazed with Fe-20Cr-43Ni-10P. On the other hand, the corrosion rate has retained at around 0.3 μm/h and 0.1 μm/h for the joints brazed with Fe-20Cr-20Ni-8P-5Si-2Mo and Ni-29Cr-6P-4Si, respectively. Compared with the Ni-based filler metal, the joints brazed with Fe-20Cr-20Ni-8P-5Si-2Mo have slightly weaker corrosion resistance. In contrast, the joints brazed with Fe-20Cr-43Ni-10P are much more severely attacked than the joint brazed with Fe-20Cr-20Ni-8P-5Si-2Mo.

As described in 4.3.2, no Cr-poor phase and fine microstructure were observed for Fe-20Cr-20Ni-8P-5Si-2Mo filler metal. Sufficient Cr content and fine microstructure can improve corrosion resistance of the filler metal [33-35], therefore, it is no Cr-poor phase and fine microstructure that promotes corrosion resistance of Fe-20Cr-20Ni-8P-5Si-2Mo. In contrast, Fe-20Cr-43Ni-10P does not nearly provide the corrosion resistance as a result of the formation of Cr-poor phase of the lower Cr content.

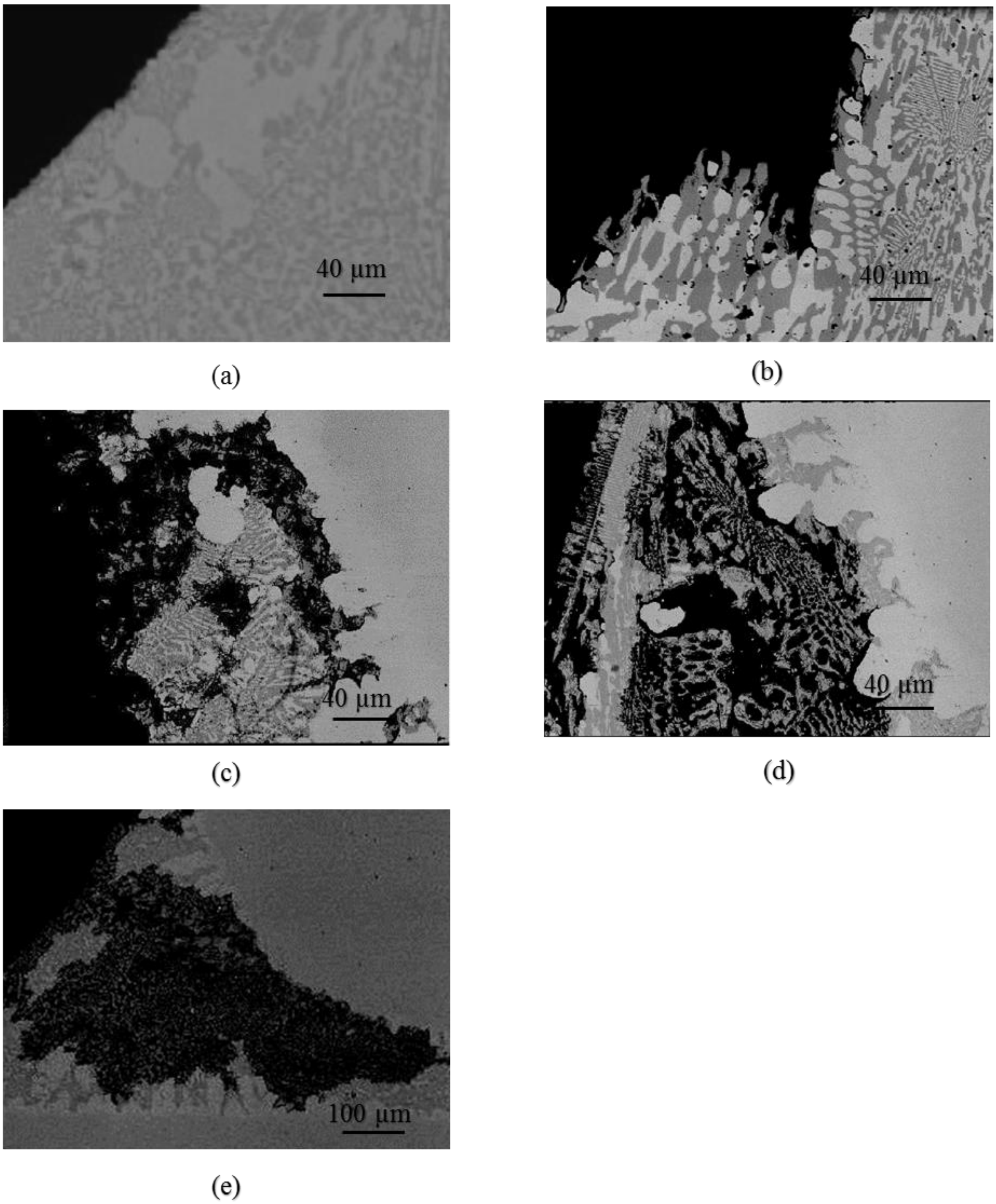

Fig. 4.3.15 Morphologies of cross sections of final solidified regions of fillet areas in joints brazed with Fe-20Cr-43Ni-10P filler metal after immersion test for different immersion time (back-scattered electron images).

(a) before immersion, (b) 50 h, (c) 100 h, (d) 200 h, (e) 300 h.

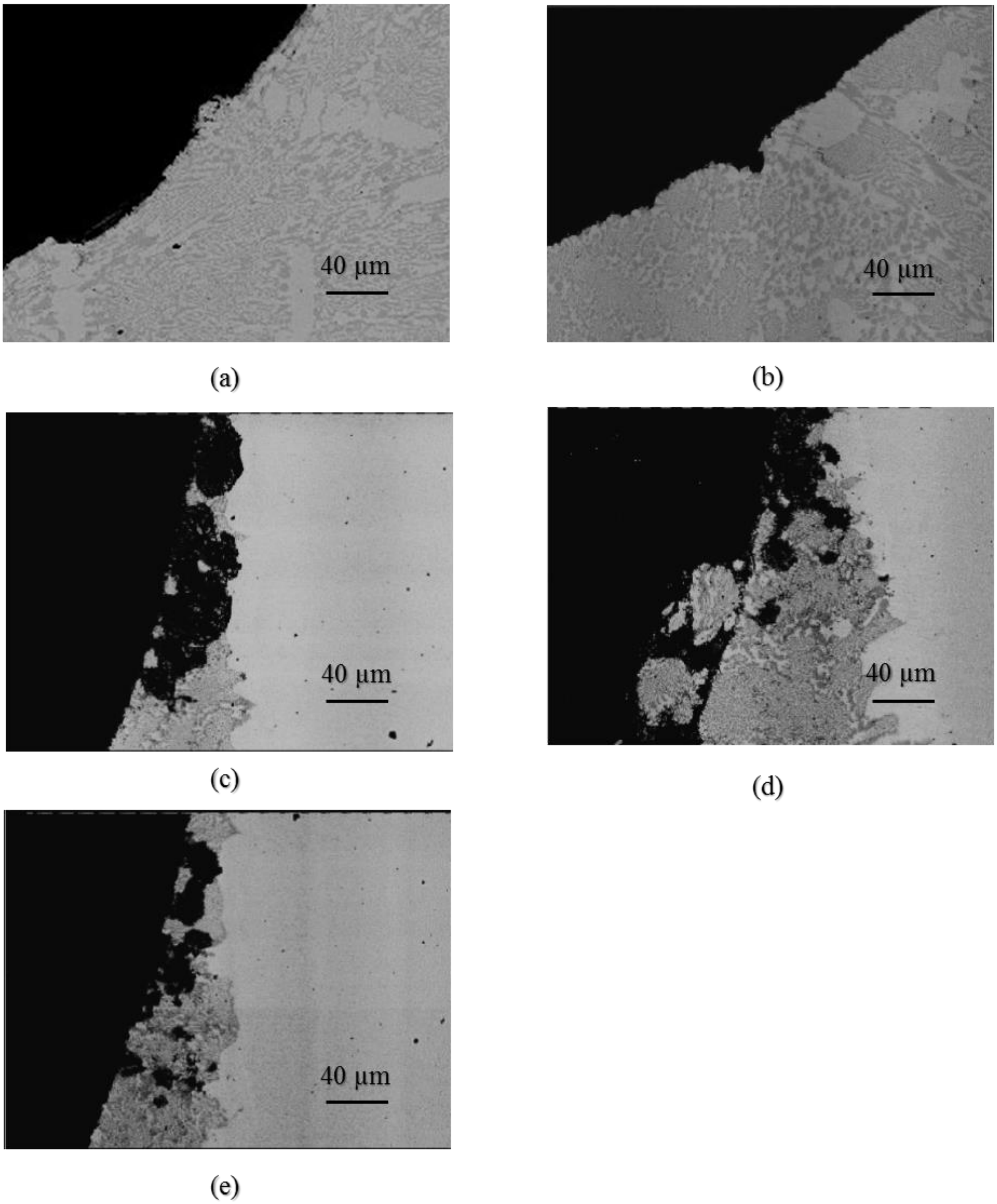

(a) (b) (c) (d) (e)

Fig. 4.3.16 Morphologies of cross sections of final solidified regions of fillet areas in joints brazed with Fe-20Cr-20Ni-8P-5Si-2Mo filler metal after immersion test for different immersion time (back-scattered electron images).

(a) before immersion, (b) 50 h, (c) 100 h, (d) 200 h, (e) 300 h.

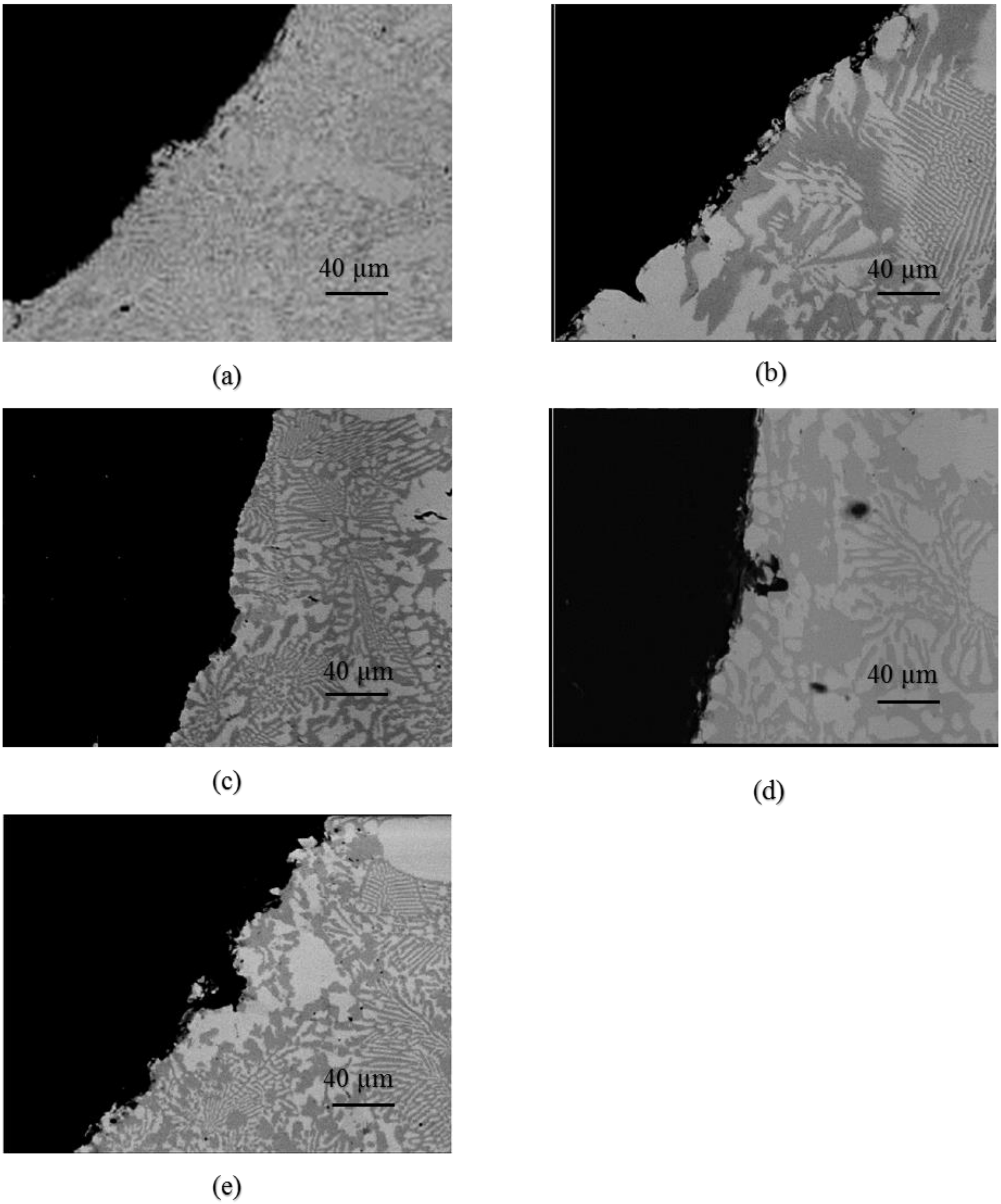

Fig. 4.3.17 Morphologies of cross sections of final solidified regions of fillet areas in joints brazed with Ni-29Cr-6P-4Si filler metal after immersion test for different immersion time (back-scattered electron images).

(a) before immersion, (b) 50 h, (c) 100 h, (d) 200 h, (e) 300 h.

Table 4.3.3 Maximum penetration depths measured.

| Brazing filler metal (mass%) | Corrosion time (h) | Maximum penetration depth (μm) | Corrosion rate (μm/h) |
|---|---|---|---|
| Fe-20Cr-43Ni-10P | 50 | 91 | 1.82 |
| | 100 | 181 | 1.81 |
| | 200 | 304 | 1.52 |
| | 300 | 897 | 2.99 |
| Fe-20Cr-20Ni-8P-5Si-2Mo | 50 | 24 | 0.28 |
| | 100 | 34 | 0.34 |
| | 200 | 56 | 0.28 |
| | 300 | 67 | 0.23 |
| Ni-29Cr-6P-4Si | 50 | 6 | 0.12 |
| | 100 | 10 | 0.10 |
| | 200 | 15 | 0.08 |
| | 300 | 27 | 0.09 |

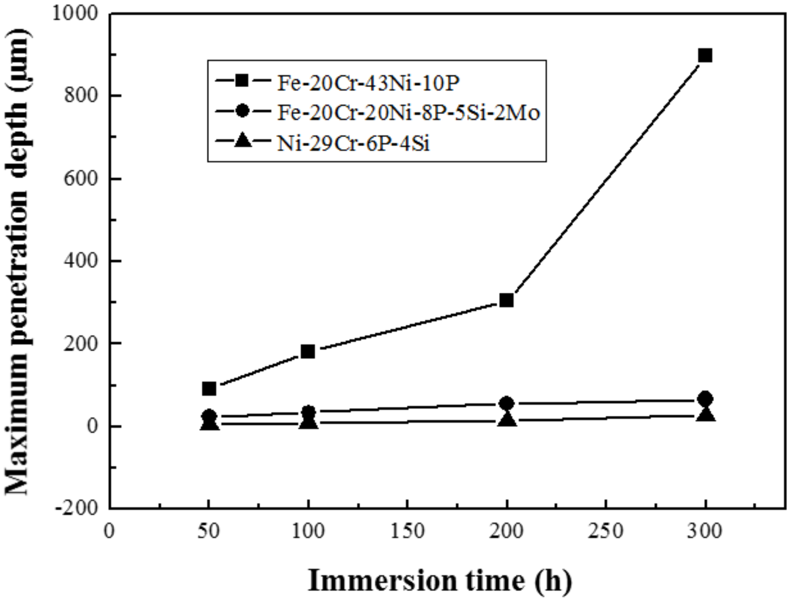

Fig. 4.3.18 Maximum penetration depths with immersion time.

### 4.3.5 Accelerated corrosion in joints brazed with Fe-20Cr-43Ni-10P filler metal

Compared with the joints brazed with Fe-20Cr-20Ni-8P-5Si-2Mo and Ni-29Cr-6P-4Si, the joints brazed with Fe-20Cr-43Ni-10P exhibit the poor corrosion resistance. This fact is associated with the inferior electrochemical characteristics of Fe-20Cr-43Ni-10P (for details, see 2.3.4). Furthermore, different from the joints brazed with Fe-20Cr-20Ni-8P-5Si-2Mo and Ni-29Cr-6P-4Si, it is noticeable for the joints brazed with Fe-20Cr-43Ni-10P filler metal that corrosion is accelerated and the corrosion resistance deteriorates with immersion time. In this section, the cause of accelerated corrosion is investigated.

As discussed in 4.3.3, for the SUS304 stainless steel joints brazed with Fe-20Cr-43Ni-10P, corrosion behavior is the self-corrosion of the final solidified region in the fillet areas. Hence, the electrochemical characteristics of the brazing filler metals refer to the joints. In other words, it can be deduced for the SUS304 stainless steel joints brazed with Fe-20Cr-43Ni-10P that the corrosion is the galvanic corrosion between the solid-solution phase and phosphide phase in the final solidified region. The solid-solution phase is the anode and the phosphide phase becomes the cathode.

Compared with smashed corrosion for the joints brazed with Fe-20Cr-20Ni-8P-5Si-2Mo and Ni-29Cr-6P-4Si as shown in Fig. 4.3.16 and Fig. 4.3.17, the phosphide phase remains till the joint is entirely corroded as shown in Fig. 4.3.19 (a) in the joint brazed with Fe-20Cr-43Ni-10P. This is confirmed by the mapping analysis of the joint shown in Fig. 4.3.20. It is indicated that the phosphide phase is continuously distributed in the final solidified region of the filler area in the joint brazed with Fe-20Cr-43Ni-10P.

It has well been known that corrosion resistance of materials can be expressed by the contact current density [36]. In case of a good conductivity of the electrolyte and a negligible polarization resistance of the anode, an approximation for the contact current density between the joined materials can be given by Eq. 4.3.1 [37].

$$J_a = (U_{\mathrm{R.k}} - U_{\mathrm{R.a}})/r_{\mathrm{K}} \times S_{\mathrm{k}}/S_{\mathrm{a}} \qquad (4.3.1)$$

$$V = S_{\mathrm{k}}/S_{\mathrm{a}} \qquad (4.3.2)$$

$J_{\mathrm{a}}$ is the contact current density, $U_{\mathrm{R.k}}$ and $U_{\mathrm{R.a}}$ are the corrosion potentials of the cathode and the anode respectively, $r_{\mathrm{K}}$ represents the specific polarization resistance of the cathode. $S_{\mathrm{k}}$ and

$S_a$ are the areas of the cathode and the anode respectively. Eq. 4.3.1 shows that the contact current density depends directly on the potential difference and the area ratio $V$. To reduce a corrosive damage caused by the galvanic corrosion, the potential difference and the area ratio should be minimized. For the joint brazed with Fe-20Cr-43Ni-10P, the phosphide phase which is the cathode has almost been retained. It means that the cathode area increases continuously with corrosion time, resulting in the greater increasing of the area ratio $V$. It is an unfavorable area ratio which consists of large cathode and a small anode that lead to the greater corrosion rate in the joint brazed with Fe-20Cr-43Ni-10P with corrosion time.

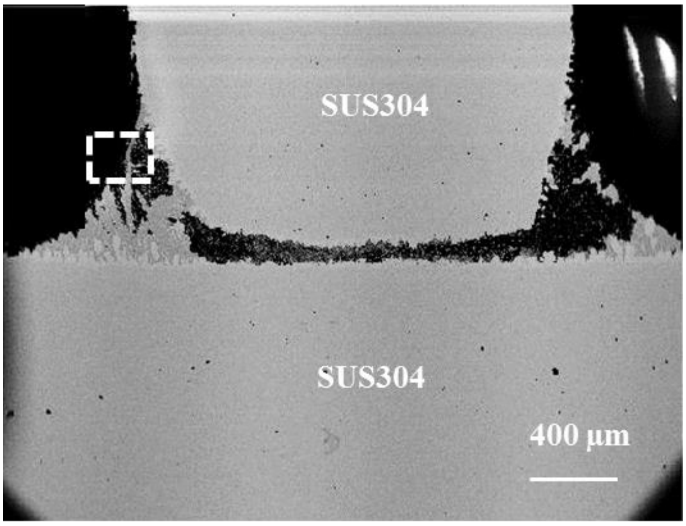

(a)

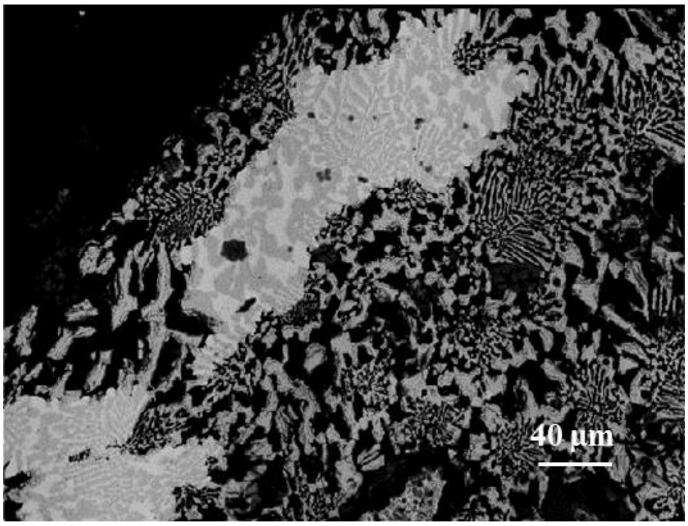

(b)

Fig. 4.3.19 Morphologies of cross sections of final solidified region of fillet area in joint brazed with Fe-20Cr-43Ni-10P filler metal after immersion test for 300 h (back-scattered electron images).

(a) general view of fillet area, (b) magnified image of dotted area shown in (a).

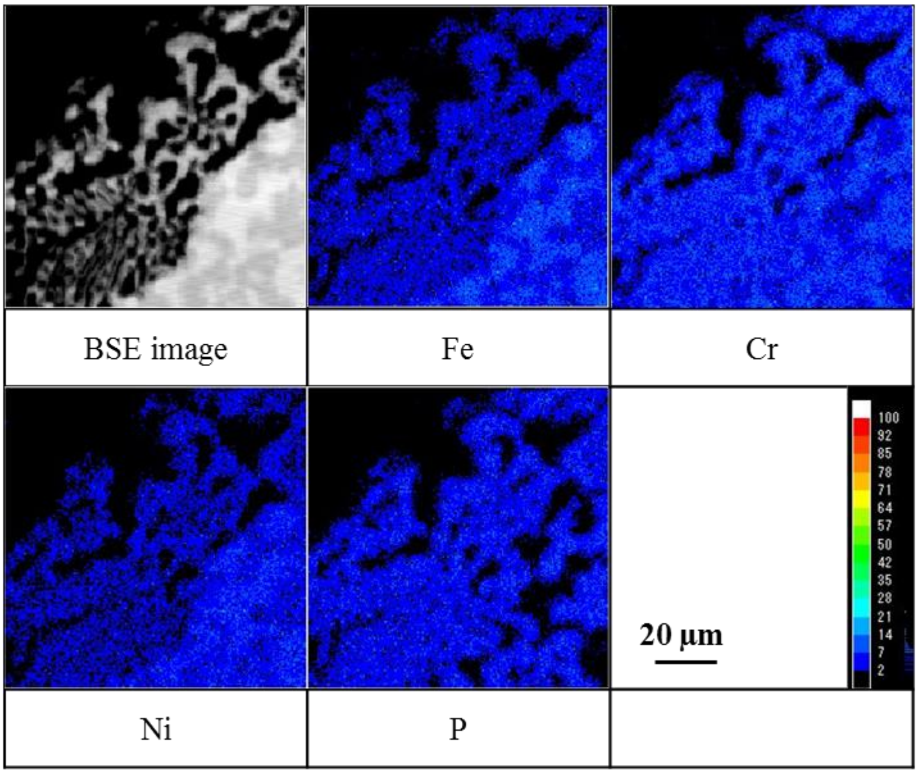

Fig. 4.3.20 Mapping analysis result of cross section of final solidified region in joint brazed with Fe-20Cr-43Ni-10P filler metal after immersion test for 300 h.

### 4.3.6 Effect of microstructure on corrosion resistance of joints brazed with Fe-20Cr-20Ni-8P-5Si-2Mo filler metal

As shown in Fig.4.3.18, different from the joints brazed with Fe-20Cr-43Ni-10P, there is no significant change in the maximum penetration depths and the maximum penetration depths keep almost constant along with increasing of immersion time in the joints brazed with Fe-20Cr-20Ni-8P-5Si-2Mo and Ni-29Cr-6P-4Si. The joints brazed with Fe-20Cr-20Ni-8P-5Si-2Mo exhibit almost as the same high corrosion resistance as the joints brazed with Ni-29Cr-6P-4Si. In addition, as shown in Figs. 4.3.15, 4.3.16 and 4.3.17, completely unlike Fe-20Cr-43Ni-10P, for Fe-20Cr-20Ni-8P-5Si-2Mo and Ni-29Cr-6P-4Si, corroded areas fall off as masses from the final solidified regions and cavities occur instead of remained phosphide phases. These facts imply that not only the composition but also the microstructure affect the corrosion resistance of the joints brazed with Fe-20Cr-20Ni-8P-5Si-2Mo.

The microstructure, particularly the morphology of the phase acting as a cathode, affects the corrosion behavior. The phase accelerates corrosion or hinder corrosion as a corrosion barrier if the phase is in the form of a continuous network [38, 39].

As shown in Fig. 4.3.21, for the joints brazed with Fe-20Cr-20Ni-8P-5Si-2Mo, the fine solid-solution phase acts as the anode and the phosphide phase acts as the cathode in the micro-galvanic corrosion. Owing to a tiny grain size, the fine solid-solution phase is finely divided in the microstructure. Corrosion preferentially occurs where the fine solid-solution phase is continuous. After the solid-solution phase is corroded, corrosion areas fall off from the surface and cavities form on the surface. At the same time, the continuous phosphide phase is exposed on the surface of the cavities. The continuous phosphide phase hinders corrosion in the deep direction as a corrosion barrier, which results in the high corrosion resistance of the joints brazed with Fe-20Cr-20Ni-8P-5Si-2Mo.

On the other hand, for the joints brazed with Fe-20Cr-43Ni-10P, as shown in Fig. 4.3.22, the coarse solid-solution phase has been united in the deep direction and continuous phosphide phase cannot form. Along with the corrosion of the coarse solid-solution phase, the phosphide phase is almost remained and the cathode area increases. The increase in the area ratio of the cathode to the anode results in an accelerated corrosion.

Therefore, the fine microstructure is the reason why the joints brazed with Fe-20Cr-20Ni-8P-5Si-2Mo have the high corrosion resistance.

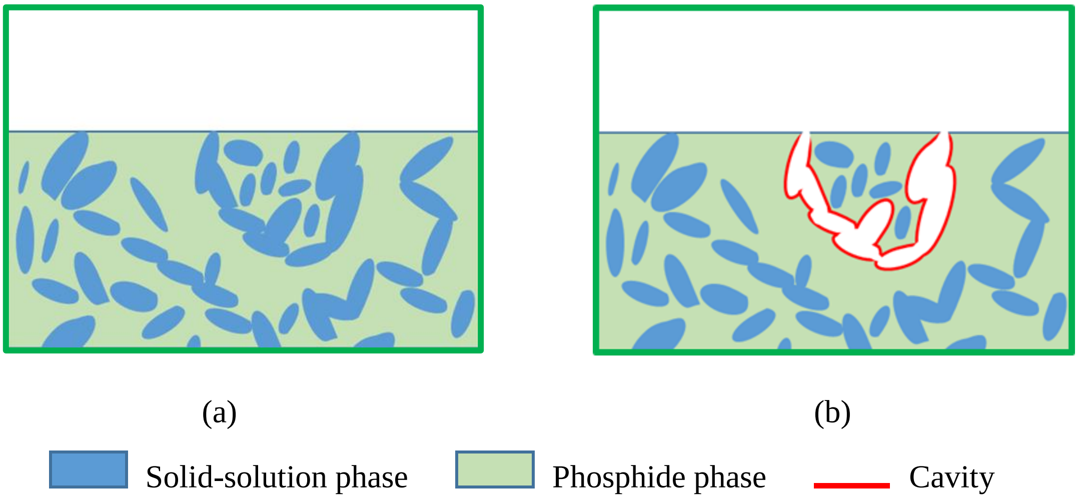

Fig. 4.3.21 Schematic diagrams of fine microstructure as a corrosion barrier. (a) before corrosion, (b) after corrosion.

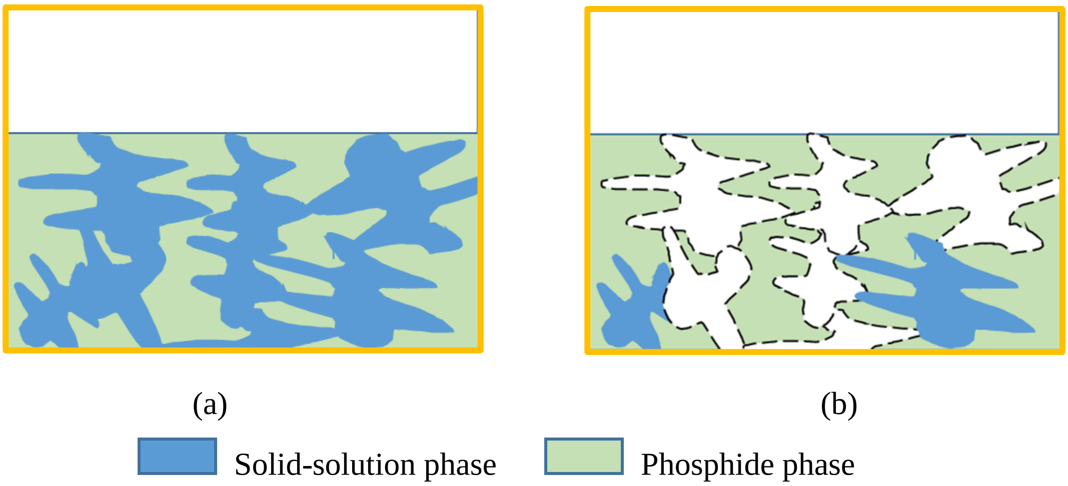

Fig. 4.3.22 Schematic diagrams of coarse microstructure as a cathode accelerating corrosion. (a) before corrosion, (b) after corrosion.

## 4.4 Conclusions

The corrosion resistance of SUS304 stainless steel joints using Fe-Cr-based brazing filler metals was extensively evaluated in this chapter. Important conclusions are summarized as below:

1) The microstructures of the fillet areas of the joints brazed with Fe-20Cr-43Ni-10P and Fe-20Cr-20Ni-8P-5Si-2Mo are made up of the primary crystal and the final solidified region. The primary crystals of the joints brazed with Fe-20Cr-43Ni-10P and Fe-20Cr-20Ni-8P-5Si-2Mo appear to be Fe-Cr-Ni-based and Fe-Cr-Ni-Si-based solid-solution phases, respectively. The final solidified region of the joint brazed with Fe-20Cr-43Ni-10P is composed of a Fe-Cr-Ni-based solid-solution phase and Cr-P-Fe-Ni-based phosphide phase. The final solidified region of the joint brazed with Fe-20Cr-20Ni-8P-5Si-2Mo contains a Fe-Cr-Ni-Si-based solid-solution phase and a Cr-P-Fe-Ni-Mo-based phosphide phase.

2) Corrosion occurred only in the final solidified region of the fillet area in SUS304 stainless steel joints brazed with both Fe-20Cr-43Ni-10P and Fe-20Cr-20Ni-8P-5Si-2Mo. Corrosion is self-corrosion of the final solidified regions in the joints with the Fe-Cr-based brazing filler metals.

3) Compared with Ni-based filler metal, the corrosion resistance of the joint brazed with Fe-20Cr-20Ni-8.0P-5.0Si-2.0Mo is slightly weaker. On the other hand, the joint brazed with Fe-20Cr-43Ni-10P does not nearly provide corrosion resistance.

4) Corrosion was accelerated with corrosion time in the joint brazed with Fe-20Cr-43Ni-10P because the phosphide phase, which acts as the cathode, is almost retained and leads to the increasing of the area ratio of the cathode to the anode.

5) For the joints brazed with Fe-20Cr-20Ni-8P-5Si-2Mo, along with the corrosion of the fine solid-solution phase, the continuous phosphide phase is exposed on the surface. The continuous phosphide phase hinders corrosion in the deep direction as a corrosion barrier. The fine microstructure results in the high corrosion resistance of the joints.

References

[1] L.L. Ferreira Squaiella, C.A. Martins and P.T. Lacava: Fuel, **104** (2013) 183-193.

[2] M. Abarham, J. Hoard, D. Assanis, D. Styles, E.W. Curtis, N. Ramesh, C.S. Sluder, and J.M. Storey: SAE Technical Paper 2009-01-1506, (2009) 1-11.

[3] M.S. Abd-Elhady, T. Zornek, M.R. Malayeri, S. Balestrino, P.G. Szymkowicz and H. Müller-Steinhagen: International Journal of Heat and Mass Transfer, **54** (2011) 838-846.

[4] M.S. Abd-Elhady, M.R. Malayeri and H.M. Steinhagen: Heat Transfer Engineering, **32** (2011) 248-257.

[5] M. Abarham, J. Hoard and D. Assanis: International Journal of Fuels and Lubricants, **3** (2010) 690-704.

[6] M.R. Malayeri, T. Zornek, S. Balestrino, A. Warey and P.G. Szymkowicz: Heat Transfer Engineering, **34** (2013) 665-673.

[7] A. Warey, A.S. Bika, D. Long, S. Balestrino and P. Szymkowicz: International Journal of Heat and Mass Transfer, **65** (2013) 807-816.

[8] A. Warey, S. Balestrino, P. Szymkowicz and M.R. Malayeri: Aerosol Science and Technology, **46** (2012) 198-213.

[9] M.S. Abd-Elhady and M.R. Malayeri: Applied Thermal Engineering, **60** (2013) 96-104.

[10] K.S. Hong, J.S. Park and K.S. Lee: International Journal of Automotive Technology, **12** (2011) 813-820.

[11] S.H. Jang, S.J. Hwang, S.K. Park, K.S. Choi and H.M. Kim: Heat Mass Transfer, **48** (2012) 1081-1087.

[12] T. Hartmann and D. Nuetzel: Proceedings of the 5th International Brazing and Soldering Conference, (2012) 394-401.

[13] G.L. Song, B. Johannesson, S. Hapugoda and D. Stjohn: Corrosion Science **46** (2004) 955-977.

[14] L.H. Hihara and R.M. Latanision: Corrosion, **48** (1992) 546-552.

[15] M. Tavakkolizadeh and H. Saadatmanesh: Journal of Composites for Construction, **5** (2001) 200-210.

[16] B. Grosgogeat, L. Reclaru, M. Lissac and F. Dalard: Biomaterials, **20** (1999) 933-941.

[17] H.P. Hack: “Galvanic Corrosion”, ed. by ASTM, (1988) 5.

[18] C.L. Hu, S. Xia, H. Li, T. Liu, B.X. Zhou, W.J. Chen and N. Wang: Corrosion Science **53** (2011) 1880-1886.

[19] K. Wu, W.S. Jung and J.W. Byeon: Corrosion Science, **105** (2016) 8-16.

[20] X.G. Feng, X.Y. Lu, Y. Zuo, N. Zhuang and D. Chen: Corrosion Science, **103** (2016) 223-229.

[21] A. Chiba, I. Muto, Y. Sugawara and N. Hara: Corrosion Science, **106** (2016) 25-34.

[22] J.J. Shi, W. Sun, J.Y. Jiang and Y.M. Zhang: Construction and Building Materials, **111** (2016) 805-813.

[23] M. Ghahari, D. Krouse, N. Laycock, T. Rayment, C. Padovani, M. Stampanonie, F. Marone, R. Mokso and A.J. Davenport: Corrosion Science, **100** (2015) 23-35.

[24] W.M. Tian, S.M. Li, N. Du, S.B. Chen and Q.Y. Wu: Corrosion Science **93** (2015) 242-255.

[25] A.A. Aghuy, M. Zakeri, M.H. Moayed and M. Mazinani: Corrosion Science, **94** (2015) 368-376.

[26] W.Y. Lv, C. Pan, W. Su, Z.Y. Wang, S.N. Liu and C. Wang: Journal of Materials Engineering and Performance, **24** (2015) 2597-2604.

[27] L. Guan, Y. Zhou, B. Zhang, J.Q. Wang, E.H. Han and W. Ke: International Journal of Electrochemical Science, **11** (2016) 2326-2334.

[28] T. Fujita, T. Yamada and N. Takahashi: Tetsu to Hagane, **61** (1975) 357-370.

[29] K. Hosomi, H. Morimoto and Y. Ashida: Tetsu to Hagane, **74** (1988) 2025-2032.

[30] T. Nakazawa, S. Date, M. Tendo and M. Yamazaki: Tetsu to Hagane, **91** (2005) 670-675.

[31] G. Okamoto, S. Matsuda and I. Matsusima: “Fusyokuhannou to sonoseigyo”, ed. by Sangyoutosyo, (1984) 65-76.

[32] E. Schaal, N. David, P.J. Panteix, C. Rapin, J.M. Brossard and F. Maad: Oxidation of Metals, **84** (2015) 307-327.

[33] G. Okamoto, S. Matsuda and I. Matsusima: “Fusyokuhannou to sonoseigyo”, ed. by Sangyoutosyo, (1984) 65-76.

[34] K. Sugimoto: “Kinzokufusyokukougaku”, ed. by Uchidarokakuho, (2009) 107-159.

[35] I. Okamoto, T. Takemoto and C. Fujiwara: Journal of JWS, **48** (1979) 510-515.

[36] K. Sugimoto: Kinzokuhusyokukougaku, ed. by Uchidarokakuho, (2009) 74.

[37] L. Kruger and M. Mandel: Corrosion Science, **53** (2011) 624-629.

[38] M.C. Zhao, M. Liu, G. Song and A. Atrens: Corrosion Science, **50** (2008) 1939-1953.

[39] G.L. Song and A. Atrens: Advanced Engineering Materials, **1** (1999) 11-33.

# Chapter 5 Conclusions

## 5.1 Summary of this thesis

This study focused on two types of new Fe-Cr brazing filler metals, Fe-20Cr-43Ni-10P (mass%) and Fe-20Cr-20Ni-8P-5Si-2Mo (mass%), and discussed the electrochemical characteristics of the Fe-Cr brazing filler metals, joint strength and corrosion resistance of the joints brazed with the Fe-Cr brazing filler metals. The conclusions are summarized as follows.

In chapter 1, environmental problems in recent years and significance of substitution for Ni-based brazing filler metals were explored. The purposes of this study and composition of the thesis were described as well.

In chapter 2, the microstructures and melting properties were analyzed for the Fe-Cr brazing filler metals. Electrochemical characteristics and corrosion behavior were investigated by electrochemical and surface analysis techniques as well. The results are summarized as follows.

The microstructure is composed of a solid-solution primary crystal and a eutectic phase, and the eutectic phase is made up of a solid-solution phase and a phosphide phase in both Fe-20Cr-43Ni-10P and Fe-20Cr-20Ni-8P-5Si-2Mo. Fe-20Cr-43Ni-10P reveals the galvanic corrosion and Fe-20Cr-20Ni-8P-5Si-2Mo is attacked at a few localized areas so that cavities form on the surface. The solid-solution phase becomes the anode and the phosphide phase serves as the cathode during the corrosion reaction in both brazing filler metals. The solid-solution phase is corroded and the phosphide phase survives. Corrosion potentials were -0.16 V-SSE and -0.22 V-SSE in the experimental compound solution in Fe-20Cr-43Ni-10P and Fe-20Cr-20Ni-8P-5Si-2Mo, respectively. Fe-20Cr-43Ni-10P is difficultly corroded almost as same as Ni-29Cr-6P-4Si. However, Fe-20Cr-20Ni-8P-5Si-2Mo is more easily corroded than Ni-29Cr-6P-4Si. Corrosion rate and corrosion resistance cannot be evaluated by the corrosion current density and polarization resistance, respectively for the two Fe-Cr brazing filler metals because of the localized corrosion. Nevertheless, the difference of $\beta_c$ (Tafel cathodic slope) with Ni-29Cr-6P-4Si implies that corrosion rate and corrosion resistance are affected by the P content in the Fe-Cr brazing filler metals.

In chapter 3, SUS304 stainless steel was brazed with the Fe-Cr brazing filler metals.

Microstructure, joint strength, fracture mechanism and the effect of the clearance on shear strength were investigated to understand the brazing characteristics of the Fe-Cr brazing filler metals. The results are summarized as follows.

In the clearance of 10 μm, owing to the diffusion of Ni or Ni and Si from the brazed layer to the base material in the joints brazed with Fe-20Cr-43Ni-10P and Fe-20Cr-20Ni-8P-5Si-2Mo, respectively, the diffusion region occurred. At the same time, P and Cr added in the brazing filler metal were concentrated in the whole brazed layer and a P-rich phase was formed in the brazed layer so that the brazed layer has a larger hardness than the adjacent diffusion region. Fracture occurred in the interface of the diffusion region and the brazed layer. In the clearance of more than 50 μm, a primary crystal and the final solidified region emerged in the brazed layer for the joints with Fe-20Cr-43Ni-10P and Fe-20Cr-20Ni-8P-5Si-2Mo. P and Cr added in the brazing filler metal were segregated and enriched in the final solidified region so that a phosphide phase with high hardness generated. The primary phase is a solid-solution phase and the final solidification region consists of a solid-solution phase and the phosphide phase. The phosphide phase arouses much larger hardness of the final solidified region than the primary crystal so that cracks occur. At the same time, the phosphide phase results in uneven distribution of hardness in the final solidified region. The cracks process along the interface of the solid-solution phase and phosphide phase in the finally solidified region. Fracture occurred in the interface of the solid-solution phase and phosphide phase in the final solidified region adjacent to the primary crystal. For every brazing filler metals, the shear strength reaches a maximum value in the clearance of 10 μm. Shear strength is up to 124 MPa, 137 MPa and 174MPa for Fe-20Cr-43Ni-10P, Fe-20Cr-20Ni-8P-5Si-2Mo and Ni-29Cr-6P-4Si, respectively. When the clearance is more than 50 μm, compared with the clearance of 10μm, the shear strength decreases and fluctuates in a tight range of approximately 10 MPa. The joint brazed with Fe-20Cr-43Ni-10P has a strength of approximately 100 MPa although the shear strength is slightly inferior to that of the joint with Ni-based filler metal in every clearance. On the other hand, the joint brazed with Fe-20Cr-20Ni-8P-5Si-2Mo exhibits comparable shear strength with that brazed with Ni-base brazing filler metal when the clearance is less than 200 μm. Along with the increase of the clearance, the change in the chemical compositions of the phosphide phase is negligible. In contrast, the volume ratio of the phosphide phase is changed with the clearance. A tendency is confirmed that shear strength increases with the decrease of the volume fraction of the phosphide phase. The generation of the phosphide phase is the important factor that the shear strength of the joint decreases.

In chapter 4, the corrosion resistance of stainless steel joints brazed with the Fe-Cr brazing filler metals was investigated. To evaluate the corrosion behavior of the joints, immersion tests in artificial compound solutions were performed. The corrosion behaviors of the joints were analyzed and compared by means of morphology of corrosion attack, quantitative analysis and penetration depth. This chapter also aimed to explore the reasons for the change in the corrosion resistance of the brazed joints. The results are summarized as follows.

The microstructures of the fillet areas of the joints brazed with Fe-20Cr-43Ni-10P and Fe-20Cr-20Ni-8P-5Si-2Mo are made up of a primary crystal and the final solidified region. The primary crystals of the joints brazed with Fe-20Cr-43Ni-10P and Fe-20Cr-20Ni-8P-5Si-2Mo appear to be Fe-Cr-Ni-based and Fe-Cr-Ni-Si-based solid-solution phases, respectively. The final solidified region of the joint brazed with Fe-20Cr-43Ni-10P is composed of a Fe-Cr-Ni-based solid-solution phase and Cr-P-Fe-Ni-based phosphide phase. The final solidified region of the joint brazed with Fe-20Cr-20Ni-8P-5Si-2Mo contains a Fe-Cr-Ni-Si-based solid-solution phase and Cr-P-Fe-Ni-Mo-based phosphide phase. Corrosion attacks occurred only in the final solidified regions of the fillet areas in SUS304 stainless steel joints brazed with both Fe-20Cr-43Ni-10P and Fe-20Cr-20Ni-8P-5Si-2Mo. The corrosion resistance of the joints brazed with Fe-20Cr-20Ni-8.0P-5.0Si-2.0Mo is slightly weaker than that of Ni-29Cr-6P-4Si. On the other hand, joints brazed with Fe-20Cr-43Ni-10P does not nearly provide corrosion resistance. Furthermore, the corrosion is accelerated with corrosion time in the joint brazed with Fe-20Cr-43Ni-10P because the phosphide phase, which behaves as the cathode, has been almost retained and leads to the increasing of the area ratio of the cathode to the anode. For the joints brazed with Fe-20Cr-20Ni-8P-5Si-2Mo, along with the corrosion of the fine solid-solution phase, the continuous phosphide phase is exposed on the surface. The continuous phosphide phase hinders corrosion in the deep direction as a corrosion barrier. The fine microstructure results in the high corrosion resistance of the joints.

In chapter 5, the main findings of this study were summarized, and some proposals for further study are offered as well.

## 5.2 Further prospect

To reduce raw material cost, demand in the industry and market has been advancing to develop the Fe-Cr-based brazing filler metals as substitutions for Ni-based brazing filler metals. However, mechanical properties and corrosion resistance of the Fe-Cr brazing filler metals still need to be improved or modified.

As the achievements of this study, it is found that P plays an important role in mechanical properties and corrosion resistance of the joints with the Fe-Cr-based brazing filler metals. It will contribute to improvement to figure out effect of the P content on mechanical properties and corrosion resistance in the Fe-Cr-based brazing filler metals.

In addition, in order to promote the practical use, it is necessary to study on the effect of temperature on the dynamic potential polarization curve and corrosion behavior of passivated Fe-Cr-based brazing filler metals.

Related papers

[1] K.D. Shi, T. Tsunoda, K. Kusumoto, I. Shohji, K. Matsu and Y. Taguchi: Evaluation of Corrosion Resistance of SUS304 Stainless Steel Joint Brazed with Fe-Cr System Alloy, Journal of Smart Processing, **4**-4 (2015) 215-221.
[2] K.D. Shi, T. Tsunoda, K. Kusumoto, I. Shohji, K. Matsu and Y. Taguchi: Joint Strength of SUS304 Stainless Steel Joint Brazed with Fe-Cr System Alloy, Journal of Smart Processing, **4**-5 (2015) 247-253.
[3] K.D. Shi, T. Tsunoda, I. Shohji, K. Matsu and Y. Taguchi: Microstructure and electrochemical corrosion behavior of Fe-Cr system alloys as substitutes for Ni-based brazing filler metal, Acta Metallurgica Sinica (English Letters), **29**-8 (2016) 697-706.

## Acknowledgements

Let me take this opportunity to express my sincere gratitude and pay high tribute to all the people who helped me during the writing of this thesis.

First of all, I would like to extend my sincere gratitude to my supervisor, Prof. Ikuo Shohji, for his constant encouragement and guidance. He has offered me valuable suggestions in the academic studies. In the preparation of the thesis, he has spent much time reading through each draft and provided me with inspiring advices. Without his patient instruction, insightful criticism and expert guidance, the completion of this thesis would not have been possible. I am also deeply indebted to all the other teachers of the Review Committee, Prof. Weimin Lin, Prof. Masaaki Matsubara, Associate Prof. Yoshihiko Hangai and Associate Prof. Shinji Koyama, for their instructive advices and useful suggestions on my thesis.

Secondly, I would like to give my thanks to Takahiro Tsunoda, Kotaro Matsu and Yasuhiro Taguchi. They have provided the statistics of the investigation for my thesis, and walked through all the stages of the writing of this thesis with me.

Finally, I also owe my sincere gratitude to all the fellow classmates in the second laboratory of material system science and engineering. They have helped me work out my problems during the difficult course of the thesis.